

**Polymer and Tissue Separation and Micro/Nano-  
Fabrication via Ultra-Short Pulsed Laser Plasma-  
Mediated Ablation**

**By**

**HUAN HUANG**

A dissertation submitted to the  
Graduate School-New Brunswick  
Rutgers, The State University of New Jersey

in partial fulfillment of the requirements

for the degree of

Doctor of Philosophy

Graduate Program in Mechanical and Aerospace Engineering

written under the direction of

Professor Zhixiong Guo

and approved by

---

---

---

---

New Brunswick, New Jersey

October, 2010

# **ABSTRACT OF THE DISSERTATION**

## **Polymer and Tissue Separation and Micro/Nano-Fabrication via Ultra-Short Pulsed Laser Plasma-Mediated Ablation**

by Huan Huang

Dissertation Director:

Professor Zhixiong Guo

Micro/nano-fabrication of polymers and micro-processing of real human tissues via plasma-mediated ablation were investigated using an ultra-short pulsed (USP) laser of 900 fs pulse duration and 1552 nm center wavelength. For the PDMS polymer micro-fabrication, the ablation threshold for the single spot and the single line scanning ablation features were studied at first. The single pulse ablation threshold is determined to be  $4.62 \text{ J/cm}^2$  and the incubation factor for the multi-pulse ablation is found to be 0.52. The influences of pulse overlap rate and irradiation pulse energy on the ablation line width, internal ablation interface depth, and ablation surface quality were scrutinized. Then the thin layer PDMS separation was completed with thickness controllable via adjusting the laser focus spot position. For the three tests with a target thickness of 20  $\mu\text{m}$ , the

averaged thickness of the separated thin layers is  $20.6 \pm 1.7 \mu\text{m}$ . And a multi-width micro-channel interconnected network was fabricated and the size of the channels varies from 50 to 400  $\mu\text{m}$ . For the real tissue ablation, the fundamental ablation features were investigated. It is found that the threshold of the single pulse ablation for the freeze-dried dermis ( $8.32 \pm 0.37 \text{ J/cm}^2$ ) is slightly smaller than that of the wet dermis ( $9.65 \pm 1.21 \text{ J/cm}^2$ ) due to the light absorption of water in wet tissues. Histological examinations were performed to evaluate the thermal damage and to find appropriate laser parameters for tissue micro-processing with minimal thermal damage. An analytical solution based on the heat conduction equation was derived to analyze the temperature distributions and to obtain the heat affected zones in materials ablated by USP laser line scanning. The analytical results were compared with the experimental measurements and a good agreement was found. Both results show that the thermal damage can be confined in a small zone about 10  $\mu\text{m}$  with proper pulse energy and overlap rate. Pulse energy and pulse overlap rate were the key parameters for the generation and severity of thermal damage. In vitro wet tissue separation into layers by the USP laser ablation was demonstrated with thickness ranging from 200 to 600  $\mu\text{m}$ . The unevenness of the separated layers is under 10%. Freeze-dried tissue stripping was also demonstrated with the stripped thickness in the range of 20 - 40  $\mu\text{m}$ . No sign of visible thermal damage was found for both types of tissues. This study has provided an effective method that can precisely and non-intrusively process polymers and tissues with minimized thermal damage.

## Acknowledgments

I would like to express my pure-hearted appreciation to my advisor, Dr. Zhixiong Guo. With his paramount guidance, I can go through some difficult circumstances and complete this dissertation. During the years of his supervision, I have learned not only how to do research, scientific writing, but also how to be a responsible person with strict independent thinking and analyzing ability. His profound knowledge, logical thinking, keen vision, rigorous attitude towards science, and especially hardworking have impressed me a lot, and will significantly impact my future career path.

My special thanks go to all the committee members, Dr. Prosenjit Bagchi, Dr. Jerry Shan from the Department of Mechanical and Aerospace Engineering, Rutgers University and Dr. Yook-Kong Yong from the Department of Civil & Environmental Engineering, Rutgers University for their time and valuable suggestions for my research and dissertation. Thank you for giving me lots of comments and encouragement to my research.

This project was mainly supported by the Musculoskeletal Transplant Foundation (MTF). I would like to give special thanks to the support of Michael Schuler and Arthur Gertzman at MTF for their help and constructive comments, to Alex Scozzarro at MTF for preparing and providing tissue samples, to Greg Spooner and Carolyn Martinez at Raydiance, Inc., for providing technical support. And I also would like to thank for the other funding supports, including the Charles and Johanna Busch Memorial Fund

managed at Rutgers University and the National Science Foundation (NSF) under Grant No.CBET-0827473.

My appreciation goes to my lab members: Xiaoliang Wang, Jian Jiao and Lei Huang in the group of Thermal Photonics & Engineering Laboratory. Their physical and mental supports helped me a lot in my research and personal life. I would also like to give my great appreciation to my friends: Dr. Po Ting Lin, Dr. Ching Jui Chang and Dr. Bin Zheng for their help to my study and research. Next I would like to thank my friends: Dr. Siwang Yu and Dr. Tin Oo Khor in the Department of Pharmaceutics at Rutgers University and Xin Tong at University of Medicine & Dentistry of New Jersey for the help and advice for my experiments. Thank you my friends. Your help, encouragement and company enriched my life and make the learning and research so easy for me.

Most important, I would like to thank my lovely family: Shizao Huang, my dad; Shilan Peng, my mom; Ying Huang, my sister. I want to show my truly love and thanks to my parents who always believe me and allow me to be as ambitious as I wanted. Their love, kindness, support and encouragement were undeniably the bedrock upon which the past years of my life have been built. This dissertation is also devoted to my grandparents with whom I have had a memorable childhood. I love you all very much.

Finally, I can not show enough gratitude and thanks for the love and support I receive from my wife - Chaoyun Chang. Thank you for your sacrifice, love and encouragement. You have given me a lot of joy and helped me out of pressure and

exhaustion, and you are the reason that driven me going ahead all the time. It is nearly impossible for me to complete this research work without your accompany and support.

## **Dedications**

This dissertation is dedicated to my families and my wife.

# Table of Contents

<b>ABSTRACT OF THE DISSERTATION .....</b>	<b>ii</b>
<b>Acknowledgments.....</b>	<b>iv</b>
<b>Dedications.....</b>	<b>vii</b>
<b>List of Figures .....</b>	<b>xi</b>
<b>List of Tables.....</b>	<b>xiv</b>
<b>Chapter 1. Introduction .....</b>	<b>1</b>
<i>1.1. Literature Review &amp; Motivation.....</i>	<i>1</i>
<i>1.2. Laser Beam Characteristics .....</i>	<i>8</i>
<i>1.3. Mechanism of Laser Ablation.....</i>	<i>12</i>
<i>1.4. Ablation Models.....</i>	<i>18</i>
<i>1.5. Research Contributions .....</i>	<i>26</i>
<i>1.6. Overview of the Dissertation .....</i>	<i>27</i>
<b>Chapter 2. Polymer (PDMS) Thin Layer Separation and 3-D Micro-fabrication by USP Laser Internal Ablation.....</b>	<b>32</b>
<i>2.1. Introduction .....</i>	<i>32</i>
<i>2.2. Materials and Methods.....</i>	<i>35</i>
2.2.1. Experimental Set up.....	35
2.2.2. Sample Preparation .....	37
2.2.3. Measurements .....	37
<i>2.3. Results and Discussion .....</i>	<i>38</i>
2.3.1. Fundamental Study of PDMS Ablation .....	38
2.3.2. PDMS Separation and 3-D Micro-fabrication .....	49
<i>2.4. Fabrication of Micro-channel Network.....</i>	<i>57</i>
<i>2.5. Summary.....</i>	<i>60</i>



<b>Chapter 3. Wet Human Dermis Tissue Separation via USP Laser Plasma-mediated Ablation.....</b>	<b>63</b>
3.1. <i>Introduction</i> .....	63
3.2. <i>Materials and Methods</i> .....	65
3.2.1. Experimental Set up .....	65
3.2.2. Tissue Sample Preparation.....	67
3.2.3. Measurements .....	68
3.3. <i>Results and Discussion</i> .....	69
3.3.1. Fundamental Study of Single Line Surface Ablation.....	69
3.3.2. Thermal Damage Investigation.....	76
3.3.3. Wet Dermis Separation by USP Laser Ablation .....	82
3.4. <i>Summary</i> .....	89
<b>Chapter 4. Freeze-dried Dermis Tissue Cut and Stripping via USP Laser Ablation .....</b>	<b>91</b>
4.1. <i>Introduction</i> .....	91
4.2. <i>Materials and Methods</i> .....	92
4.2.1. Experimental Set up .....	92
4.2.2. Tissue Sample Preparation.....	94
4.2.3. Measurements .....	94
4.3. <i>Results and Discussion</i> .....	95
4.3.1. Single Line Surface Ablation.....	95
4.3.2. Multi-line Surface Ablation .....	100
4.3.3. Thermal Damage Investigation.....	103
4.3.4. Freeze-dried Dermis Cut and Stripping .....	105
4.4. <i>Summary</i> .....	108
<b>Chapter 5. Theoretical Analysis of Thermal Damage.....</b>	<b>110</b>
5.1. <i>Introduction</i> .....	110
5.2. <i>Physical Model</i> .....	117
5.3. <i>Initial and Boundary Conditions</i> .....	119
5.4. <i>Mathematical Formulation</i> .....	121
5.5. <i>Results and Discussion</i> .....	129
5.5.1. Wet Dermis Tissue Sample Ablation.....	129

5.5.2. Comparison with Experimental Results.....	135
5.5.3. Key Laser Parameters .....	136
5.5.3.1. Pulse Energy .....	137
5.5.3.2. Pulse Overlap Rate.....	138
5.6. Summary.....	139
<b>Chapter 6. Near-field Nano-fabrication Based on Monolayer Spherical/Cylindrical Particles .....</b>	<b>141</b>
6.1. Introduction .....	141
6.1.1. Near-field Optics and Intensity Enhancement .....	142
6.1.2. Approaches to Achieve Near-field Intensity Enhancement .....	143
6.1.3. Literature Review .....	144
6.1.4. Objectives .....	145
6.2. Experiment.....	147
6.2.1. Experiment Set up and Design.....	147
6.2.2. Particle Sample & Deposition Method .....	148
6.2.3. Experimental Results and Discussion .....	152
6.3. Simulation.....	160
6.3.1. Introduction.....	160
6.3.2. Mathematical Formulation.....	164
6.3.3. Interface and Boundary Conditions .....	167
6.3.4. Simulation Method .....	169
6.3.5. Simulation Models.....	170
6.3.6. Results and Discussion .....	172
6.3.6.1. Model Verification and Comparison.....	173
6.3.6.2. Influence of Different Parameters.....	175
6.3.6.3. Comparison with Experiment Results.....	180
6.4. Summary.....	180
<b>Chapter 7. Conclusions and Future Work .....</b>	<b>182</b>
7.1. Conclusions .....	182
7.2. Future Work.....	184
<b>References .....</b>	<b>187</b>
<b>Curriculum Vitae .....</b>	<b>197</b>

## List of Figures

Figure 2.1. Sketch of the Experimental Setup.....	36
Figure 2.2. Photos of Sample Fixture and Motion Stage Setup.....	36
Figure 2.3. Microscopic View (400X) of an Ablation Craters Array on PDMS Surface for Single Spot Ablation. ....	39
Figure 2.4. Effects of Pulse Number and Energy on Ablation Crater Diameter.....	40
Figure 2.5. (a) Square Diameter of the Single Pulse Ablation Crater versus the Incident Pulse Energy for Effective Focal Radius; (b) Square Diameter of the Single Pulse Ablation Crater versus the Irradiation Pulse Fluence for Ablation Threshold.....	41
Figure 2.6. Multi-pulse Incubation Effect on PDMS Single Spot Ablation. ....	43
Figure 2.7. Microscopic View (1000X) of Ablated Single Lines at PDMS Surface with Different Pulse Overlap Rates and Various Irradiation Pulse Energies. ....	45
Figure 2.8. Plots of the Single Ablation Line Width versus the Irradiation Pulse Energy. ....	46
Figure 2.9. Incubation Effect on PDMS Single Line Ablation with Different Pulse Overlap Rate. ....	47
Figure 2.10. Ablation Line Widths versus Pulse Energy for Effective Spot Radius. ....	48
Figure 2.11. Photos of the Separation Area Scanned PDMS Blocks.....	51
Figure 2.12. (a) Microscopic View (400X) of the Ablation Interface Across the Cross-section of a Separation Scanned PDMS Block (1 mm deep, 1 pulse/ $\mu\text{m}$ , and 1.0 $\mu\text{J}$ ); (b) Microscopic View (40X) of Ablation Cuts at Different Depth Inside a PDMS Sample (1 pulse/ $\mu\text{m}$ and 1.0 $\mu\text{J}$ ); and (c) A Plot of the Measured Ablation Interface Depth Versus the Laser Beam Focusing Depth Inside PDMS (1 pulse/ $\mu\text{m}$ and 1.0 $\mu\text{J}$ ).....	54
Figure 2.13. Ablation Line Widths versus Pulse Energy for Effective Spot Radius. ....	55
Figure 2.14. Demonstration of PDMS Thin Layer Separation (2 pulses/ $\mu\text{m}$ and 1.0 $\mu\text{J}$ ).....	55
Figure 2.15. Surface Profilometer Measurement of Thin Layer PDMS Separation Thickness.....	56
Figure 2.16. Microscopy View of a PDMS Separation Surface (5 pulses/ $\mu\text{m}$ and 1.0 $\mu\text{J}$ ).....	58
Figure 2.17. Multi-width Micro-channel Network Fabricated via the USP Laser Direct Writing (2 pulses/ $\mu\text{m}$ and 1.0 $\mu\text{J}$ ). ....	59
Figure 2.18. SEM Images of the Multi-width Micro-channel Network Structure.....	60
Figure 2.19. Micro Structures Fabricated by USP Laser Internal Ablation.....	61
Figure 3.1. Sketch of the Experimental Setup.....	67
Figure 3.2. Photo of One Wet Dermis Sample before Experiment. ....	68
Figure 3.3. Microscope View of Wet Dermis Single Line Surface Ablation with Different Laser Paramters. ....	70
Figure 3.4. SEM Images of the Single Line Ablations with a Fixed Pulse Overlap Rate 20 pulses/ $\mu\text{m}$ and Different Irradiation Energies. ....	72
Figure 3.5. Square of Ablation Line Width versus Irradiation Pulse Energy for the Evaluation of	

Effective Focal Spot Size.....	74
Figure 3.6. Incubation Effect on Wet Dermis Single Line Ablation with Different Pulse Overlap Rate. ....	75
Figure 3.7. Single Line Ablation Depths as a Function of Irradiation Pulse Energy.....	75
Figure 3.8. Histological Views of Single Line Ablation at Wet Tissue. ....	78
Figure 3.9. Histological Views of Multi-line Ablation at Wet Tissue.....	79
Figure 3.10. Alternative Set up of Wet Dermis Separation. ....	83
Figure 3.11. Ablation Spark from Wet Dermis Separation with 100 $\mu\text{m}$ Deep into Dermis and 250 kHz Repetition Rate. ....	85
Figure 3.12. Microscope View of Separated Wet Dermis Layer on Sapphire Window after 2 times Repeat with 20 $\mu\text{m}$ Increase (40X). ....	86
Figure 3.13. Microscope View of Wet Dermis Residue on Sapphire Window (20 pulses/ $\mu\text{m}$ & 2.5 $\mu\text{J}$ , 40X).....	86
Figure 3.14. Wet Tissue Separation by the USP Laser Ablation.....	87
Figure 3.15. An Image of a Partially Separated Dermis.....	87
Figure 4.1. Experimental Setups for the USP Laser Freeze-dried Tissue Layer Stripping. ....	93
Figure 4.2. Microscopy View of Single Line Ablation at the Freeze-dried Dermis Surface with Different Laser Parameters.....	96
Figure 4.3. SEM Images of Single Line Ablation at the Freeze-dried Dermis Surface with Different Irradiation Energies.....	98
Figure 4.4. (a) Square of Ablation Line Width versus Pulse Irradiation Energy, and (b) Single Line Ablation Depth versus Pulse Irradiation Energy.....	99
Figure 4.5. Incubation Effect on Freeze-dried Dermis Single Line Ablation with Different Pulse Overlap Rate. ....	100
Figure 4.6. Microscopy View of Multi-line Ablation at the Freeze-dried Dermis Surface with Different Repeat Lines (20 pulses/ $\mu\text{m}$ , 2.5 $\mu\text{J}$ ). ....	101
Figure 4.7. SEM Images of Multi-line Surface Ablation at Freeze-dried Dermis with Pulse Irradiation Energy 2.5 $\mu\text{J}$ and Overlap Rate 20 pulses/ $\mu\text{m}$ . ....	102
Figure 4.8. Ablation Depths and Widths Subject to Repeated Line Ablation with 2.5 $\mu\text{J}$ and 20 pulses/ $\mu\text{m}$ . ....	103
Figure 4.9. Histological Views of the USP Laser Ablation in the Freeze-dried Dermis with Pulse Irradiation Energy 1.0 $\mu\text{J}$ and Overlap Rate 20 pulses/ $\mu\text{m}$ . ....	104
Figure 4.10. Freeze-dried Dermis Cut by Repeated Line Scanning Ablation (Solid Arrow: Cut Through Area; Hollow arrow: Partially Cut Through Area). ....	106
Figure 4.11. Back Side Freeze-dried Dermis Cut by Repeated Line Scanning Ablation. ....	107
Figure 4.12. Thin-layer Stripping from a Freeze-dried Dermis.....	107
Figure 5.1. Threshold temperatures for thermal damage as a function of exposure time [119]. ....	116
Figure 5.2. 2-D Cylindrical Coordinates Domain Sketch for Multi Pulse Ablation.....	119

Figure 5.3. 1-D Cylindrical Coordinates Domain for Thermal Damage Analysis. ....	120
Figure 5.4. Temperature Increase with Time for Different Location( $4\mu m \leq r \leq 13\mu m$ ): .....	132
Figure 5.5. Temperature Increase along Different Location for Different Pulse Overlap Rates. (2.5 $\mu$ J Pulse Energy).....	134
Figure 5.6. Thermal Damage Zone Size Compared with Experimental Investigations for Different Pulse Overlap Rates.....	136
Figure 6.1. Ti:Sapphire Femtosecond Laser System. ....	148
Figure 6.2. (a) Set Up of Monolayer Spherical Nano Particle Deposition; (b) Microscope View of Monolayer Silica Spherical Particle on Silicon Substrate (0.05% DI Water Suspension, 200x); (c) SEM Image of Monolayer Deposited Spherical Particles on Substrate. ....	151
Figure 6.3. (a) PDMS Substrate with Nano Holes after Irradiation; (b) Silicon Substrate with Nano Holes after Irradiation and Particle Removal.....	154
Figure 6.4. (a) CNT on Silicon Substrate; (b) Nano Line Feature on Silicon Substrate.....	155
Figure 6.5. (a) Silica Nano Rod on Silicon Substrate (260 nm diameter); (b) Another Silica Nano Rod on Silicon Substrate (500 nm diameter).....	157
Figure 6.6. (a) 2D model Domain for COMSOL Simulation Calculation; (c) A Typical Solution of Electric Field Distribution for the Whole Domain (Rod Diameter: 300nm, Wavelength: 600 nm).....	172
Figure 6.7. y component of the electric field of the scattered wave in the near field as a function of x for different z (S-incident) [151] .....	175
Figure 6.8. Z component of the electric field of the scattered wave in the near field as a function of x for y=0.25 by COMSOL (gold on gold substrate).....	176
Figure 6.9. Enhancement Factor for the Center Point Right on Surface of Substrate with 100 nm Rod Diameter (Gap Distance Changes from 0 to 100 nm).....	176
Figure 6.10. Solution of Silica Cylinder on PDMS Substrate with Different Gaps (Gaussian Beam with 2 v/m Maximum Electric Field for Incident Wave, D=500 nm).....	177
Figure 6.11. Maximum Enhancement Factors in the Gap with Different Gap Distance (100-500 nm Rod Diameters).....	179
Figure 6.12. Maximum Enhancement Factors in the Gap with Different Rod Diameters (0-400 nm Gap Distance).....	179

## List of Tables

Table 1.1. Ablation Threshold for Different Materials and Lasers Parameters.....	29
Table 2.1. Specific Focal Spot Radius and Ablation Thresholds for Different Pulse Overlap Rates .....	48
Table 2.2. Test of Laser Parameters for PDMS Separation Focusing 1 mm Inside PDMS.....	50
Table 2.3. Thickness of the Separated Thin PDMS Layers (Dimension: 10mm × 2mm). ....	58
Table 3.1. Effective Focal Spot Radii and Ablation Thresholds for Different Pulse Overlap Rates. ....	74
Table 3.2. Lateral Thermal Damage Zones Results from 100-line Ablation.....	80
Table 3.3. Results from Several Dermis Separation Tests. ....	88
Table 4.1. Effective Focal Spot Radius and Ablation Threshold for Different Pulse Overlap Rates. ....	98
Table 4.2. Results from Several Freeze-dried Dermis Stripping Tests.....	108
Table 5.1. Thermal Properties for Dermis Tissue [35]. ....	129
Table 5.2. Thermal Damage Zone for Different Pulse Overlap Rate. (2.5 μJ Pulse Energy).....	134
Table 5.3. Thermal Damage Zone for Different Pulse Overlap Rate with Effective Thermal Properties. (2.5 μJ Pulse Energy).....	134

## Chapter 1.

### Introduction

#### ***1.1. Literature Review & Motivation***

Although conventional machining has undergone miniaturization efforts, modern micromachining technologies like sawing, cutting, drilling, or grinding are only capable of producing structures in the range of a few 10  $\mu\text{m}$  and have their limitations in the course of the progressing miniaturization. For instance, when separating natural tissues into thin layers and for precisely cutting and shaping tissues, techniques using a surgical knife to separate a tissue into multiple layers or cut the tissue into portions are often limited in precision, resulting in a large amount of waste [1]. For the removal of a few defined cubic micrometers of silicon from the surface of a delicate sensor, there are no mechanical tools available that might be able to handle with this precision.

Micro-fabrication technologies originated from the microelectronics industry and are used to produce devices with dimensions of micrometer sizes and smaller. Micro-fabrication processes can be effectively applied to yield a single device or thousands of devices, the so-called batch processing. This does not only lead to a tremendous cost reduction, but also enables the production of array structure or large device series with minute fabrication tolerances. Micro-fabrication processes hence significantly differ from conventional machining processes. However, for microelectronics-originated micro-fabrication, many processes are needed, one after the other, many time repeatedly. These

processes typically include deposition of thin film, patterning or etching with desired micro features, and removing the rest of the film. These processes make micro-fabrication very complex and expensive.

Micro-fabricated devices include integrated circuits, micro-electro-mechanical systems (MEMS), laser diodes, flat panel displays and micro-sensors. Micro-fabricated devices are not generally freestanding devices but are usually formed over or in a thicker support substrate. For electronic applications, semi-conducting substrates such as silicon wafers can be used; for optical devices or flat panel displays, transparent substrates such as glass or quartz are common; for life science applications, polymer substrates can be used. Polymers micro-fabrication has become a quickly growing field of micro-fluidic systems for tissue engineering and life sciences because they show a high compatibility to many biologically active molecules and living cells. Current polymer micro-fabrication techniques include replica molding [2], stereolithography [3], and electro-spinning [4], etc. Replica molding is low-cost, but requires multiple processing steps and has issues like chemical biotoxicity to the polymers [2]; Stereolithography can fabricate high aspect ratios and a wide variety of functional materials, but it builds up the structure slowly and allows only limited device volumes [3]; Electro-spinning techniques can produce continuous nano-fibers from various polymers, but require high voltage and a collecting substrate [4].

Recently, considerable efforts have been devoted to utilizing laser micro/nano-fabrication techniques [5, 6] because lasers can create complex micro structures



resembling a natural tissue environment and have many advantages such as clean, non-invasive, and precise processing. In addition, only an optical lens is needed to focus a laser beam to the micro level for realization of micro-fabrication in laser direct writing techniques [7]. Laser processing of materials has become a field of growing importance with applications in mechanical engineering, such as drilling, cutting, bending, welding, cleaning, hardening, alloying and surface treatment; in electrical engineering and materials science, such as photolithography, ablation, thin film deposition, doping, annealing, recrystallization, defect scanning and mapping; in chemical engineering such as laser induced reaction, dissociation, photo-ionization; and in bioengineering, such as tissue cleaning and tissue removal. At low laser flux, the material is heated by the absorbed laser energy and evaporates or sublimates. At high laser flux, the material is typically converted to plasmas. One describes the effect as a strong local ionization of the medium, where the plasma reaches density beyond a critical value. Laser ablation that takes great advantages in precise material removal is a promising method in processing and treatment of metal [8-10], biological tissues [11-14], polymers [15-17], collagen gels [18], dental implants [19], glasses [20], etc.

Meanwhile, surgical treatment is frequently restricted by the scarcity of adequate donor tissues available for reconstruction in medical implantation field. Separation of a donor soft tissue such as human skin into two or multiple layers leads to augmented usages of the limited tissues, doubling or even tripling the harvest of donor tissues. Moreover, a tissue may have to be separated into layers, as the tissue in its entirety may not be necessary or appropriate for implantation. The use of these natural biomaterials

typically requires chemical or physical pretreatment for sterilization and immunogenicity reduction and other processing, such as preparing the tissue by cutting and shaping the tissue into an appropriate form before being transplanted into a patient or subject [1, 21-24]. However, there lack effective and efficient methods for separating natural tissues into thin layers and for precisely cutting and shaping tissues without collateral damage [1], saying by experts in the Musculoskeletal Transplant Foundation (MTF), the largest tissue bank in USA. Techniques using a mechanical tool or surgical knife to separate or cut the tissue are often limited in precision. It is noticed that those mechanical tools can cause damage to the underlying layers and surrounding tissues to the range of 0.1 to 1 mm. For chemical method, it is time-consuming and the residues at the tissue sample could be hard to remove and is harmful for the safety of further usage. Thus, it would be very useful to develop an effective method that can precisely and non-intrusively modify tissues without collateral damage.

Since the invention in the 1960, laser has been of great interests in medical diagnosis, treatment and therapy. It was greatly anticipated that laser would enable manipulation and destruction of biological tissue with unprecedented precision and selectivity. Considerable efforts have been devoted into the medical applications of lasers and it has become one of the most important and rapidly growing areas of modern laser physics, such as laser eye surgery and tumor removal. However, a clinically viable application of laser ablation was delayed mainly due to a lack of understanding of the fundamental mechanisms of laser-tissue interactions. In practice unacceptable local tissue damage and slow material removal rates have inhibited the real clinic applications of

lasers in many areas. Fundamental investigations with different types of tissue have been conducted with different types of lasers. Typically, treatment by a conventional pulsed laser (nanoseconds to microseconds pulse width) leads to cracking, melting, charring of the surrounding materials [25]. Sasaki *et al.* [26] conducted bone tissue ablation with a 200 ms Er:YAG laser and a continuous-wave CO<sub>2</sub> laser and revealed that the thermal damage layer of the CO<sub>2</sub> laser was much severe than the ablation by the Er:YAG laser; Walsh *et al.* [27] studied tissue removal by an infrared laser pulsed CO<sub>2</sub> laser and the zone of thermal damage increased from 50  $\mu\text{m}$  to 750  $\mu\text{m}$  when the pulse duration increases from 2  $\mu\text{s}$  to 50 ms. Trauner *et al.* [28] used a near-infrared pulsed holmium laser (400  $\mu\text{s}$  pulse duration and 2.1  $\mu\text{m}$  wavelength) to ablate bovine tissue with 550  $\mu\text{m}$  thermal damage zone from ablation sites.

More than a decade ago, intensive research in short pulsed laser micromachining of inorganic and biological samples has been initiated and this opens a wide range of industrial and medical laser applications since they can provide higher precision and less thermal damage than long-pulsed laser or continuous wave (CW) laser [11-14]. The ultra-short pulsed (USP) laser, which refers to lasers with a few picoseconds or down to femtoseconds pulse duration, has opened a new era especially for micro-fabrication of polymer and micro-processing of tissues.

Neev *et al.* [29] conducted preliminary studies of 350 fs and 1053 nm pulse interactions with hard tissue (dentin, nail, and enamel) and compared their results to the nanosecond ablation regime; Rode *et al.* [30] studied the laser ablation of dental enamel

using 95 and 150 fs pulses without collateral damage and the materials removal rates of dental enamel were compared with other techniques; Kim *et al.* [31] investigated the influence of pulse duration on ultrashort laser ablation of dental hard tissue and water and found that there was a transition occurs between 1 and 5 ps for both materials; Sun *et al.* [32] experimentally confirmed the corneal ablation threshold as a square-root dependence function of the laser pulse width 800 fs to 20 ps pulse duration range; Fischer *et al.* [12] performed brain tissue ablation using 35 ps and 1053 nm laser pulses and no thermal damage was induced, while microsecond pulse induced 20  $\mu\text{m}$  lateral damage zone due to the longer pulse durations and the higher pulse energies; Göetz *et al.* [33] conducted *in vitro* ablation experiments with a 20 ps Nd:YLF laser at 1053 nm to investigate the effects of liquid media (distilled water and physiological saline) on the ablation efficiency and quality; Loesel *et al.* [14] conducted non-thermal *in vitro* ablation of bovine neural tissue with 100 fs to 35 ps pulse duration laser with wavelengths ranging from 630 to 1053 nm and no sign of significant thermal damage was observed by histopathological examinations; More experimental studies with different types of materials and laser parameters are listed in Table 1.1, with ablation threshold and incubation factor indicated for comparison.

For USP laser ablation, its precision, high peak power, flexibility, non-thermal interaction, and non-clean room operation provide many advantages in micro-fabrication for many applications. USP lasers have been widely used for micromachining because collateral damage is mostly eliminated in materials and heat affected zones in target materials can be smaller. The main characteristic of ultra-short laser pulses is the very

high peak intensity and the rapid deposition of energy into the material. At this high intensity, the onset of optical breakdown that initiates ablation can be more deterministic and a wide range of materials can be machined.

However, the understanding of USP laser-material interaction mechanism has not been fully established and especially for laser tissue interaction in order to produce the desired processing results. The thermal damage check of ablation to the surrounding area is also desired for applications in laser tissue micro-processing. The purposes and motivations of this dissertation work are to experimentally investigate the USP laser application of polymer micro/nano-fabrication and real tissue micro-processing, such as separation and cut. The ablation on a variety of sample materials are to be carried out, including polymer and biological tissue materials. The significant applications of USP laser in polymer micro/nano-fabrication and tissue micro-processing are to be demonstrated. This study is to try to answer these questions: (1) what are the ablation thresholds and incubation factors for polymer (PDMS) and human dermis tissue? (2) What are the proper laser parameters for PDMS separation and what is the minimum thickness for the separated layer? (3) How USP laser can be applied to real tissue micro-processing with high precision and minimized thermal damage, such as separation and cut? (4) How much is the thermal damage for the USP laser micro-processing of tissues and what is the analytical formulation between the laser parameters and the thermal damage zone? What are the key parameters and relationship to induce the thermal damage? (5) What is near-field enhancement and what are the key factors for the USP laser nano-fabrication by near-field effect, especially for nano-line fabrication.

A review of studies of USP laser-material interaction for various materials above the laser damage threshold has already been presented as shown in Table 1.1. This chapter will also give a brief review of the literature of the laser-material interaction process especially for laser-tissue interaction and a review of the laser ablation models. Finally, research objectives and the outline of this dissertation are discussed.

## ***1.2. Laser Beam Characteristics***

In most laser related applications, laser beam propagation should be considered. Focusing by objective lens is sometimes necessary to shape the laser beam. In general, laser beam can be assumed to have an ideal Gaussian intensity profile, which corresponds to the theoretical TEM<sub>00</sub> mode. Unfortunately, the output from real-life lasers is not truly Gaussian. To accommodate this variance, a quality factor -  $M^2$  factor, has been defined to describe the deviation of the laser beam from a theoretical Gaussian. A low  $M^2$  value indicates good beam quality and ability to be focused to a tight spot. In this study, the  $M^2$  of the USP laser beam used is very small ( $<1.3$ ), and thus the beam can be approximated as a Gaussian profile.

To specify and discuss the beam propagation characteristics, the diameter of the laser beam should be defined at first. The beam width is the single most important characteristic of a laser beam profile. The  $1/e^2$  definition is in common use for beam width. The  $1/e^2$  width is equal to the distance between the two points on the marginal distribution that are  $1/e^2 = 0.135$  times the maximum value. The laser beam diameter can be measured by the knife-edge measurement technique as follows: slice a laser beam with

a razor and measure the power of the clipped beam as a function of the razor position. The measured curve is the integral of the marginal distribution, and starts at the total beam power and decreases monotonically to zero power. The width of the beam is defined as the distance between the intensity points at 13.5% ( $1/e^2$ ) of the peak which were calculated to be 2.3% and 97.7% for the integrated power levels at the intensity points.

As a light source, a laser beam offers several unique features for material processing. Monochromaticity is one of the unique characteristic of laser light and laser light is many times more monochromatic than the light from any other source. Since the absorption coefficient of different materials is highly wavelength dependent, by selecting the laser beam wavelength from deep ultra-violet to infrared, one can precisely control the material processing. Laser light is generated coherent and all the light waves travel in the same direction at the same frequency and in phase. This allows one to focus the laser beam very tightly down to micron level and this provides the means for precise laser processing. Another important characteristic of the laser beam is its very small divergence. The beam divergence determines the spot size. Higher the divergence, higher is the spot size and vice versa.

The ability to optimize the lens design with computers and machine the optic products to better specifications is somewhat helpful in focusing the laser beam to smaller spot sizes. However, even with acceptably overcoming spherical and chromatic aberrations in lens systems, the diffraction limit still restricts higher resolutions. The

diffraction limit, no matter how good the optical system is will still limit the ability to resolve small objects. This limit arises from the wave nature of light. Light waves interfere and this causes diffraction of light. The diffraction-limit focal spot size can be obtained by:

$$d_{\min} = 2.44 \times \lambda \times \frac{f}{\phi} = 1.22 \times \frac{\lambda}{N.A.}, \quad (1.1)$$

where  $\lambda$  is the wavelength of the laser;  $f$  is the focus length of the lens in free space;  $\phi$  is the diameter of the incident laser beam,  $N.A.$  is the numerical aperture of the lens. Thus, when viewed through an aperture or a lens with a finite collection angle, the resolvable feature separation is limited by the wavelength of light and the solid angle of light collected. Although the introduction of light sources with shorter-wavelength techniques is helpful to maintain the current rate of device miniaturization, a point will be reached at which the traditional approaches of shortening the exposure wavelength will no longer be able to produce the required feature sizes. The other approach to improve the diffraction limited resolution of focused light is to increase the index of refraction at the focus. With an oil immersion lens [34], the space between the lens and sample can be filled with oil, and this shrinks the focused spot size. However, this technique is limited by the refractive index of the oil.

In general, if the focused laser energy flux is in excess of  $10^{11}$  W/cm<sup>2</sup>, it will result in an optical breakdown in solids and the excitation of plasma-induced ablation. Thus ablation can be easily achieved for a  $\mu$ J level ultra-short pulse with a focal spot size less than 10  $\mu$ m. The energy flux in the beam focus can be calculated by



$$q'' = \frac{E \times (1 - R)}{t_p \times (\pi \times r^2)}, \quad (1.2)$$

where  $q''$  is the energy flux for the laser pulse,  $E$  is the pulse energy,  $t_p$  is the pulse duration,  $r$  is the radius of the focused laser beam spot and  $R$  is the percentage of the total beam energy loss in the optical system. For example, in the PDMS separation experiment, the laser beam is focused about 1 mm inside the PDMS. The pulse energy ( $E$ ) is preset as 5  $\mu$ J and the pulse duration ( $t_p$ ) is 0.9 ps. The PDMS is semi-transparent, and the optical transmission can be calculated by Beer-Lambert's law as shown in Eq. (1.3)

$$I = I_0 e^{-\mu l}, \quad (1.3)$$

where  $I_0$  and  $I$  are the intensity of the incident light and the transmitted light, respectively;  $\mu$  is the attenuation coefficient and  $l$  is the path length in the material. The attenuation is about 15% for a piece of PDMS with 1 mm thickness. The total losses of beam energy include the energy loss in the optical system (50%) and the energy loss inside the PDMS (15%), so totally  $R = 1 - 50\% \times 85\% = 57.5\%$  when focusing 1 mm inside the PDMS. Considering the calculated focal spot diameter (7.6  $\mu$ m) in free space, the refractive index of PDMS is 1.45 and the focal spot size 1 mm inside the PDMS after refraction will be about 3% larger than that in free space because of the refractive index discontinuity. So considering all the energy losses and the focal spot diameter change, the energy flux in the focus area 1 mm inside the PDMS can be calculated by Eq. (1.2) and it is about  $5.2 \times 10^{12}$  W/cm<sup>2</sup>, which is enough for optical breakdown of PDMS materials and

excitation of ablation.

### ***1.3. Mechanism of Laser Ablation***

The variety of interaction mechanisms that may occur when applying laser to materials is manifold. There are specific material characteristics as well as laser parameters that can contribute to the diversity. For material characteristics, the refractive index, surface roughness, absorption and scattering are the most important properties. For laser parameters, pulse duration, wavelength, focal spot size, pulse energy and exposure time are the most important features, and especially pulse duration is a very crucial parameter to determine the type of interaction and mechanism.

The spatial distribution of volumetric energy density generated by laser irradiation is controlled by the incident energy flux and the optical absorption and scattering properties of the materials. Both optical absorption and scattering play important roles in determining the spatial distribution of volumetric energy density deposited in the target. When absorption is dominant over scattering, the optical penetration depth of the incident radiation is given by the reciprocal of the absorption coefficient, and the Beer-Lambert law as shown in Eq. (1.3) can be applied accurately to describing the spatial distribution of absorbed laser energy in the target. When scattering is dominant comparable to absorption, one must resort to more detailed models of radiative transport to obtain the distribution of the absorbed radiation [35].

In this study, three different materials have been used for the laser ablation -

polymer, wet human dermis tissue and freeze-dried human dermis tissue. For the polymer material (PDMS), it is optical transparent against the laser light (1552 nm wavelength) and its absorption and scattering of the USP laser wavelength range is small when the laser beam is focused inside the polymer; for the wet dermis tissue, water is the most important chromophore in the infrared and it contributes significantly to tissue absorption when the wavelength is above 900 nm. There are absorption peaks located at 0.96, 1.44, 1.95, 2.94, 4.68, and 6.1  $\mu\text{m}$  wavelengths for water [36]. The optical absorption of water in the near-infrared is initially weak but rises quite rapidly with wavelength. From the visible spectral region, the absorption of water increases by nearly 6 orders of magnitude and reaches a maximum at 2.94  $\mu\text{m}$  wavelength, where the absorption coefficient is  $12,000\text{ cm}^{-1}$  [37]. Meanwhile, optical scattering for collagen-based dermis is also very strong because it possesses collagen fibrils with a significant variability in diameter, orientation, and spacing. This variability produces significant refractive index variation over spatial scales. From experimentally measured results by Troy *et al.* [38], the optical scattering of human skin is in the same order of optical absorption for 1552 nm wavelength. So both scattering and absorption are important for the attenuation of laser light in the study of wet tissue ablation; for freeze-dried dermis tissue, since it is dry, water absorption is not a concern and optical scattering is the major concern for the laser energy transfer. The measurement of tissue optical properties is typically done under room conditions. However, the thermal and mechanical transients generated in the ablation processes are substantial and can result in significant alteration of the tissue optical properties, which are not discussed in this study.

For laser tissue interaction, there are mainly five categories of interaction types: photochemical interaction, thermal interaction, photoablation, plasma-mediated ablation, and photodisruption. However, most interactions do not fall clearly into one of these categories, and often multiple processes are competing with each other [39].

Photochemical interaction stems from empirical observations that light can induce chemical effects and reactions within macromolecules or tissues. Photochemical interaction takes place at very low power densities (typically  $1 \text{ W/cm}^2$ ) and long exposure time (1 second to CW). In the field of medical laser physics, photochemical interaction mechanisms play a significant role during photodynamic therapy (PDT) and the main idea is to use a chromophore receptor acting as a catalyst. Therefore, this type of interaction is also called photosensitized oxidation. [39]

Thermal interactions usually happen for pulse duration of  $\mu\text{s}$  or higher and they include a large group of interaction types and different effects like coagulation, vaporization, carbonization and melting, which can be distinguished from the duration and peak value of the tissue temperature achieved. Compared with photochemical interactions, thermal interactions do not need to be governed by a specific reaction pathway. Coagulation occurs when the temperature reaches at least  $60^\circ\text{C}$  and can be illustrated by histological check and the coagulated area appears obviously darker than normal tissue. Vaporization is often attributed by the water absorption and it is sometimes referred to thermo-mechanical effect due to the pressure build-up involved. Carbonization happens at temperature above about  $150^\circ\text{C}$  and will lead to a blackening in

color. Melting usually occurs in hard tissue when the temperature reaches a few hundred degrees Celsius [39].

Temperature is the governing parameter for all thermal interactions. And the temperature rises and thermal diffusion generates significant thermal and mechanical transients. In biological tissues, absorption is mainly due to the presence of water molecules or macromolecules such as proteins and pigments. The heat generation is determined by the linear absorption, and laser parameters and optical tissue properties should be considered, such as exposure time, absorption coefficient and irradiance. Heat transport is characterized by heat conduction, heat convection and heat irradiation. One typical example of heat convection in tissue is heat transfer due to blood flow. Due to the low perfusivity of most tissues, heat convection is negligible. Heat radiation is described by Stefan-Boltzmann's law which states that the radiated power is related to the fourth power of temperature. Due to the moderate temperature achieved in most laser-tissue interactions, heat radiation can often be neglected. The final heat effects depend on the tissue type and the temperature distribution [40, 41]. Rapid heating of tissue by pulsed laser radiation leads to the generation and propagation of thermo elastic stresses as the heated tissue volume reconfigures to its new equilibrium state. The competition of the rate of the energy deposition with characteristic times needed for thermodynamic and mechanical response to the fast laser heating determines the character and the relative importance of photothermal and photomechanical processes in the ablation. Phase transitions processes, such as normal vaporization, normal boiling, and phase explosions drive the formation of an ablation plume that consists of material removed from the

ablation site [42-44].

Photoablation is kind of UV light-induced ablation for nanosecond lasers and the material is decomposed when exposed to high intense laser irradiation ( $10^7$ - $10^8$  W/cm<sup>2</sup>). If a UV photon is absorbed, the energy gain is usually high enough to access an electronic state which exceeds the bond energy and atoms are promoted to repulsive excited state, then the dissociation of chemical bonds happen and fragments are ejected. Because of the relatively higher photo energy for UV lights, photoablation interaction is limited to UV lasers - typically excimer lasers which can provide an energy level sufficient for dissociating the bonds. Moreover, it was observed that certain threshold intensity must be applied to achieve photoablation. Above this threshold intensity, a well defined depth is ablated, depending on the absorption coefficient and the incident intensity. At the same time, an audible report is heard and visible fluorescence is observed at the impact site. Photoablation can be differentiated from thermal interaction by the photon energy or laser wavelength [45, 46]. Photoablation can induce very clean ablation without appearance of thermal damage.

The mechanism of USP laser ablation is totally different from the ablation mechanism of the longer pulsed lasers (order of ns or higher) and CW lasers. Typical interactions, such as thermal interactions and photoablation, rely on linear photon absorption, while USP laser ablation is governed by laser induced plasma-mediated ablation, also known as laser induced ablation, when the intensities of the pulses are high enough ( $10^{11}$  W/cm<sup>2</sup> for solids and fluids) [39]. For linear absorption by longer pulsed

laser, the energy of a single photon is usually smaller than the band gap needed to ionize an electron. For USP laser, the extremely high intensity of powerful pulses leads to a saturated photon flux, causing multi-photon ionization and tunneling photo ionization in the materials. Multi-photon ionization can be realized when an electron absorbs two or more photons simultaneously to gain enough energy to cross the band gap at very high laser intensity and is thereby excited to the conduction band. On the other hand, in an intense electric field, the potential barrier of an atom (molecule) is distorted drastically. Therefore, the length of the barrier that electrons have to pass decreases and electrons can escape from the atom (molecule) easily. Tunnel ionization is a process in which electrons in an atom (or a molecule) pass through the potential barrier and escape from the atom (or molecule) [42, 47, 48].

These effects result in the ionization of some atoms and molecules, thereby providing initial free electrons for the laser induced optical breakdown. Once one starting free electron has been generated, it can absorb photons and accelerates via “inverse Bremsstrahlung absorption” (IBA) in the course of collisions with other charged particles. The absorption of the photon increases the kinetic energy of the free electron. After several events, the kinetic energy of the electron exceeds the band gap energy and the accelerated electron strikes another atom and ionizes it by impact ionization, resulting in two free electrons each with less individual energy. These two free electrons, in turn, absorb more photons, accelerate, strike other atoms, and release two more electrons, and the recurring sequences of avalanche ionization lead to a rapid growth in the number of free electrons [49, 50]. For plasma to grow, the irradiance must be intense enough to

cause rapid ionization, such that losses do not quench the electron avalanche. Recombination and free-electron diffusion from the focal volume are the main loss mechanisms during avalanche ionization. When the density of the free electron reaches to a critical value ( $10^{21}$  or  $10^{22}$  cm<sup>-3</sup> for USP laser), optical breakdown happens.

At the breakdown threshold, plasma formation is restricted to the focal region of the laser beam. Due to the expansion of the plasma, ablation fragments are ejected out of the interaction zone and ablation is achieved. When the pulse energy exceeds significantly the breakdown threshold, the originally formed plasma is characterized by a growth of the plasma from the beam waist toward the incoming laser beam by absorbing and scattering incident light.

#### ***1.4. Ablation Models***

Meanwhile, to provide rough predictions for the amount of material removal based on knowledge of the laser parameters, ablation models have been developed to determine the ablation threshold and ablation efficiency for comparison with experimental studies. Especially for laser tissue interaction, considering the complexity of the phenomena involved (phase transition, plume dynamics, bond - breaking, etc.) and the variety of laser and tissue parameters, it is quite difficult to devise a single model that represents the physics of the processes involved and yields predictions for quantities such as the amount of material ablated, the ablation threshold, and the zone of the residual thermal damage within the tissue bulk.



Two early ablation models that were heuristic in nature were first developed - blow-off model and steady-state model. These two models were not designed with any particular ablation mechanism and the goal of them was to provide rough predictions for the amount of material removal based on knowledge of the laser parameters. The blow-off model was first developed to predict the etch depth resulting from pulsed UV laser ablation of polymers [45, 51] and has also been applied to tissue ablation data. In this model it is assumed that the total pulse energy is absorbed by the irradiated material and no material is removed during the laser pulse. Finite threshold fluence  $F_{th}$  is required to initiate ablation and fluences below the threshold result only in heating of the target. These conditions are nearly always satisfied when performing laser ablation using pulse durations on the time scale of 100 ns or less. For an incident laser fluence,  $F_0$ , larger than the threshold radiant exposure,  $F_{th}$ , material will be removed up to an etch depth  $\delta$ . This results in the following relationship between the etch depth,  $\delta$ , and the incident radiant exposure:

$$\delta = \frac{1}{\mu_a} \ln\left(\frac{F_0}{F_{th}}\right) \quad (1.4)$$

Similar to the blow-off model the steady-state model requires the delivery of a threshold radiant exposure to the target to initiate material removal. For laser pulses in the microsecond domain, material removal typically occurs concurrently with the irradiation of the target. A generic description of such processes is provided by models that assume that a fixed energy density,  $h_{abl}$ , is required for the removal of a unit mass of tissue. This assumption is adequate to describe a continuous ablation process because it

results in a rate of material removal that balances the irradiance delivered to the tissue. It is also assumed that material removal begins soon after the beginning of laser irradiation and proceeds during the entire laser pulse. Once this threshold is exceeded, such a model predicts a linear dependence between the etch depth and incident radiant exposure. The slope of the etch depth versus radiant exposure curve depends solely on the assumed value for the ablation enthalpy,  $h_{abl}$ , as [42, 52]

$$\delta = \frac{F_0 - F_{th}}{h_{abl} * \rho} \quad (1.5)$$

Note that in the steady-state model, there is no explicit dependence of the etch depth on absorption coefficient and there is a direct relationship between the threshold radiant exposure and ablation enthalpy. The steady-state model is valid only for microsecond (or longer) pulse durations and is not valid if the ablation process is characterized by a succession of stages with different ablation enthalpies [42].

The applicability of the blow-off and steady-state models to ablation data is often not evident. This arises because the assumptions made in the heuristic models are often not satisfied. For example, although the steady-state model is expected to be valid at high fluence, it is at these radiant exposures that shielding effects by the ablation plume or by plasma formation become most prominent and are not accounted for by the simple assumption of a constant ablation enthalpy. Another characteristic limiting the applicability of the steady-state model is that at low radiant exposures, material removal may consist of various distinct phases; and thus possesses an unsteady character [42, 47].

Due to the significant limitations of the heuristic models, many researchers have developed different models by considering the mechanisms underlying the ablation process or by considering the dynamics of groups of molecules. However, to understand the mechanisms underneath, it is very difficult when dealing with the complexity of phase transition processes and the significant dynamic changes of tissue properties in the ablation process. For simplicity, the initial mechanistic models – the steady-state vaporization models - ignored the explosive characteristics of the material removal process and instead treated ablation as rapid laser vaporization or boiling of tissue. Later thermomechanical models were developed to consider the dynamics of the ablation process as well as the impact of mechanical tissue properties.

Early models for the laser ablation process in tissue were inspired by treatments developed to describe the ablation of metals. These models treated ablation as a rapid vaporization process and reduced the process to a moving boundary problem, during which the metal surface possessed a fixed vaporization temperature. The first comprehensive model developed specifically for tissue ablation was presented by McKenzie [53-55]. He developed a general relationship between the laser parameters used to create a laser excision and both the temperature profile developed inside the tissue and the resulting extent of thermal injury. But the thermal diffusions following the laser pulse has not been considered. Other investigators developed models to include the thermal diffusion effect and provided predictions for threshold radiant exposure and material removal consistent with the vaporization enthalpy of water modified by losses associated with thermal diffusion. However, these predictions typically do not fare very

well when compared to experimental measurements. This is because of the prominence of phase explosions, confined boiling, and the effects of photomechanical transients and the tissue matrix on the ablation process. These limitations stimulated the construction of thermomechanical models that integrate the effects of photomechanical processes and tissue mechanical properties on the material removal process.

Similar to the steady-state vaporization model, the first comprehensive attempt at integrating mechanical effects into a steady-state model of the tissue ablation process drew upon models developed for the ablation of metals [56]. And later this approach was continued in tissue ablation [57-59]. In this model, tissue is considered to be capable of undergoing two phase transition processes - one from solid to liquid phase and one from liquid to vapor phase. The solid-liquid phase transition is postulated to occur upon thermal denaturation, at which point the tissue is thought to lack mechanical integrity and “flows” under the action of a shear stress or pressure gradient. This opens the possibility that recoil pressures produced by tissue vaporization would provide for the ejection of denatured tissue “liquid”, and enables material removal with ablation enthalpies lower than the vaporization enthalpy for water. The model treated the thermodynamics of the vaporization process rigorously to describe the relationship between the recoil pressure and temperature at the tissue surface. The dynamics associated with the liquid ejection was modeled using the Navier-Stokes equations. However, the model does not consider phase explosions or confined boiling as driving the ablation process and liquid or material ejection acts as a byproduct of the recoil forces produced by surface vaporization [42]. In a more realistic approach, the process of confined boiling is modeled by

considering the thermodynamic behavior of tissue water when it is heated within an elastic tissue extracellular matrix [60]. This was the first attempt at modeling explosive material removal as the primary process of tissue ablation. The model accurately predicts that explosive material removal can be initiated without supplying the entire enthalpy of vaporization. However, the model considers only the initiation of explosive material removal and does not consider the ablation process at fluence larger than the ablation threshold. These advances notwithstanding, significant work remains for the development of a mechanistic ablation model. As a result, assessment of the ablation threshold, enthalpy, and efficiency, within the context of the heuristic models, is still valuable and remains in prevalent use.

In the situation where the analytical description of the laser ablation of tissue is hindered by the complexity and diversity of the processes involved in the phenomenon, molecular dynamic simulation can provide useful information and is becoming a viable complementary approach to model and understand ablation processes with the development and advances in computational power [44, 61-63]. Computation of molecular dynamics offers predictions of the motion of molecular units produced by the deposition of laser energy. In these computations, macroscopic thermodynamic constraints are not imposed explicitly. Instead, ablation arises as a natural consequence of molecular interactions governed by the implementation of the equations of motion, intermolecular interactions, energy transfer, and molecular excitation within the model system. The molecular dynamics approach yields a wealth of information regarding the time evolution of both the size and velocity distributions of the ablation products that is

difficult to obtain by other means. These simulations reveal the volumetric nature of the ablative material removal process, in which small and large clusters leave the material bulk from locations not limited to those on the material surface. This is quite distinct from evaporative and desorption processes, in which material removal tends to occur strictly from the surface of the bulk material and consists predominantly of single molecules. The molecular dynamics approach has already provided valuable insight into the microscopic dynamics of desorption/ablation of both homogeneous and heterogeneous materials and is thus well suited to provide insight into the ablation dynamics of biological tissues [42]. The advantage of this approach is that only details of microscopic interactions need to be specified, and no assumptions are made about the character of the processes under study.

Several models have been proposed to explain the physical phenomena involved in plasma-mediated ablation [64-66]. Most of them focused on the main physical parameter at the very threshold of the breakdown, such as the electric field strength. The amplitude of the electric field, on the other hand, is related to the power density or intensity in the focus of the laser beam. For power densities far above the threshold value, most theories could fairly well describe the observed experimental results. However, at power densities close to the threshold value, none of them could give a detailed explanation of the influence of the laser pulse parameters. And a square root dependence of the threshold power density or pulse duration was observed when using picosecond or nanosecond laser pulses for inorganic materials [67-69] and various biological tissues [70-72].

Researchers later render a consistent theory to develop the optical breakdown model based on the Drude model to describe the temporal evolution of the volumetric density of free electrons, and to calculate breakdown thresholds for various laser parameters [73-77]. It starts with a basic rate equation, describing generation and losses of free electrons. The generic form of such a rate equation is

$$\frac{\partial \rho}{\partial t} = \left( \frac{\partial \rho}{\partial t} \right)_{mp} + \left( \frac{\partial \rho}{\partial t} \right)_{ch} + \eta_{casc} \rho - g \rho - \eta_{rec} \rho^2 \quad (1.6)$$

where the free electron density  $\rho$  is a function of time. The first three terms on the right hand side represent the production of free electrons through multiphoton, chromophore and cascade ionizations, respectively. The last two terms are the electron losses through diffusion out of the focal volume and recombination, respectively. The cascade ionization rate and the diffusion rate are proportional to the number of existing free electrons. The recombination rate is proportional to  $\rho^2$ , as it involves an interaction between two charged particles (an electron-hole pair). A detailed description of the individual terms of Eq. (1.6) was given by Noack and Vogel [77]. Several investigations based on the above rate equation have neglected multi-photon ionization, recombination, or diffusion, and only four terms of the rate equation were all considered in a few studies. While many of the early studies were focused on calculation of the breakdown thresholds, recent numerical simulations also include an analysis of the time evolution of the electron density during the laser pulse, the irradiance dependence of the free-electron density, the plasma absorption, and the volumetric energy density in the plasma.

However, the basic mechanisms underneath plasma-mediated ablation are still not conclusive. Plasma-mediated ablation occurs at very short temporal and spatial scales, involving complicated optical, thermodynamic, energy transfer, and mechanical processes which are closely coupled. Simultaneously, the target area could be heated to extremely high temperature and pressure, where the properties of the materials become unknown. The fundamental understanding of laser interaction with materials has been a goal of intense research for the last few decades. Though various researches on the mechanisms of laser multi-photon absorption, material excitation and plasma formation, as well as its removal and expansion, have been done, none of them can be considered exhaustive.

### ***1.5. Research Contributions***

The main contribution of this research is

- The parametric experimental study of the USP laser ablation of polymer (PDMS) material with single spot and single line ablation and determination of the ablation threshold and incubation factor.
- The development of proper ranges of laser parameters for PDMS separation and thin layer separation and 3-D micro-fabrication demonstration for potential applications in micro-fluidics and tissue engineering.
- The parametric experimental study of wet human dermis and freeze-dried dermis



ablation characteristics and determination of the ablation thresholds and incubation factors.

- The thermal damage investigation via experimental and analytical investigation for relation between thermal damage zone and laser parameters.
- The development of proper ranges of laser parameters for tissue separation and micro-processing.
- The innovations of using USP laser to separate wet dermis tissue and strip freeze-dried dermis tissue with no visible thermal damage for tissue implantation and biomedical surgery applications.
- The initial experiment development and modeling of near-field fabrication assisted by monolayer nano-particles.

## **1.6. Overview of the Dissertation**

The dissertation is organized as follows: Chapter 1 reviews the mechanism of laser tissue interaction and introduces different models that represent the physics of the processes and predictions of quantities in the processes. The development and application of laser technique is briefly covered. Chapter 2 deals with the laser polymer ablation, thin layer separation and micro-fabrication. Chapter 3 describes the experimental work carried out to study the wet tissue ablation with USP laser, separation demonstration via the USP

laser ablation and the thermal damage check by histological analysis. Chapter 4 studies the ablation feature on freeze-dried dermis sample and thin layer stripping via the USP laser ablation. Chapter 5 presents the theoretical analysis with 1D model to obtain the analytical formulation between laser parameters and the thermal damage zone and the comparison with experimental results. Chapter 6 presents the experimental and simulation study of near-field nano-fabrication via spherical and cylindrical particle on substrates. Chapter 7 summarizes the work contained in this dissertation and comments on future directions where this research can be applied and developed.

**Table 1.1. Ablation Threshold for Different Materials and Lasers Parameters.**

<b>Material</b>	<b>Laser Wavelength</b>	<b>Laser Pulse Duration</b>	<b>Ablation Threshold</b>	<b>Remark</b>
Dielectrics	1053 nm	0.4 ps	BaF <sub>2</sub> : 1.6 J/cm <sup>2</sup> CaF <sub>2</sub> : 2.0 J/cm <sup>2</sup> MgF <sub>2</sub> : 2.1 J/cm <sup>2</sup> LiF <sub>2</sub> : 2.6 J/cm <sup>2</sup>	Single spot Damage threshold [78]
Indium-tin-oxide film	775 nm	150 fs	0.7 J/cm <sup>2</sup> (5.3 $\mu$ m focus spot ) 0.95 J/cm <sup>2</sup> (10.6 $\mu$ m focus spot)	Single spot [79]
			0.76 J/cm <sup>2</sup> (3.6 $\mu$ m focus spot) 0.71 J/cm <sup>2</sup> (6.3 $\mu$ m focus spot) 0.82 J/cm <sup>2</sup> (11 $\mu$ m focus spot)	Incubation factor: 0.6469, 0.779, 0.7745 Line scanning [79]
Silicon carbide (3C-SiC)	800 nm	120 fs	0.97 J/cm <sup>2</sup> (low fluence) 3.29 J/cm <sup>2</sup> (high fluence)	Single spot [80]
Sapphire	775 nm	150 fs	3.27 J/cm <sup>2</sup> (single pulse)	Single spot [81]
Polyimide(PI)	800 nm	150 fs	1.0 J/cm <sup>2</sup> (single pulse) 0.5 J/cm <sup>2</sup> (100 pulses)	Incubation factor: 0.87 Single spot [82]
Borosilicate glass	780 nm	200 fs	4.1 J/cm <sup>2</sup> (single pulse in vacuum) 2.6 J/cm <sup>2</sup> (single pulse in air) 1.7 J/cm <sup>2</sup> (multi pulse in vacuum and air)	Single spot [83]
Metals	775 nm	150 fs	Stainless steel: 0.1600 J/cm <sup>2</sup> Niobium: 0.1460 J/cm <sup>2</sup> Titanium: 0.1021 J/cm <sup>2</sup> Copper: 0.3529 J/cm <sup>2</sup>	Multi-shot [10]

Polycarbonate(PC) Poly(methylmethacrylate) (PMMA)	400 nm	90 fs	PC: 0.20 J/cm <sup>2</sup> PMMA: 0.57 J/cm <sup>2</sup>	Incubation factor: 0.68 & 0.61 Single spot [84]
Au film	775 nm	148 fs	0.66 J/cm <sup>2</sup> (single pulse) 0.39 J/cm <sup>2</sup> (5 pulses) 0.30 J/cm <sup>2</sup> (10 pulses) 0.22 J/cm <sup>2</sup> (100 pulses)	Incubation factor: 0.765 Single spot [85]
Brain tissue	1053 nm	35 ps	20 J/cm <sup>2</sup>	[12]
Bovine neural tissue	630 nm	100 fs - 3 ps	1.5 J/cm <sup>2</sup> (100 fs) 5.3 J/cm <sup>2</sup> (3 ps)	Area scan [14]
Dental enamel	780 nm 800 nm	150 fs 95 fs	2.2 J/cm <sup>2</sup> (same for 95 fs and 150 fs) 1.0 J/cm <sup>2</sup> (95 fs & 400 nm)	Area scan [30]
Water	800 nm	130 fs - 10 ps	3.6 J/cm <sup>2</sup> (130 fs) 10.9 J/cm <sup>2</sup> (10 ps)	Single spot [31]
Dentin	800 nm	130 fs - 20 ps	0.75 J/cm <sup>2</sup> (130fs) 3.8 J/cm <sup>2</sup> (20ps)	Single spot [31]
Human skin	2940 nm	250 $\mu$ s	1.6 J/cm <sup>2</sup>	Single spot [86]
Porcine cornea	1030 - 1041 nm	800 fs - 20 ps	0.73 J/cm <sup>2</sup> (800 fs) 1.15 J/cm <sup>2</sup> (1.63 ps) 1.57 J/cm <sup>2</sup> (2.86 ps) 4.8 J/cm <sup>2</sup> (20 ps)	Single spot [32]
Fresh calf brain tissue	1053 nm	20 ps	20 J/cm <sup>2</sup> (in air) 29 J/cm <sup>2</sup> (in distilled water and physiological saline)	Area scan [33]
Cortical bone	820 nm 1064 nm	225 fs 20 ps	3.5 J/cm <sup>2</sup> (225 fs) 80 J/cm <sup>2</sup> (20 ps)	Single spot [87]

Human cornea and Hard and soft tissue	620 nm	1 ps	Human cornea: $2.2 \text{ J/cm}^2$ (350 fs), $40 \text{ J/cm}^2$ (200 ps) Human enamel: $1.1 \text{ J/cm}^2$ (100 fs), $10 \text{ J/cm}^2$ (35 ps) Bovine brain tissue: $1.5 \text{ J/cm}^2$ (100 fs), $20 \text{ J/cm}^2$ (35 ps)	[88]
Corneal tissue and water	620 nm	150 fs	Human corneal tissue: $1.3 \text{ J/cm}^2$ Water: $0.87 \text{ J/cm}^2$	[89]
Cortical bone	775 nm	200 fs	$0.69 \text{ J/cm}^2$ (775nm) $0.19 \text{ J/cm}^2$ (387nm)	Single spot [90]
Neocortex of rat	760 nm	120 fs	$3 \text{ J/cm}^2$	Single spot & line ablation [91]

## **Chapter 2.**

# **Polymer (PDMS) Thin Layer Separation and 3-D Micro-fabrication by USP Laser Internal Ablation**

### ***2.1. Introduction***

Recently, more interests have been gained in the field of micro-systems such as in the life sciences with applications like DNA sequencing or clinical diagnostics. In these micro-systems, disposable devices on a biocompatible substrate are in great demand. These devices often require large surface areas to allow either a massively parallel processing of samples or long micro-channel length for good analysis performance. In contrast to the substrates silicon, glass, or quartz, which is still used in most micro-fluidic systems, polymers offer a variety of advantages: the wide range of material properties and surface chemistries, normally low costs and low conductivity. Besides, biodegradable polymeric scaffolds have a significant impact on medical technology, greatly enhancing the efficacy of many existing drugs and enabling the construction of entirely new therapeutic modalities. The development of next generation drug delivery and tissue engineering devices based on biodegradable polymers are contingent on the fashioning of features analogous to the size of cells and organelles.

Poly (dimethylsiloxane) (PDMS) has been one of the most widely used silicon-based polymers for MEMS, such as micro-fluidic systems [77, 92, 93]. It is also often

used as a base master material for nano-imprinting and soft lithography, which seems to be a rather promising technique for mass production of micro- or nano-scaled biodegradable polymer pattern for tissue engineering. Its applications range from contact lenses and medical devices to elastomers [94].

The commercialization of micro-system technology requires low-cost micro-fabrication methods with high-volume production capability. The current techniques for generating micro- and nano-patterns on polymeric materials such as soft lithography, stereolithography have many disadvantages as described in Chapter 1. Therefore, a low-cost, minimally invasive and rapid technique for polymers micro-fabrication, where the integrity of the polymeric substrate can be maintained after processing is needed.

Laser ablation has become a widely used technology for the fabrication of micro-fluidic devices. However, general long pulsed or CW laser can not be used for polymer micro-fabrication since the absorption coefficient is small because the polymer is usually transparent or semi-transparent. The situation is totally different for USP laser system. Contrast to thermal ablation with general laser, plasma-mediated ablation by USP laser is a completely different process of interaction when the power density is more than  $10^{11}$  W/cm<sup>2</sup> (in liquids and solids), which can be achieved easily in the focal spot of the laser beam for USP lasers since the pulse duration is ultra short. The extremely high intensity of powerful ultra-short pulses will lead to the rapid generation of free electrons in a very short time and finally results in the transformation of the material into plasma that will continue to absorb energy from the laser pulses causing immediate vaporization.

Furthermore, plasma-mediated ablation is material-independent and it can ablate materials that are normally difficult to ablate by conventional lasers, such as transparent or low absorption materials like polymer (PDMS). Thus, material-dependent absorption usually seen with long pulsed laser is no longer a limitation and processing of almost any type of materials via the so-called USP laser plasma-mediated ablation is possible. Compared with the thermal interaction by general long pulsed or CW lasers, plasma-mediated ablation by USP laser has great advantages to remove precise amount of materials with minimum thermal damage to the surrounding materials since the power duration is so short that the plasma expansion happens on a timescale smaller than the rate of energy transfers to the adjacent material, and thermal damages are reduced or eliminated. The so-called plasma-mediated ablation occurs when the incident energy flux is over the threshold for optical breakdown and the ablation threshold is usually defined as the minimum fluence at which the free electron density reaches the critical electron density.

Although laser ablation of real tissues [14], glasses [20] and polymers [95, 96] have been extensively studied in recent years, studies on USP laser thin-layer separation and micro-fabrication of polymer materials such as PDMS have not been reported in the literature. Meanwhile USP laser micro-fabrication of polymer also shows the potential in developing artificial vasculature in tissue engineering, and such structures would be difficult to achieve by using conventional fabrication methods. The objectives of this research include: 1). a fundamental study of single spot ablation and single line surface scanning ablation of PDMS; 2). Parametric studies for PDMS separation and



demonstration of PDMS thin layer separation; 3). PDMS 3-D micro-fabrication by USP laser internal ablation.

## ***2.2. Materials and Methods***

### **2.2.1. Experimental Set up**

The experimental setup is sketched in Fig. 2.1 and it compromises four major systems: a commercial USP laser system, a beam delivery system, an automated motion system, and a whole control system. The UPS laser system is an erbium doped fiber laser (Raydiance, Inc.) consisting of a seed box, an amplifier box, and a chiller. Its lasing wavelength is centered at 1552 nm. The output pulses have a pulse width 900 fs. The pulse repetition rate is tunable between 1 Hz and 500 kHz. The direct output pulse energy is adjustable between 1.0 and 5.0  $\mu\text{J}$ .

The beam delivery system is made up of a beam blocker, an astigmatism correction periscope (mirror) and an objective lens (Mitutoyo M Plan Apo NIR 20X,  $NA = 0.40$ ,  $f = 20$  mm). The measured focal spot size for the current laser system is about 8.0  $\mu\text{m}$ . A digital power meter was used to measure the laser power loss in the beam delivery system and found that the total loss is 50%. Such a loss has been accounted for in the irradiation pulse energy values stated hereafter.

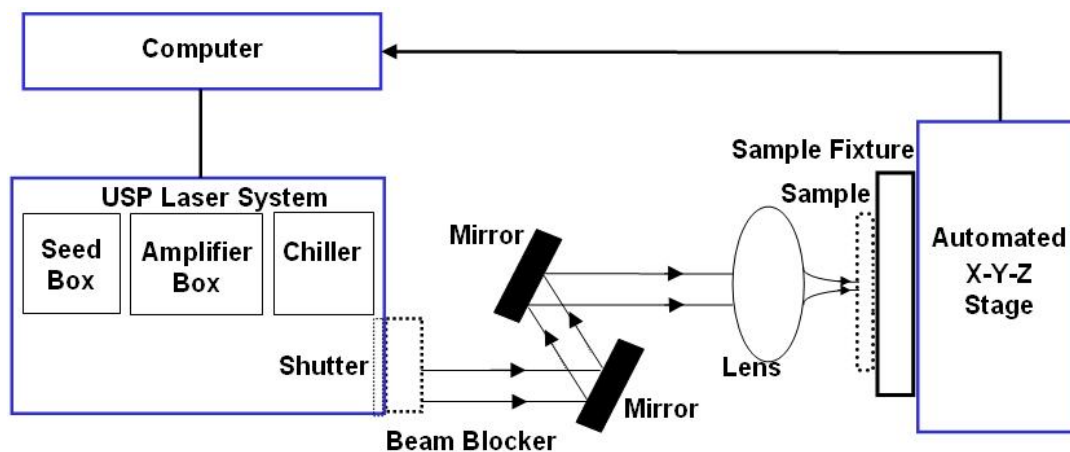


Figure 2.1. Sketch of the Experimental Setup.

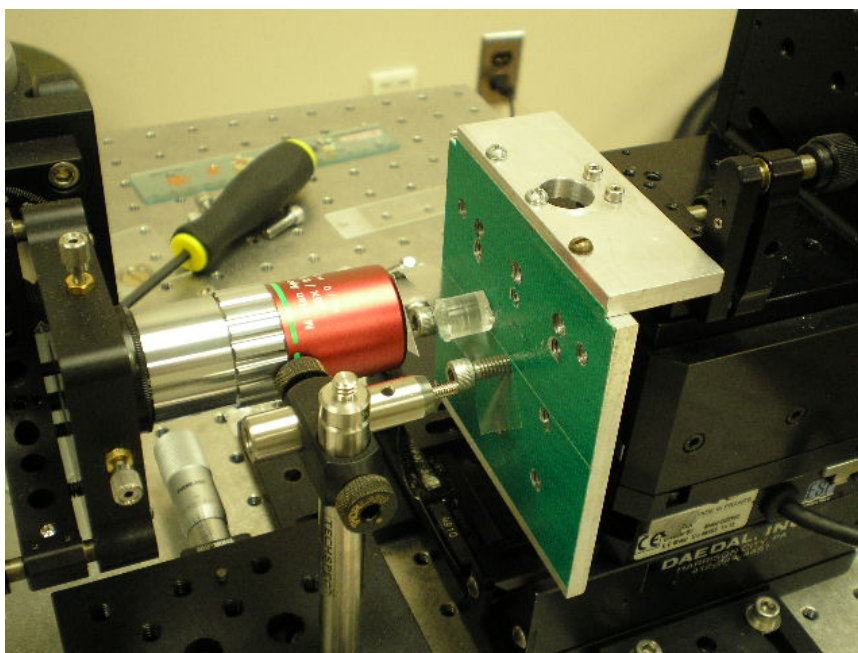


Figure 2.2. Photos of Sample Fixture and Motion Stage Setup.

The automated motion system (see Fig 2.2) is composed of a lab-made fixture for holding PDMS samples and a 3-axis motorized high-speed high-precision translation stage (VP-25XA, Newport) for adjusting the laser beam focusing position and for

performing line and area scanning. The whole control system is a commercial RayOSTM laptop interface for controlling laser output parameters and for programming the motion pattern of the 3-axis stage. All the experiments presented here were conducted in free space. During surface ablation processes an evacuator system (FX225, EDSYN) which is not shown in Fig. 1 was also employed to collect plasma plume residue and debris.

### **2.2.2. Sample Preparation**

PDMS samples were prepared by Dow Corning Sylgard Elastomer 184 Kit. Proper amounts of PDMS base and curing agent were taken by weighing scale 10: 1 and mixed well to a milky color consistency. The mixture was put into a vacuum chamber to evacuate the bubbles generated during mixing. The degassed PDMS assembly was placed on a hotplate at 65 °C for 4 hours upon completion of the curing cycle. The refractive index of PDMS is determined by the curing time and temperature [97]. At wavelength 1552 nm the current PDMS has a refractive index 1.45. Measurement of the laser beam passing through the PDMS 1 mm thick gave a 15% attenuation loss.

### **2.2.3. Measurements**

The micro topography of the ablated PDMS lines, surfaces and channels were observed and characterized with an upright digital microscope (National Optical DC3-156-S) and a scanning electron microscopy (SEM, AMRAY 1830I). A surface profiler (Dektak 3030) was also utilized to measure the thickness of the separated PDMS thin layers.

## **2.3. Results and Discussion**

### **2.3.1. Fundamental Study of PDMS Ablation**

The ablation threshold of the PDMS samples via the current experimental setup should be determined first. We have conducted both PDMS surface single spot ablation and single line ablation to obtain the ablation threshold. For single spot ablation, the laser beam was focused on the surface of PDMS and for each target spot, single or multiple laser pulses were incident on the spot with constant 1 Hz repetition rate. Figure 2.3 shows the microscopic view of an ablated PDMS surface craters array. For each spot the laser beam was normally focused onto a PDMS sample surface. The number in the array column represents the number of pulses deposited in a single spot with a pulse repetition rate 1 Hz. The irradiation pulse energy (50% of the laser direct output) in the array rows varies from 0.75 to 2.5  $\mu\text{J}$ . Ablation damage is defined as any visible permanent modification to the surface observed by the microscope at 400X magnification. From Fig. 2.3 it is seen that a single pulse generates an ablation crater when the irradiation pulse energy is not less than 1.5  $\mu\text{J}$ . However, it needs two or four continuous pulses to generate a visible ablation crater when the irradiation pulse energy is 1.0  $\mu\text{J}$  or 0.75  $\mu\text{J}$ , respectively.

Figure 2.4 shows the measured average ablation crater diameters for different irradiation pulse energies with different pulse numbers. It is found that the crater diameter enlarges as the pulse energy or pulse number increases.

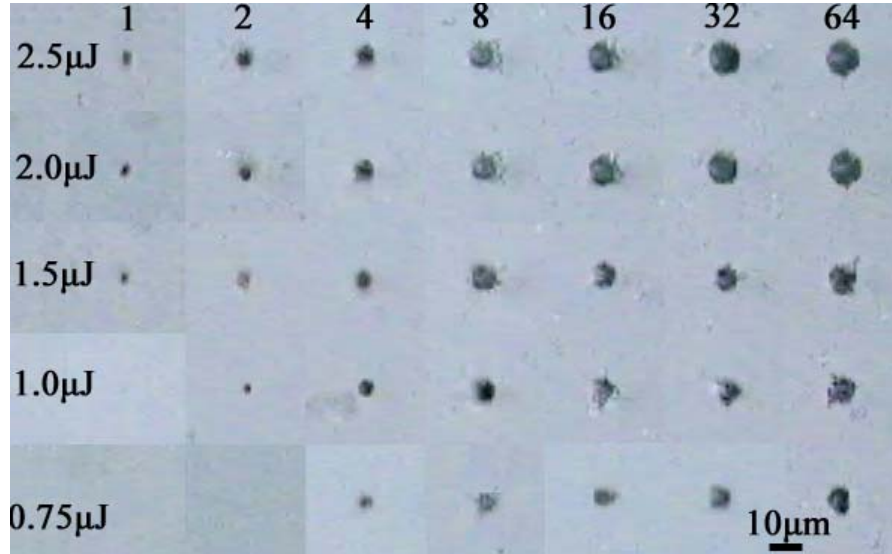


**Figure 2.3. Microscopic View (400X) of an Ablation Craters Array on PDMS Surface for Single Spot Ablation.**

For laser pulses with a Gaussian spatial beam profile, the maximum irradiation fluence  $F_0$  can be calculated from the irradiation pulse energy  $E$  and the beam focus radius  $r$  as

$$F_0 = \frac{2E}{\pi r^2}. \quad (2.1)$$

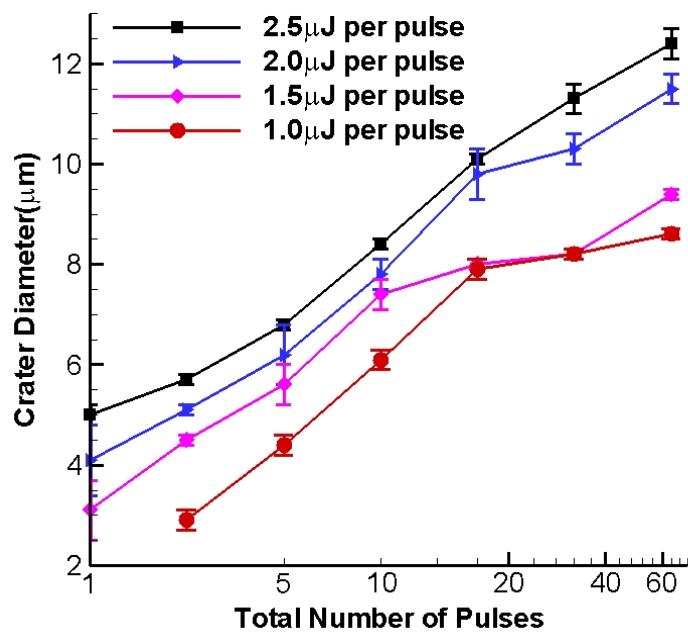
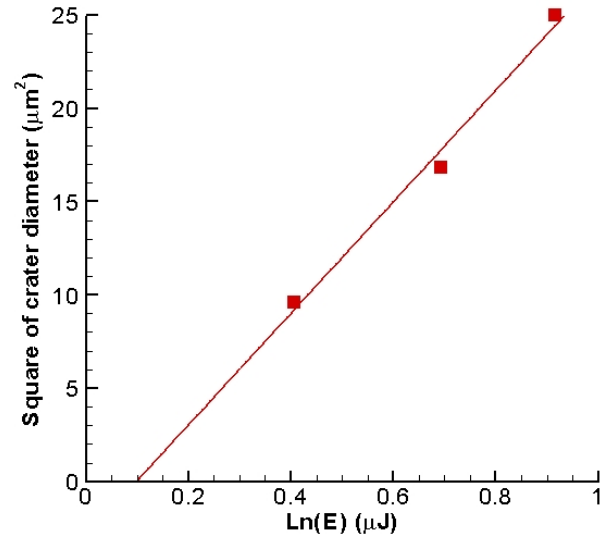
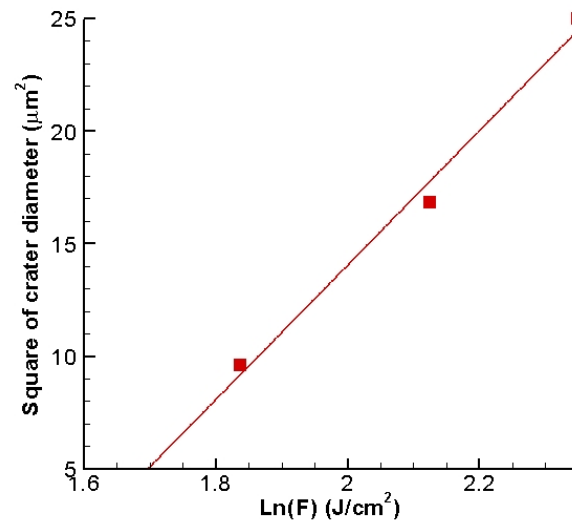


Figure 2.4. Effects of Pulse Number and Energy on Ablation Crater Diameter.



(a)



(b)

**Figure 2.5. (a) Square Diameter of the Single Pulse Ablation Crater versus the Incident Pulse Energy for Effective Focal Radius; (b) Square Diameter of the Single Pulse Ablation Crater versus the Irradiation Pulse Fluence for Ablation Threshold.**

If the maximum fluence ( $F_0$ ) exceeds the ablation threshold fluence ( $F_{th}$ ), then the squared diameter ( $D^2$ ) of the ablation crater is correlated with  $F_0$  by [82]

$$D^2 = 2r^2 \ln\left(\frac{F_0}{F_{th}}\right). \quad (2.2)$$

Therefore, it is possible to determine the Gaussian beam radius and the ablation threshold by plotting the diameter of the single pulse ablation crater versus the incident pulse energy. This technique is well described in ref. [82]; and thus, not repeated here. As shown in Fig. 2.5, the focal beam radius in the ablation spot is determined to be  $r = 3.9 \mu\text{m}$  and the ablation threshold of the PDMS with single pulse irradiation is calculated as  $F_{th} = 4.62 \text{ J/cm}^2$  for the current laser and optical system. This calculated beam focus diameter value ( $2r = 7.8 \mu\text{m}$ ) is close to the measured value ( $8.0 \mu\text{m}$ ). Rubahn *et al.* [98] summarized the ablation thresholds of PDMS for various nanosecond lasers and found that the ablation threshold of PDMS increases with increasing ablation wavelength from ultraviolet (UV) to near-infrared.

For ablation with multiple pulses, the effect of incubation attributed to increased absorption due to accumulation of damage or defects from individual pulses tends to reduce ablation threshold. A relationship between the multi-pulse ablation threshold  $F_{th}(N)$  and the single-pulse ablation threshold  $F_{th}(1)$  is given by the accumulation model [99]

$$F_{th}(N) = F_{th}(1)N^{\xi-1}, \quad (2.3)$$



where  $N$  is the number of irradiation pulses and the exponent  $\xi$  is the so-called incubation factor. This factor depends on both the material and laser properties. Figure 2.6 shows the experimental data for  $\ln(NF_{th}(N))$  versus  $\ln(N)$  and a least squares fitting line from which the slope yields an incubation factor  $\xi = 0.52$  for the PDMS.

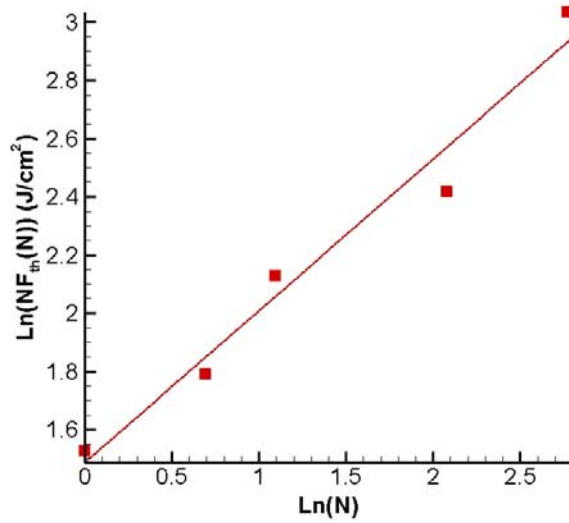


**Figure 2.6. Multi-pulse Incubation Effect on PDMS Single Spot Ablation.**

To enable practical thin-layer separation and micro-fabrication, the ablation features of line scanning must be understood because the continuity and quality of an ablation line depend on the overlap of many individual ablation craters. Meanwhile, surface single line scanning ablation test was also studied to compare and verify the ablation threshold results with single spot ablation. For each line scanning line, the stage moving speed is constant and the pulse energy and repetition rate vary. To this end, the pulse repetition rate and the moving speed of work stage are two key factors. These two factors can be combined into one parameter - pulse overlap rate, which is the ratio of the

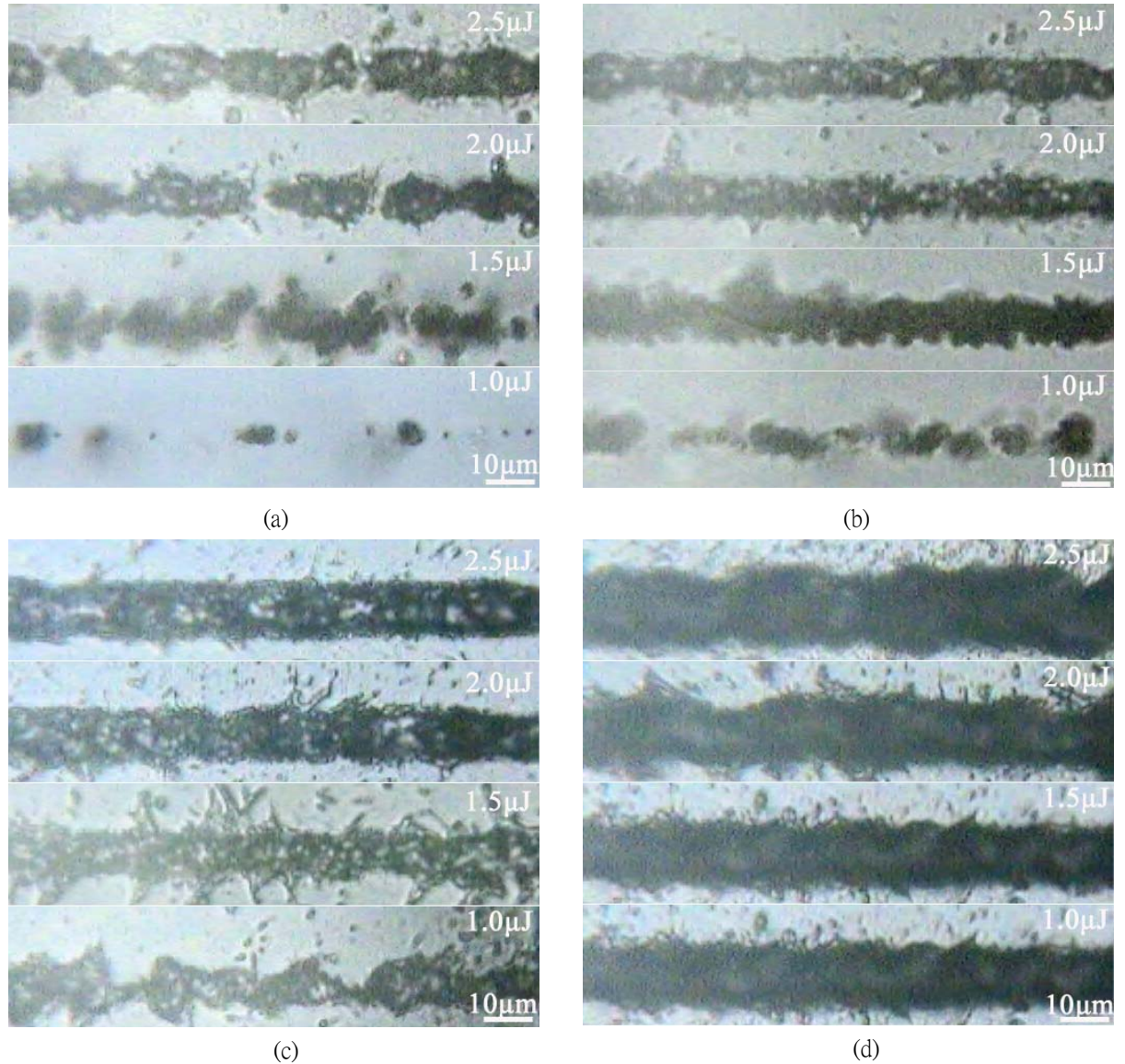
pulse repetition rate -  $f$  over the stage moving speed -  $s$ , and it represents the pulse number per unit moving distance.

Figure 2.7 shows the single line scanning results at PDMS surface with different pulse overlap rates and various pulse energies. Each line was scanned only once. In Fig. 2.7(a) where the pulse overlap rate is 0.2 pulse/ $\mu\text{m}$ , no continuous ablation line is observed. In the case with 1.0  $\mu\text{J}$  irradiation pulse energy, only about 30% of the line scanning area has been ablated. Even in the case with the maximum irradiation pulse energy (2.5  $\mu\text{J}$ ) there is yet un-ablated area in the scanning line. In Fig. 2.7(b), the pulse overlap rate increases to 0.5 pulse/ $\mu\text{m}$ ; then only one ablation line with low irradiation pulse energy (1.0  $\mu\text{J}$ ) is broken. Further increasing the pulse overlap rate to 2 and 10 pulses/ $\mu\text{m}$ , all the ablation lines are continuous as shown in Figs. 2.7(c) and (d), respectively. However, it is noticed that the ablation lines in Fig. 2.7 (d) are very dark, where thermal damage may be a concern.

Figure 2.8 plots the measured average single ablation line width versus the irradiation pulse energy for three different pulse overlap rates. The line width uncertainty is due to two main factors: crater boundary and wavy motion ( $\pm 1 \mu\text{m}$ ) of the translation stage. It is seen that the ablation line width increases as the irradiation pulse energy and overlap rate increase. The results in Figs. 2.7 and 2.8 show that 2 pulses/ $\mu\text{m}$  is a proper pulse overlap rate for line ablation.

Compared with the single spot ablation, an ablation line consists of continuously

ablated craters along the laser scanning direction. When the pulse overlap rate is so intense that no individual crater can be distinguished, the ablation line width is then equivalent to the diameter of the ablated crater ( $D$ ) generated by  $N$  repeated pulses. The equivalent pulse number can be approximated by Eq. (2.4):



**Figure 2.7. Microscopic View (1000X) of Ablated Single Lines at PDMS Surface with Different Pulse Overlap Rates and Various Irradiation Pulse Energies.**

(a) 0.2 pulse/μm, (b) 0.5 pulse/μm, (c) 2 pulses/μm, and (d) 10 pulses/μm.

$$N = 2r_{\text{eff}}f / s . \quad (2.4)$$

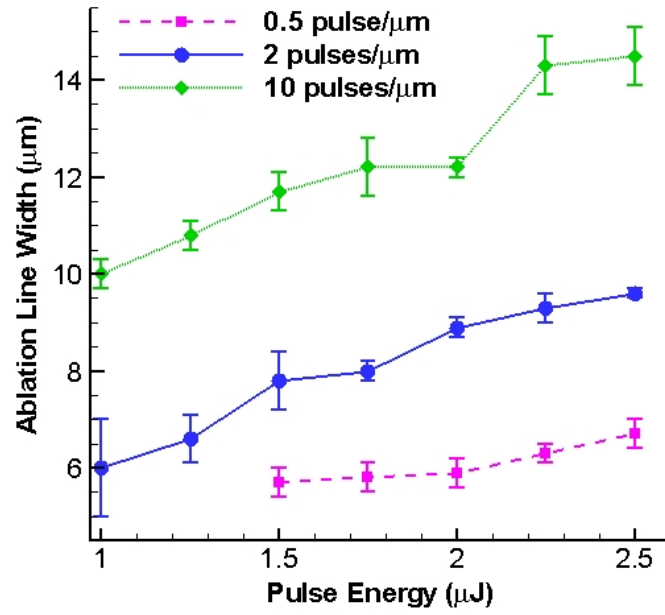
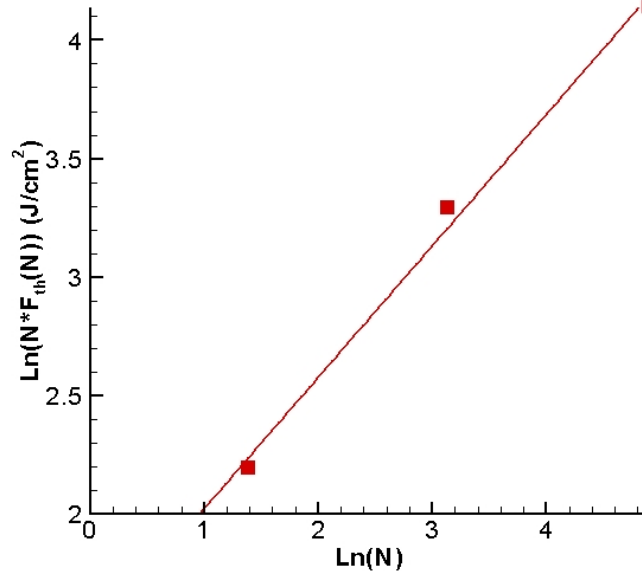


Figure 2.8. Plots of the Single Ablation Line Width versus the Irradiation Pulse Energy.



**Figure 2.9. Incubation Effect on PDMS Single Line Ablation with Different Pulse Overlap Rate.**

For each scanning line, three samples were selected to obtain average ablation line width, which is equivalent to  $D$ . And therefore, it is possible to determine the Gaussian beam radius and the ablation threshold by plotting the ablation line width versus the incident pulse energy similar to the single spot ablation, as shown in Fig. 2.10. Table 2.1 lists the specific focal spot radii and ablation thresholds for different pulse overlap rates. Then the slope of least squares fitting line yields an incubation factor  $\xi = 0.56$  as shown in Fig. 2.9 and the ablation threshold of the PDMS with single pulse irradiation is calculated as  $F_{th}(1) = 4.33 \text{ J/cm}^2$  from Eq. (2.3) for the surface single line ablation.

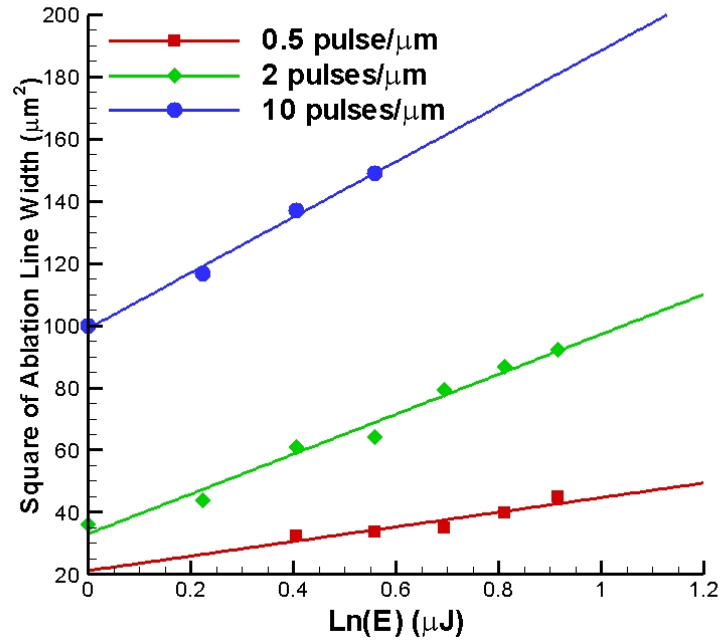


Figure 2.10. Ablation Line Widths versus Pulse Energy for Effective Spot Radius.

Table 2.1. Specific Focal Spot Radius and Ablation Thresholds for Different Pulse Overlap Rates

Pulse Overlap Rate (pulse/ $\mu m$ )	0.5	2.0	10
Focal Spot Radius ( $\mu m$ )	3.4	5.7	6.7
Accumulated Pulse Number ( $N$ )	4	23	134
Threshold $F_{th}(N)$ (J/cm <sup>2</sup> )	2.24	1.17	0.47

Comparing the incubation factor and  $F_{th}(1)$  for single spot and single line ablation experiments, both of them are close to each other and it means that both methods can be used to determine the ablation threshold and incubation factor. Which method is preferred depends on the laser energy level, the target material property and the difficulty

level for ablation feature measurement. For example for dermis tissue sample, because of the relatively high threshold, the tissue surface roughness and water content on the surface, it is hard to generate single spot crater and use the single spot ablation method, so single line ablation is preferred.

### **2.3.2. PDMS Separation and 3-D Micro-fabrication**

Before the PDMS separation, the overlap intensity must be controlled in order to increase working efficiency or to avoid any possible thermal damage due to over-deposition of energy. Hence, it is needed to find a proper pulse overlap rate for PDMS thin-layer separation and micro-fabrication. For separation tests, three big PDMS samples were prepared. Each sample was cut into 35 small blocks, with a similar dimension about 8 mm long, 2 mm wide and 6 mm thick. Each block was separation (internal area) scanned with laser beam focused 1 mm below surface. The translation stage moved at a constant speed of 10 mm/s along the block length direction. The scanning lines are spaced 2  $\mu\text{m}$  apart. For different blocks, the pulse repetition rate varied from 2 to 500 kHz, corresponding to a pulse overlap rate range between 0.2 and 50 pulses/ $\mu\text{m}$ . The surface irradiation pulse energy varied from 0.75  $\mu\text{J}$  to 2.5  $\mu\text{J}$ . Each test condition was repeated in three different sample blocks to minimize the impacts of performance fluctuation of the laser and the sample-to-sample variation.

**Table 2.2. Test of Laser Parameters for PDMS Separation Focusing 1 mm Inside PDMS.**

<b>Energy</b> <b>Overlap</b>	0.75 $\mu$ J	1.0 $\mu$ J	1.5 $\mu$ J	2.0 $\mu$ J
0.2 pulse/ $\mu$ m	☆□	☆□	★□	★□
0.5 pulse/ $\mu$ m	☆□	★□	★□	★■◆●
1.0 pulses/ $\mu$ m	☆□	★■◆●	★■◆●	★■◆●
2.0 pulses/ $\mu$ m	★□	★■◆●	★■◆●	★■◆●
5.0 pulses/ $\mu$ m	★■◆●	★■◆●	★■◇●	★■◇●
10 pulses/ $\mu$ m	★■◆●	★■◇●	★■◇●	★■◇●
50 pulses/ $\mu$ m	★■◇●	★■◇○	★■◇○	★■◇○

★: Ablation spark is observed.

◆: Ablated surface looks normal.

☆: No Ablation spark

◇: Ablated surface looks dark.

■: Can be separated into two layers.

●: No Obvious carbonized particle generated;

□: Can not be separated.

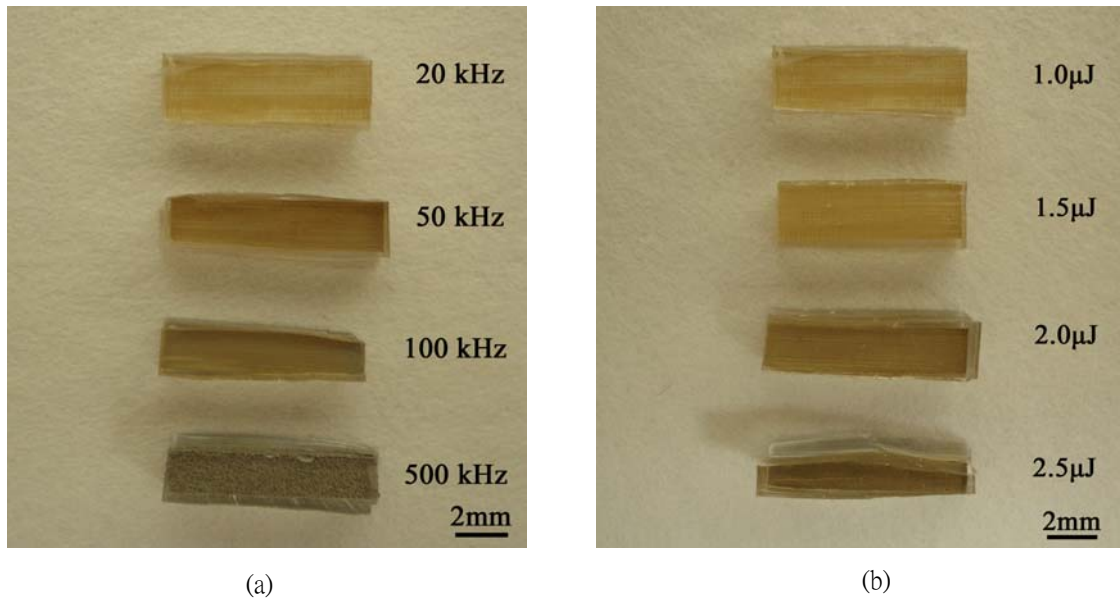
○: Obvious carbonized particle generated;

Table 2.2 shows the test results for these blocks separation scanned with different sets of laser parameters. Comparisons are available with regard to the following aspects: (1) whether ablation sparks are observed during the laser scanning process; (2) whether the block can be separated by tweezers after the scanning; (3) whether the ablation surface looks normal or dark; and (4) whether obvious carbonization at the separation surface is observed. From Table 2.2, it seems that a wide range of pulse overlap rate between 0.5 pulse/ $\mu$ m and 10 pulses/ $\mu$ m is all right for the PDMS separation. However, the selection of a proper pulse overlap rate must be in combination with the irradiation pulse energy. When the irradiation pulse energy is 0.75  $\mu$ J, for example, the pulse overlap rate should be in the range of 5 to 10 pulses/ $\mu$ m. When the irradiation energy is increased to 2.5  $\mu$ J, the pulse overlap rate should drop to the range of 0.5 to 1 pulse/ $\mu$ m. In terms of fabrication efficiency, it is preferred to reduce pulse overlap rate; and thus, apply high



pulse energy.

Figure 2.11 visualizes the separation scanned PDMS blocks with different sets of pulse repetition rate and irradiation pulse energy. The photos were taken immediately after the laser scanning, but before peeling off. Since PDMS is transparent against visible light, what visualized in the photos is the view of the separation interface. It is observed that the separation surface becomes darker and darker when the repetition rate increases from 20 to 500 kHz (i.e. pulse overlap rate from 2 to 50 pulses/ $\mu\text{m}$ ) or when the irradiation pulse energy increases from 1.0 to 2.5  $\mu\text{J}$ . In terms of minimization of possible thermal damage, it is more appropriate to operate at low laser pulse energy with a modest pulse overlap rate.



**Figure 2.11. Photos of the Separation Area Scanned PDMS Blocks.**

**(a) With a Constant Irradiation Pulse Energy 1.0  $\mu\text{J}$ , and (b) With a Constant Pulse Overlap Rate 2 pulses/ $\mu\text{m}$ .**

Separation of PDMS layers is based on the area scanning with laser focusing in the target depth. Figure 2.12 (a) visualizes the cutting interface of a PDMS block that was area scanned with beam focusing 1 mm inside, pulse overlap rate at 1 pulse/ $\mu\text{m}$  and surface irradiation pulse energy at 1.0  $\mu\text{J}$ . The interface layer depth is measured to be about  $20 \pm 3\mu\text{m}$ . This value is exactly twice of the analyzed depth of the beam focus for this laser and lens system [100]:  $\Delta z = \pm 0.32\pi r^2 / \lambda = \pm 10\mu\text{m}$  if we choose a typical spot size variation value 5%.

Figure 2.12 (b) shows the cutting interfaces at different layers inside one PDMS block with the laser beam focusing into different positions. The depth of the focus position under the PDMS surface is 1, 1.6, 2.2 and 2.8 mm, respectively for the cutting interfaces from number 1 to number 4 shown in Fig. 2.12 (b). We actually generated another interface at layer 0.4mm deep as well. It is not shown in Fig. 2.12 (b) because of the view limit of the microscope used. Clear ablation occurred at all layers. The interface patterns for all layers are quite similar. Since the cuts at different layers were generated in the same block, it demonstrated the feasibility of performing three-dimensional micro-fabrication.

Figure 2.12 (c) shows the ablation interface layer depths for different beam focusing positions from 0.4 to 2.8 mm inside the PDMS block. It is seen that the beam focusing position has slight effect on the ablation interface layer, because the beam focal spot size and depth are very weak functions of beam length inside PDMS [101] when the same objective lens is used. This also implies that the ablation threshold at any depth is a

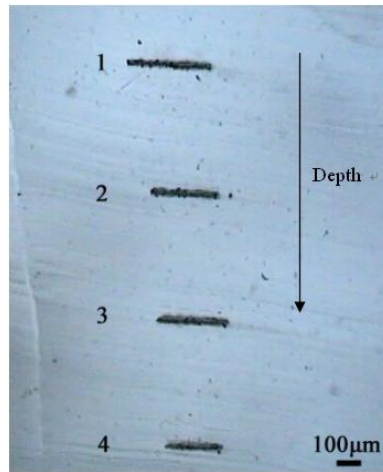
constant. It is worth mentioning that the laser intensity is attenuated with increasing depth because of light scattering and absorption in material. For PDMS, it is optical transparent; and thus, laser attenuation inside the PDMS is not a concern.

Figure 2.13 displays the ablation layer depths with different pulse repetition rates and pulse energies at a constant stage moving speed 10 mm/s. The beam was focused at 1mm deep in the block. It is seen that both the pulse energy and the repetition rate influence the ablation interface layer depth. The effect of pulse repetition rate is more pronounced when the repetition rate is over 40 kHz (i.e. pulse overlap rate 4 pulses/ $\mu\text{m}$ ). The ablation layer depth increases substantially from about 20 to 170  $\mu\text{m}$  as the pulse overlap rate increases from 4 to 25 pulses/ $\mu\text{m}$ .

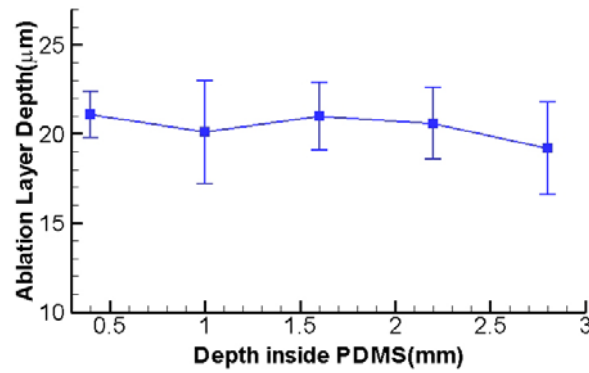
Figure 2.14 demonstrates PDMS layer separation after the laser scanning (2 pulses/ $\mu\text{m}$  and 1  $\mu\text{J}$ ), where a thin layer is completely peeled off from a PDMS block via tweezers. There is no visible thermal and mechanical damage to the two separated layers. The thin layer thickness was measured by a surface profiler (DEKTAK 3030) and it is 20.3  $\mu\text{m}$  thick on average. It has a very good uniformity with a fluctuation  $\pm 0.5 \mu\text{m}$  over the entire area.



(a)



(b)



(c)

**Figure 2.12. (a) Microscopic View (400X) of the Ablation Interface Across the Cross-section of a Separation Scanned PDMS Block (1 mm deep, 1 pulse/μm, and 1.0 μJ); (b) Microscopic View (40X) of Ablation Cuts at Different Depth Inside a PDMS Sample (1 pulse/μm and 1.0 μJ); and (c) A Plot of the Measured Ablation Interface Depth Versus the Laser Beam Focusing Depth Inside PDMS (1 pulse/μm and 1.0 μJ).**

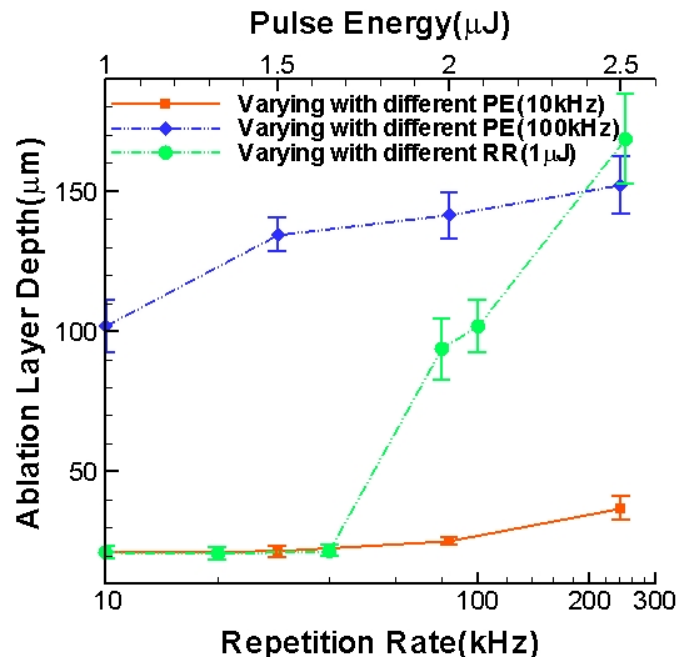
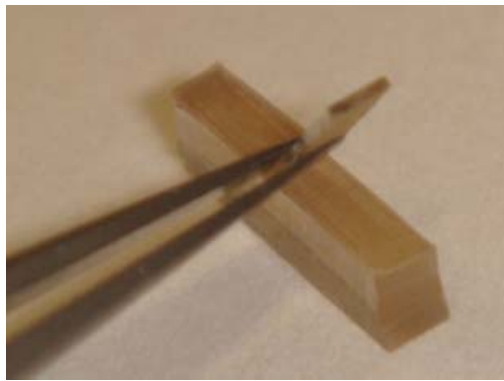
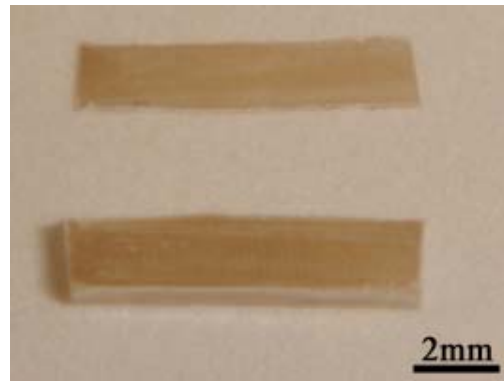


Figure 2.13. Ablation Line Widths versus Pulse Energy for Effective Spot Radius.



(a)



(b)

Figure 2.14. Demonstration of PDMS Thin Layer Separation (2 pulses/μm and 1.0 μJ).

(a) Peeling by Tweezers, and (b) The Separated Layers.

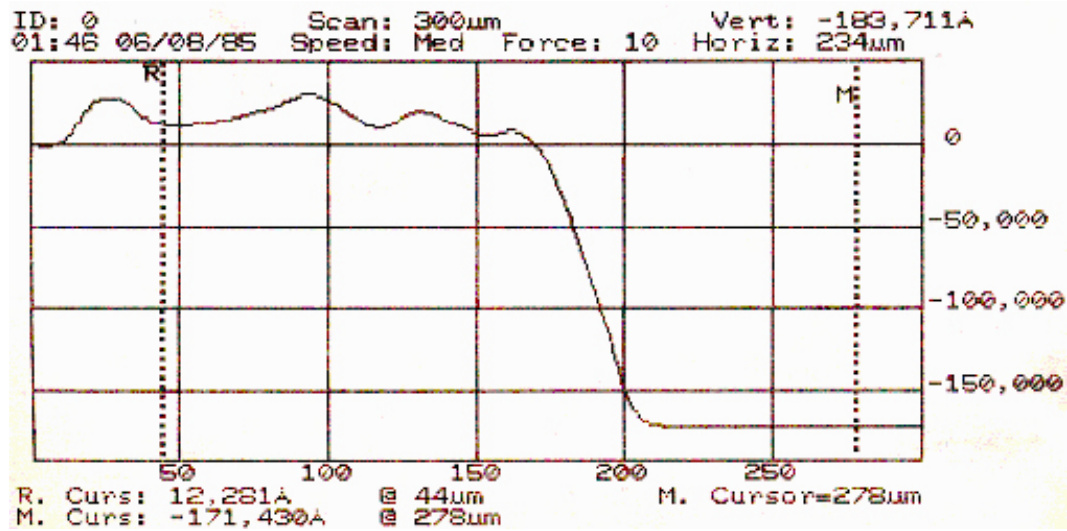


Figure 2.15. Surface Profilometer Measurement of Thin Layer PDMS Separation Thickness.

The thickness of the separated thin layer is controllable by adjusting the position of the laser beam focal spot under the PDMS sample surface as shown in Fig. 2.12 (b). The procedure consists of three steps: (1) the laser beam is aligned to be focused exactly on the PDMS sample surface, via the observation of optimal spark generation on the surface; (2) the sample on the translation stage is moved towards the lens (z-direction) for a distance identical to the target thickness; and (3) the sample is moved in the x-y plane to realize laser area scanning. Figure 2.15 shows one of the surface profilometer measurement results for the PDMS separation layer. Table 2.3 shows the measured thickness of the different tests. For the three tests with a target thickness of 20  $\mu\text{m}$ , the averaged thickness of the three samples is analyzed as  $20.6 \pm 1.7 \mu\text{m}$ . Thus, the fabrication is very precise.

Figure 2.16 shows the microscopy view of one PDMS separation surface with 5

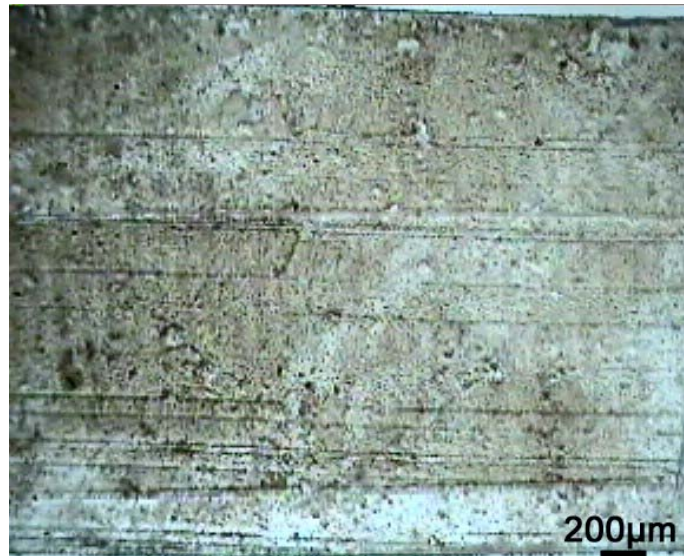
pulses/ $\mu\text{m}$  and  $1.0\ \mu\text{J}$ , and we can see that there are small particles on the separation surface and this is the ablation residue after the re-solidification of the ablated PDMS materials.

## ***2.4. Fabrication of Micro-channel Network***

Using the USP laser direct writing technique, a multi-width micro-channel network structure in PDMS was fabricated and illuminated in Fig. 2.17. Figure 2.17(a) shows the channel network after experiment and Fig. 2.17(b) shows that the fabricated channels are interconnected when the red dye flow was injected from left side of the network. Figure 2.17(c) shows the microscopy view of one of the junction of the channel network. The network is about 3.5 mm beneath the PDMS sample surface. The size of the channels varies from 50 to 400  $\mu\text{m}$ . The laser parameters used in the fabrication were 2 pulses/ $\mu\text{m}$  and  $1.0\ \mu\text{J}$ . The line scanning space was 2  $\mu\text{m}$  apart. The network structure could be significant for micro-fluidics. It also shows the potential of the current fabrication technique in developing artificial vasculature in tissue engineering. Such structures would be difficult to achieve by using conventional fabrication methods. For example, undercuts can not be directly done via the replication technology and use of a master is needed. However, the USP laser fabrication technique is simple and direct. It is also feasible to fabricate in three-dimension as demonstrated in Fig. 2.12 (b).

**Table 2.3. Thickness of the Separated Thin PDMS Layers (Dimension: 10mm × 2mm).**

Sample No.	Measured Thickness ( $\mu\text{m}$ )	Target Thickness ( $\mu\text{m}$ )	Fluctuation (%)
1	$18.7 \pm 0.8$	20	6.5
2	$20.3 \pm 0.5$	20	1.5
3	$22.8 \pm 0.6$	20	14
4	$195.6 \pm 5.5$	200	2.2
5	$212.5 \pm 6.7$	200	6.3
6	$227.7 \pm 9.3$	200	14
7	$330.2 \pm 10.4$	300	10
8	$335.3 \pm 5.5$	300	12
9	$315.8 \pm 8.4$	300	5.3

**Figure 2.16. Microscopy View of a PDMS Separation Surface (5 pulses/ $\mu\text{m}$  and 1.0  $\mu\text{J}$ ).**

The SEM images of the ablated network structure are exhibited in Figs. 2.18(a)



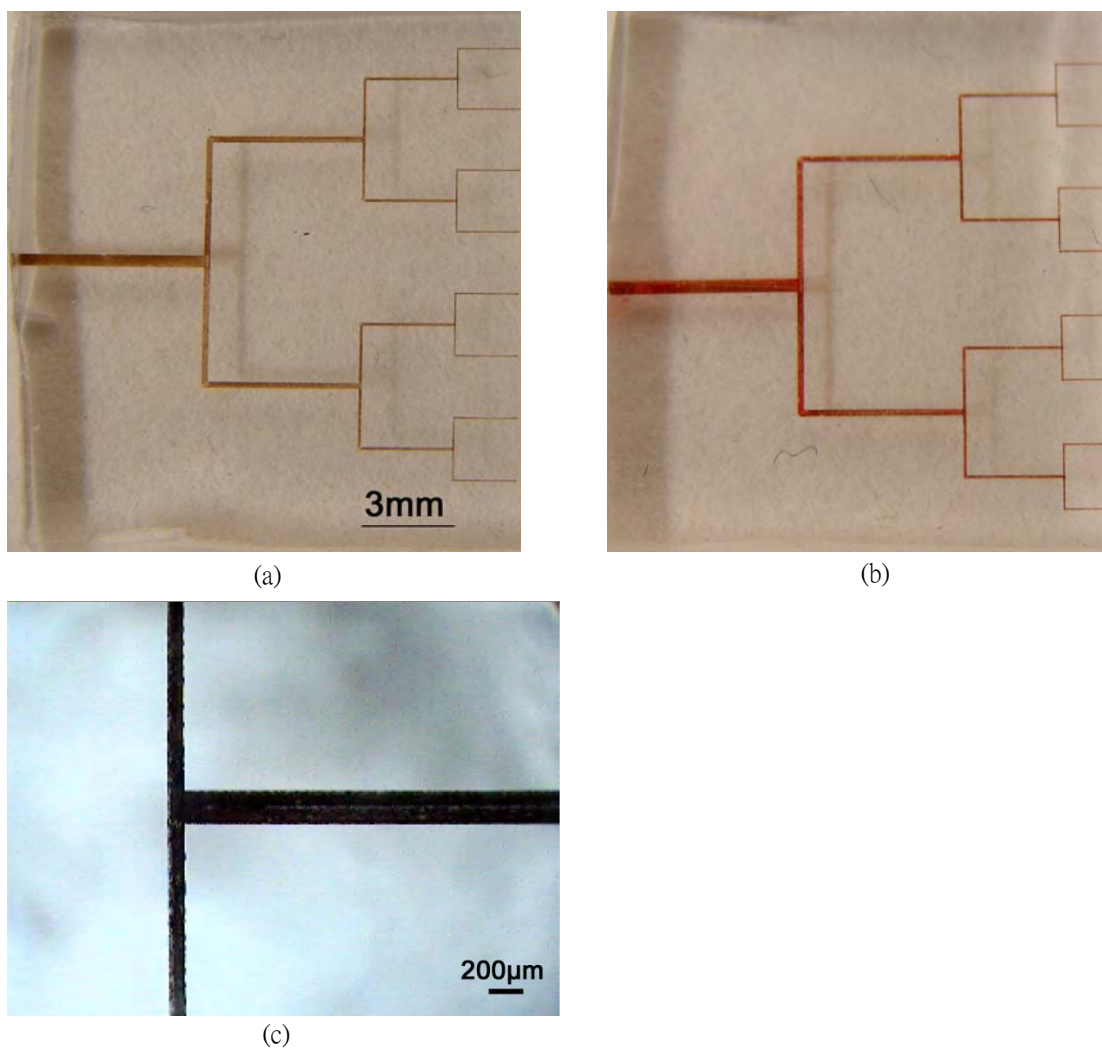


**Figure 2.17. Multi-width Micro-channel Network Fabricated via the USP Laser Direct Writing (2 pulses/μm and 1.0 μJ).**

**(a) Multi-width Micro-channel Network Structure, (b) The Same Structure with Red Dye Flow, and (c) Microscopy View of a Junction of the Micro-channel Network.**

and (b) for an ablated surface in the largest channel and a junction connecting two channels, respectively. From the images the roughness of the ablated surface is estimated as 10 μm. Thus, the internal surface ablation roughness is close to the analytical value of the depth of focus. For taking the SEM image in Fig. 2.18 (b), the network structure was cut into two halves so that the inside of the channel can be visualized with a tilted angle.

It should be mentioned that the channel network results shown in Figs. 2.17 and 2.18 have not been treated with any other method such as etching which can smoothen the ablation surface.

And we have also fabricated a ‘V’ shape channel structure and an ‘R’ shape micro structure inside the PDMS block, as shown in Fig 2.19. Both of the structures were fabricated by one time scan. The dimension of the ‘V’ shape channel is about 10 mm long, 8 mm wide by 4 mm high. The dimension of the ‘R’ shape is about 10 mm high, 4 mm wide and 4 mm thick.

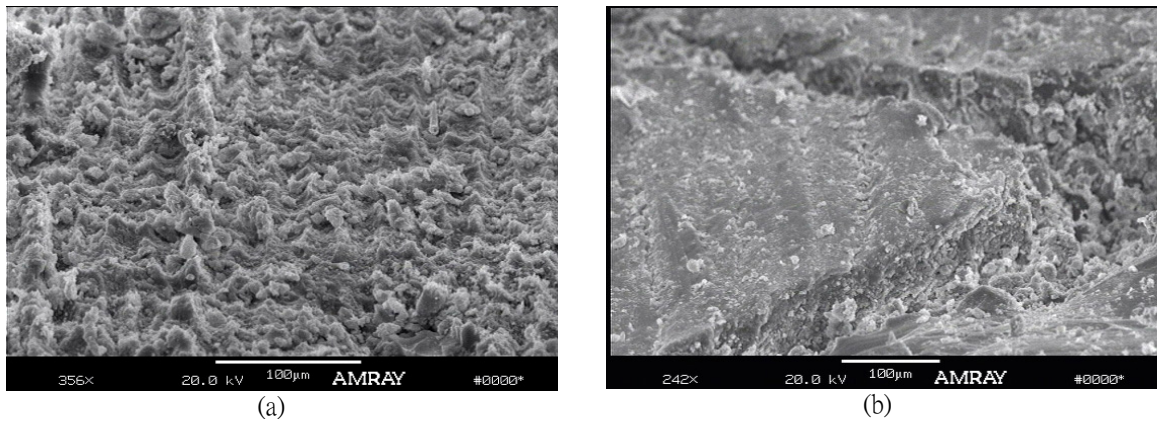


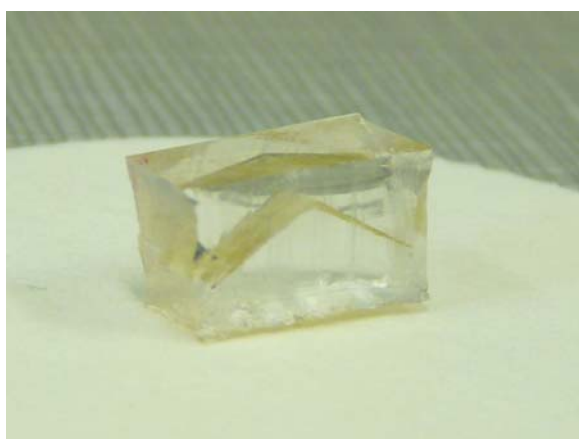
**Figure 2.18. SEM Images of the Multi-width Micro-channel Network Structure.**

**(a) An Ablated Channel Surface, and (b) A Junction with Tilted Angle.**

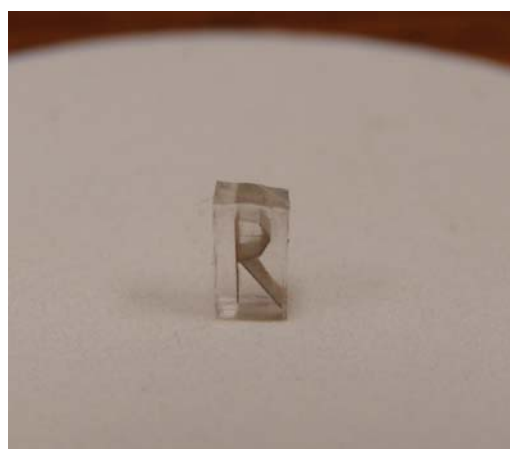
## **2.5. Summary**

The ablation features of single spots and continuous lines on PDMS surface via the USP laser direct writing are investigated. The ablation craters and lines are imaged for different irradiation pulse energies with various pulse numbers or pulse overlap rates.

The single pulse ablation threshold for single spot ablation and single line scanning ablation are determined to be 4.62 and 4.33 J/cm<sup>2</sup>; and the incubation factor for multi-pulse ablation is found as 0.52 and 0.56. The results from both methods are close to each other. The ablation line width increases as pulse energy or overlap rate increases. For PDMS thin-layer separation and micro-fabrication using the present instrument, the pulse overlap rate can be chosen in a wide range between 0.5 pulse/μm and 10 pulses/μm. However, a proper pulse overlap rate should accommodate the irradiation pulse energy. When the irradiation pulse energy is 0.75 μJ, an appropriate pulse overlap rate should be in the range of 5 to 10 pulses/μm; while when the irradiation energy increases to 2.5 μJ, the pulse overlap rate should drop to the range of 0.5 to 1 pulse/μm. Use of lower pulse overlap rate will improve fabrication efficiency and minimize possible thermal damage; but may require higher pulse energy. Overall, 1-2 pulses/μm and 1-1.5 μJ are proper parametric ranges.



(a)



(b)

**Figure 2.19. Micro Structures Fabricated by USP Laser Internal Ablation.**

**(a) A 'V' Shape Channel Inside PDMS Block, and (c) An 'R' Shape Structure.**

Separation of PDMS layers is based on the area scanning with laser ablation inside. The separation of various PDMS thin layers and fabrication of a micro-channel network structure by the USP laser system are presented. The thickness of the separated thin layer is controllable via adjusting the laser focus spot position. For the three tests with a target thickness of 20  $\mu\text{m}$ , the averaged thickness of the separated thin layers is  $20.6 \pm 1.7 \mu\text{m}$ . Both the pulse energy and the overlap rate influence the ablation interface layer depth. The effect of pulse overlap rate is more pronounced when the overlap rate goes above the value 4 pulses/ $\mu\text{m}$ . Below this value, the ablation layer depth is about 20  $\mu\text{m}$  for 1-1.5  $\mu\text{J}$  pulse energy, twice of the depth of focus. The fabricated network is shown to be interconnected. The roughness of the internal ablation surfaces in the network is close to the depth of focus

## **Chapter 3.**

### **Wet Human Dermis Tissue Separation via USP Laser Plasma-mediated Ablation**

#### ***3.1. Introduction***

Skin grafting originated from approximately 2500 to 3000 years ago has evolved over the last century into an option that is routinely and sometimes preferentially used during soft tissue reconstruction. The number of patients recovering from post-burn and post-traumatosis by graft tissue implantation is growing. Nowadays in USA over 900,000 allografts are transplanted each year. Naturally derived materials such as allograft, xenograft, and autograft tissues have many biological, chemical and mechanical advantages over synthetic materials; and thus, hold tremendous potential for use in tissue transplantation and therapies. However, surgical treatment is frequently restricted by the scarcity of adequate tissues available for reconstruction. Separation of a tissue into two or multiple layers leads to augmented usages of the limited tissues, doubling or even tripling the harvest of donor tissues. Moreover, a tissue may have to be separated into layers, as the tissue in its entirety may not be necessary or appropriate for implantation [1]. In the treatment of burn wounds, for instance, in many cases it is necessary only to implant the epidermal layer of a skin allograft [21]. It is also known that in many cases only an acellular dermis is needed for facial soft tissue augmentation [22] or for breast reconstruction [23].

Furthermore, the use of these natural biomaterials typically requires pretreatment such as cutting and shaping the tissue into an appropriate form before transplanted into a patient or subject and there lack effective and efficient methods for micro-processing of tissue without collateral damage. How to utilize a donor or artificial tissue as efficient as possible is still a big challenge, because techniques using a mechanical cutter or surgical knife to separate a tissue into layers or cut the tissue into portions are often imprecise and can result in damage to the underlying layers and/or surrounding tissue. Conventional pulsed laser ablation usually generates thermal damage to the surrounding tissue such as melting or charring. Chemical method is time-consuming and the residues at the tissue sample could be harmful for the safety of further usage. Thus, an effective method that can precisely and non-intrusively modify tissues with minimized damage is desired.

Lasers have become irreplaceable tools of modern medicine, spanning a wide spectrum of applications from laser surgery [39] to optical imaging [102]. Laser ablation that takes great advantages in precise material removal is a promising method in processing and treatment of biological tissues [11-14], biodegradable polymers [15-17], collagen gels [18], dental implants [19], etc. If the rate of plasma formation is relatively slow, in the ns time regime (for ns excitation laser pulses) or longer, energy is transferred from the plasma to the lattice, and thermal damages like melting or charring of the surrounding tissue can occur.

Contrast to thermal ablation, *in vitro* experiments on soft tissue have proved the absence of remarkable thermal damage to the surrounding materials via plasma-mediated

ablation by USP lasers. This important feature makes USP lasers very attractive for micro-processing of various tissues. The use of USP laser for tissue separation and cut provides a new method that can precisely and efficiently modify tissues with minimized damage. Although processing and treatment of biological tissues with USP laser have been investigated by many researches [11-14], the separation and cut of real human tissue has not been accomplished and reported. The objectives of this research project include: 1) Fundamental study for wet dermis tissue ablation threshold with USP laser; 2) Thermal damage investigation of USP laser wet dermis tissue ablation; 3) Wet dermis separation and micro-processing with minimized thermal damage demonstration via USP laser ablation.

## ***3.2. Materials and Methods***

### **3.2.1. Experimental Set up**

The experimental setup for USP laser tissue ablation is composed of the same four main parts as described in Chapter 2: a USP laser, a beam delivery system, a work stage and a whole control system. The commercial Erbium doped fiber laser (Raydiance, Inc.) has the same parameters as in the PDMS micro-fabrication described in Chapter 2. In the beam delivery system, the laser beam was focused to the target through the same objective lens as shown in Fig. 3.1. The diffraction-limit focal spot diameter ( $2.44\lambda f_L / D$ ) in free space is estimated as 8  $\mu\text{m}$ . The laser power loss in the beam delivery system was measured to be 50% by the digital power meter.

The work stage for mounting tissue samples was fixed to the 3-D automated translation stage through which the alignment of optics and laser scanning were realized. There are two designs for the work stage in this study. Figure 3.1(a) shows the schematic diagram of experimental setup I with a plate fixture for sample mounting. This setup is simple and was used for characterizing the single line scanning ablation features.

However, it was time consuming to separate dermis. A wet tissue mounting on the simple plate fixture was apt to dehydrate and deform because of the stage movement. In order to avoid the deformation, a moisture chamber that keeps the tissue wet during the laser processing was utilized as sketched in Fig. 3.1(b). A tissue feeding and pulling scheme was also designed in experimental setup II as shown in Fig. 3.1(b) such that the separation interface was always exposed to the laser focal spot through the pulling of two opposite tension forces. Therefore, one does not have to focus the beam into deep tissue and the strong attenuation of biological tissues against light was not a concern. With laser ablation at the exposed interface, the two opposite tension forces pull and split the dermis into two separate layers. An evacuator system (FX225, EDSYN) which is not shown in Fig. 3.1 was also employed to collect plasma plume residue and debris during the laser processing.



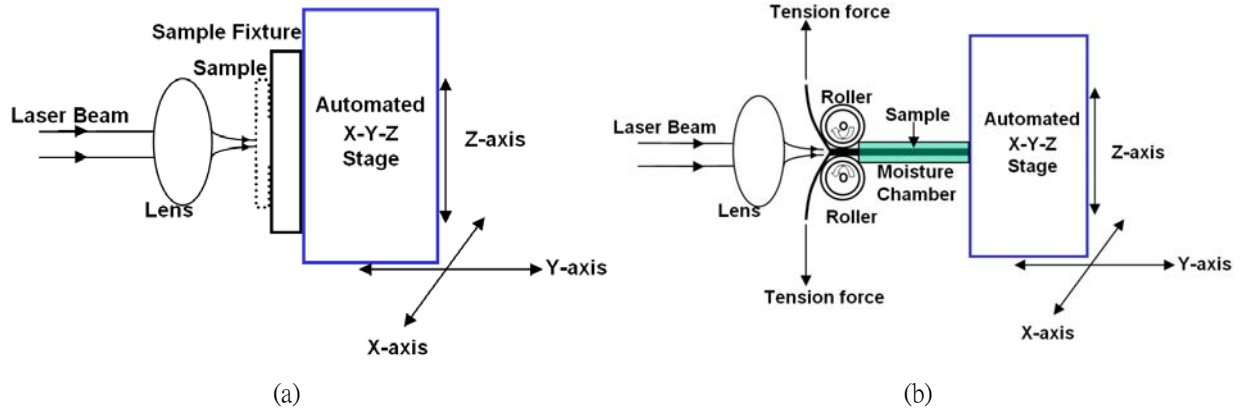


**Figure 3.1. Sketch of the Experimental Setup.**

**(a) Experimental Setup I for Single Line Ablation, and (b) Experimental Setup II for Multi-line Ablation and Separation.**

### 3.2.2. Tissue Sample Preparation

In this study, we used human dermal tissue samples, which were obtained post-mortem from donated human allograft skin and were provided with package hydrated after processing by professionals from the project sponsor - MTF. The donor skin tissue was processed with a series of soak processing - sodium chloride, triton and finally disinfection soak. After processing, the epidermal and dermal cells were removed and the remaining components and extracellular matrix of the dermis were preserved. The dermal tissue samples are about 2 mm thick and precut from the original whole piece tissue samples. Figure 3.2 shows a precut wet dermal tissue sample with about 20 mm by 20 mm dimension and 2 mm thickness.

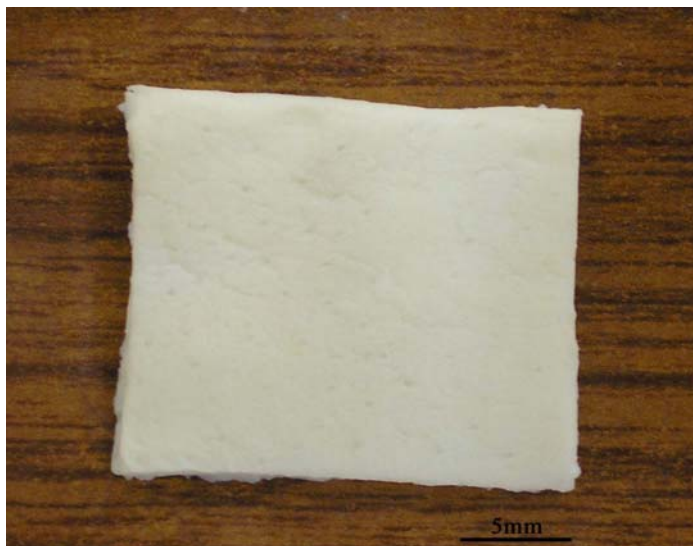


**Figure 3.2. Photo of One Wet Dermis Sample before Experiment.**

### **3.2.3. Measurements**

Immediately following the ablation experiment, the micro topography and surface quality of the ablated tissue sample were examined by an upright digital microscope (National Optical DC3-156-S). Then the treated samples were fixed in 2% phosphate buffered Glutaraldehyde for 2 hrs, rinsed twice in Phosphate Buffer and dehydrated in ethanol. After critical point drying and metal coating, the tissue samples were checked by SEM (AMRAY 1830I). For the histological evaluation, the samples were routinely dehydrated in a series of graded ethanol. Then the samples were fixed in paraffin wax and sectioned into 10  $\mu\text{m}$ -thick slices. After that, the slices were stained with Hemaoxylin and Eosin (H&E). Finally the samples were viewed and photographed by a Nikon Eclipse E600 microscope system. The thickness of the separated samples was measured by a vernier caliper.

### **3.3. Results and Discussion**

#### **3.3.1. Fundamental Study of Single Line Surface Ablation**

First of all, the ablation threshold of the wet tissue samples via the current experimental setup should be determined. We have tried the single spot ablation on the wet tissue surface to obtain the ablation craters on the tissue sample surface. But two major problems were encountered in this process: firstly, the ablation crater on the wet tissue surface is very hard to check and measure because the tissue sample is easy to get dried and it is not transparent compared with PDMS; Secondly, the pulse energy of the current laser system is not high enough to generate single ablation crater on the sample surface and this is because the ablation threshold of tissue sample is higher than PDMS. Therefore single line surface scanning ablation was used for the fundamental study of the wet tissue ablation.

To enable practical tissue separation, ablation features of the single line surface scanning has been studied to obtain the ablation threshold. The main parameters that affect the ablation include irradiation pulse energy and the pulse overlap rate which is equal to  $f/s$ . The irradiation pulse energy,  $E$  that is 50% of the laser output energy, determines whether the incident laser fluence is above the critical value that plasma-mediated ablation occurs. The pulse overlap rate determines the pulse overlap intensity.

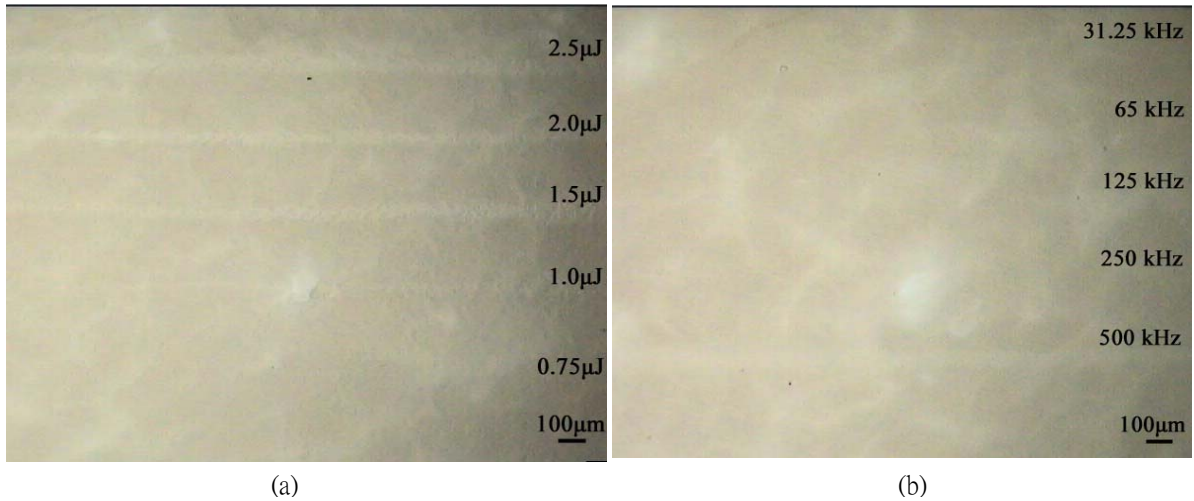


**Figure 3.3. Microscope View of Wet Dermis Single Line Surface Ablation with Different Laser Parameters.**

**(a) With Different Pulse Energies, and (b) With Different Pulse Overlap Rates.**

Multiple wet dermis samples have been chosen to investigate the single line scanning ablation features on sample surface with different laser parameters. After irradiation, a digital microscopy was used to inspect the ablated features of the tissue sample and the measurements of ablation line features are conducted by SEM. Figure 3.3(a) shows the microscopic view (40X magnification) of several laser scanned lines on the wet dermis with different irradiation pulse energies (0.75  $\mu\text{J}$  - 2.5  $\mu\text{J}$ ). The pulse repetition rate was 500 kHz and the moving speed of stage was 25 mm/s. Thus, the pulse overlap rate was 20 pulses/ $\mu\text{m}$ . Figure 3.3(b) shows the microscopic view (40X magnification) of laser scanned lines with different pulse overlap rates with the same pulse energy (2.5  $\mu\text{J}$ ), and the stage moving speed was 25 mm/s and thus the pulse overlap rate changes from 1.25 - 20 pulses/ $\mu\text{m}$ . From Fig. 3.3, we can see that it is difficult to observe a clear ablation line at the wet dermis although ablation sparks were observed during the laser processing. This is quite different from the previous PDMS polymer ablation study in Chapter 2 [17] in which clear ablation lines were observable in

a single line scanning ablation. Thus, the ablation at wet dermis is very superficial. However, the generated imprints at the wet dermis are clearly shown in Fig. 3.3. It is worth mentioning that the imprint lines have a width about 30 - 40  $\mu\text{m}$ . This width can be further reduced using a high numerical aperture lens.

Further inspection and measurements from SEM show that the microscopy view of the wet soft tissue ablation can not provide accurate measurement results for ablation features because of the tissue deformation and the water evaporation in the processes. To obtain accurate measurement of ablation features, such as ablation line width or depth, SEM image view could be a proper way to check and measure the features.

Figure 3.4 shows four representative SEM images for the four ablation lines generated with varying irradiation pulse energy 1.0 - 2.5  $\mu\text{J}$ , respectively. The pulse repetition rate was 500 kHz and the moving speed of the stage was 25 mm/s. Thus, the pulse overlap rate was 20 pulses/ $\mu\text{m}$ . From the SEM top view images such as Figs. 3.4(a) and 3.4(b), one can measure the average ablation line width as  $18.5 \pm 1.3 \mu\text{m}$  and  $15.6 \pm 0.7 \mu\text{m}$  (based on three different ablated samples) for the cases of 2.5 and 2.0  $\mu\text{J}$  irradiation pulse energies, respectively. While the cut width using mechanical tools such as general surgical blade or scalpel is in the range from 100  $\mu\text{m}$  to 1 mm [1]; so the USP laser ablation is more precise and results in less waste. Figures 3.4 (c) and (d) are representative views with a tilt angle for the ablation lines of 1.5 and 1.0  $\mu\text{J}$  irradiation pulse energies, respectively. It is seen that the dermis surface is not very flat and has a roughness about 5  $\mu\text{m}$ . This roughness will certainly enhance light scattering on the

surface and affect the effective size of the beam focal spot at dermis surface.

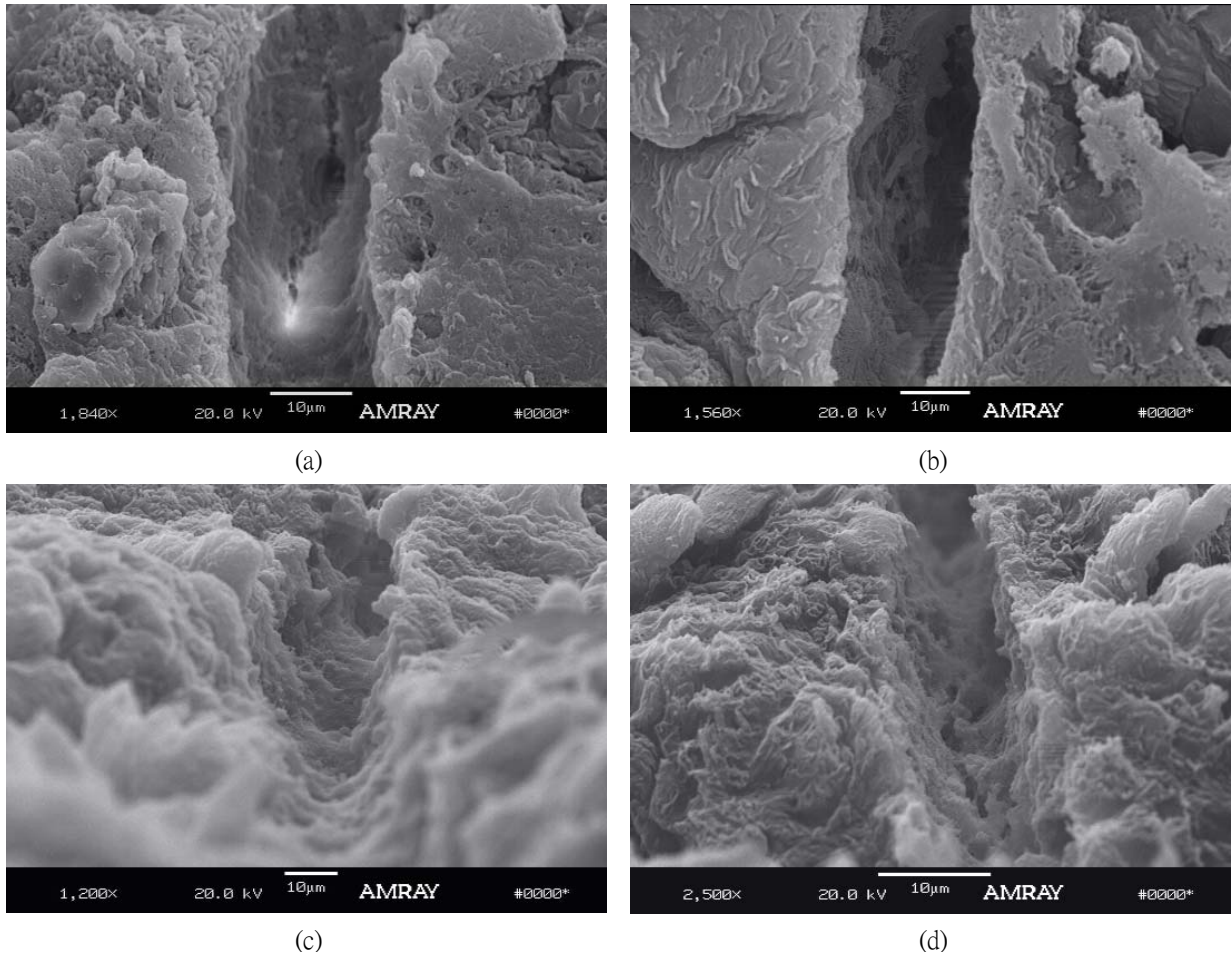


**Figure 3.4. SEM Images of the Single Line Ablations with a Fixed Pulse Overlap Rate 20 pulses/ $\mu\text{m}$  and Different Irradiation Energies.**

**(a) 2.5  $\mu\text{J}$ ; (b) 2.0  $\mu\text{J}$ ; (c) 1.5  $\mu\text{J}$ ; and (d) 1.0  $\mu\text{J}$ .**

An ablation line consists of continuously ablated craters along the laser scanning direction. When the pulse overlap rate is so intense that no individual crater can be distinguished (such as displayed in Fig. 3.3), the ablation line width is then equivalent to the diameter of the ablated crater generated by  $N$  repeated pulses. The equivalent pulse number can be approximated by Eq. (2.4) in Chapter 2. In laser ablation, the effective

focal spot radius  $r_{\text{eff}}$  and the ablation threshold  $F_{th}$  can be found by the slope and interception with the abscissa the Eq. (2.2) using the same method in Chapter 2.

Figure 3.5 plots the relationship - the square of the ablation line width versus the logarithm of irradiation pulse energy for three different pulse overlap rates. As pointed out by Bonse *et al.* [103], the data at high fluence points should be excluded from linear fitting because the deviation of the intensity from the Gaussian distribution at the “edge” of high fluence beam will lead to nonlinearity. It should be mentioned that the accumulated fluence for the present ablation lines is very high because the equivalent pulse number  $N$  is very large as calculated in Table 3.1. Thus, only low fluence points are adopted for the linear fitting to obtain the slopes of the three curves in Fig. 3.5, in particular for the curve with 20 pulses/ $\mu\text{m}$  pulse overlap rate. The calculated effective radii for the focal spots with different pulse overlap rates and the corresponding equivalent pulse number are listed in Table 3.1. It is seen that the effective spot size (9 - 17  $\mu\text{m}$ ) is bigger than the diffraction-limit spot size (8  $\mu\text{m}$ ) in free space. This is consistent with the results of Mullan *et al.* [21] and Choi *et al.* [22] for polymers and can be attributed to the strong scattering of light on the rough dermis surface. When the pulse overlap rate is just 5 pulses/ $\mu\text{m}$ , it is seen that the calculated effective radius is close to the diffraction-limit prediction. With increasing pulse overlap rate, the accumulated fluence increases and the deviation between the calculated effective radius and the diffraction-limit prediction widens.

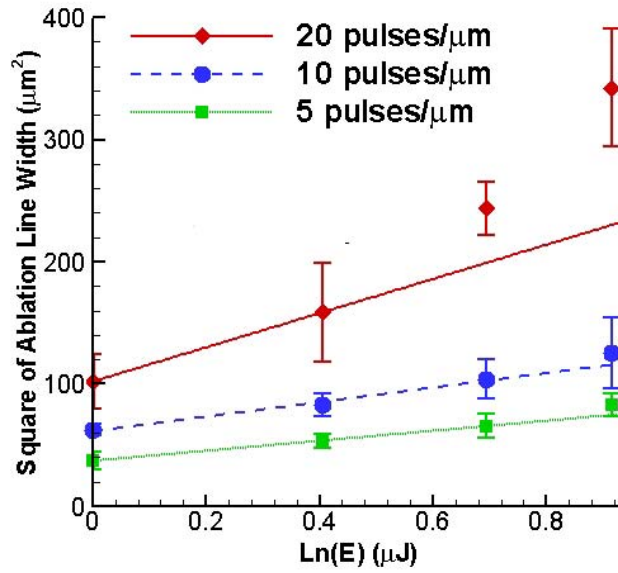


Figure 3.5. Square of Ablation Line Width versus Irradiation Pulse Energy for the Evaluation of Effective Focal Spot Size.

Table 3.1. Effective Focal Spot Radii and Ablation Thresholds for Different Pulse Overlap Rates.

Pulse Overlap Rate (pulses/ $\mu m$ )	5	10	20
Equivalent Pulse Number	45	110	336
Effective Focal Spot Radius ( $\mu m$ )	4.5	5.5	8.4
Ablation Threshold $F_{th}$ ( $J/cm^2$ )	1.27	0.75	0.43

Table 3.1 also lists the ablation thresholds for the three different pulse overlap rates. Clearly the ablation threshold decreases as the pulse overlap rate increases because of the incubation effect. Using the data in Table 3.1, a least-squares fitting line of  $\ln(NF_{th}(N))$  versus  $\ln(N)$  can be drawn (not presented here) and the slope yields an incubation factor  $\xi = 0.46 \pm 0.03$ , as shown in Fig. 3.6. Therefore, the ablation threshold



for the wet human dermis is determined as  $F_{th}(1) = 9.65 \pm 1.21 \text{ J/cm}^2$ .

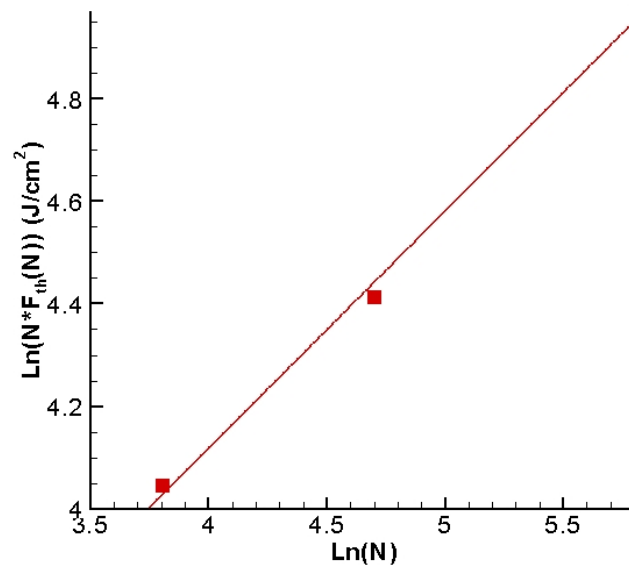


Figure 3.6. Incubation Effect on Wet Dermis Single Line Ablation with Different Pulse Overlap Rate.

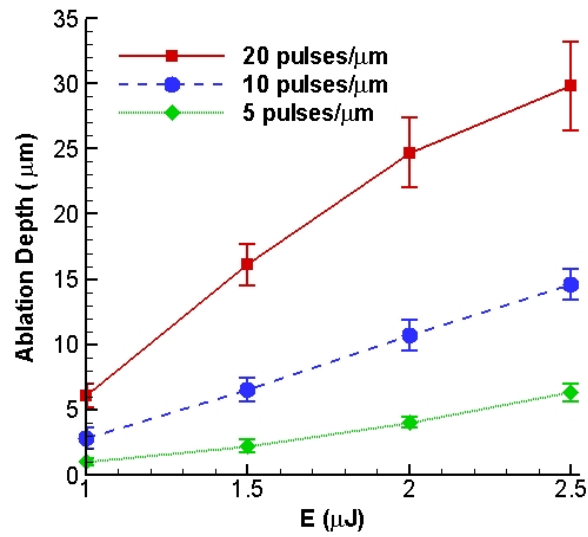


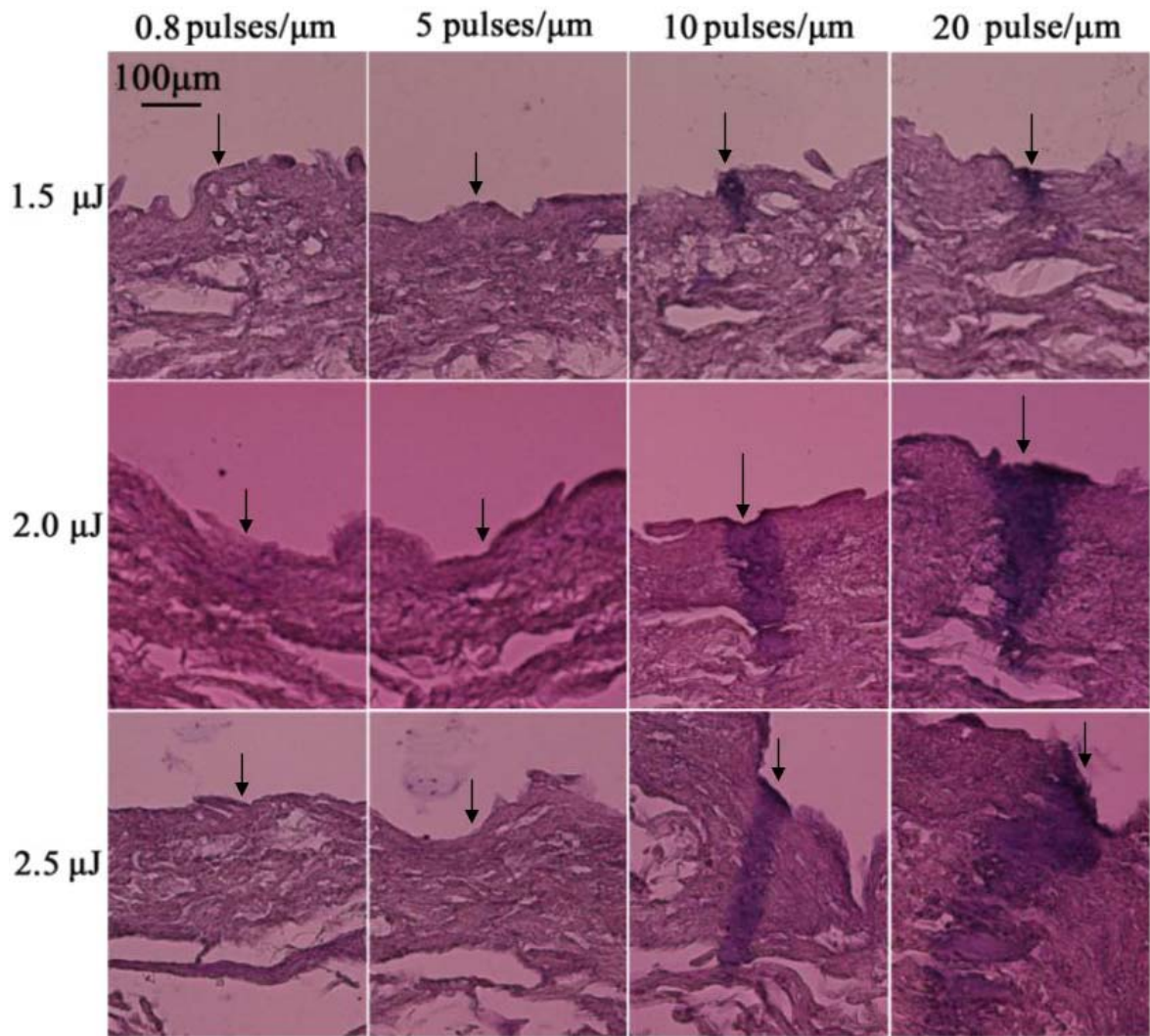
Figure 3.7. Single Line Ablation Depths as a Function of Irradiation Pulse Energy.

Figure 3.7 shows the ablation depth changing with the irradiation pulse energy for different pulse overlap rates in the situation of single line scanning ablation. For each ablation depth datum, three samples were measured to obtain the average value and the uncertainty. It should be noticed that in the preparation of fixing and drying for the SEM examination, the samples may be somewhat distorted and the distortion affects the measurement accuracy as well. From Fig. 3.7 it is seen that the ablation depth increases with both the irradiation pulse energy and overlap rate. It is known that the pulse overlap rate increases with the pulse repetition rate but decreases with the scanning speed, and the ablation progress is linearly proportional to the scanning speed. For a fixed scanning speed, the ablation production efficiency increases with increasing pulse energy and repetition rate.

### **3.3.2. Thermal Damage Investigation**

In order to examine the degree of thermal damage, the histology of some line scanning ablated samples was analyzed. Figure 3.8 shows the sectional view (200X magnification) of 12 H&E stained wet dermis samples ablated with single line surface scanning with different laser parameters. The selected pulse energies are 1.5, 2.0 and 2.5  $\mu\text{J}$ , respectively. The pulse overlap rates are 0.8, 5, 10 and 20 pulses/ $\mu\text{m}$ , respectively. The irradiation surface in the pictures faces up and the beam spot is around the middle in each picture. Thermal damaged zone is visualized by the dark shadow area, because the elastic fibers in the damaged zone are no longer apparent, having been converted into an amorphous, coagulated mass. As observed from Fig. 3.8, no thermal damage or structure change occurs in the dermis when the pulse overlap rate is 5 pulses/ $\mu\text{m}$  and below, even

in the case of high irradiation pulse energy (2.5  $\mu\text{J}$ ). When the pulse overlap rate is 10 pulses/ $\mu\text{m}$  and above, however, a clear thermal damage zone is observed, in particular when the pulse energy is 2.0  $\mu\text{J}$  and above. The higher the pulse overlap rate or the higher the pulse energy, the larger and the severer (darker) is the thermal damaged zone. Hence, the accumulation of irradiation fluence is the key factor for causing thermal damage. In order to minimize or eliminate thermal damage, operation with a lower pulse overlap rate is essential. For the cases studied here, a pulse overlap rate up to 5 pulses/ $\mu\text{m}$  is safe for single line ablation.



**Figure 3.8. Histological Views of Single Line Ablation at Wet Tissue.**

The study by Suhm *et al.* [104] also showed no thermal damage signs in picosecond laser ablation of neural tissue. Kautek *et al.* [105] reported a damage zone less than 0.5 μm in the ablation of human corneas using a femtosecond pulsed laser. Girard *et al.* [90] claimed approximately 14 μm damage zone in the ablation of osseous tissues using a femtosecond Ti:Sapphire laser. When long pulsed lasers are utilized, thermal damage zone is more profound. For example, Walsh *et al.* [27] found that the damage zone jumped from 50 to 750 μm when the pulse duration increased from 2 μs to

50 ms using CO<sub>2</sub> lasers.

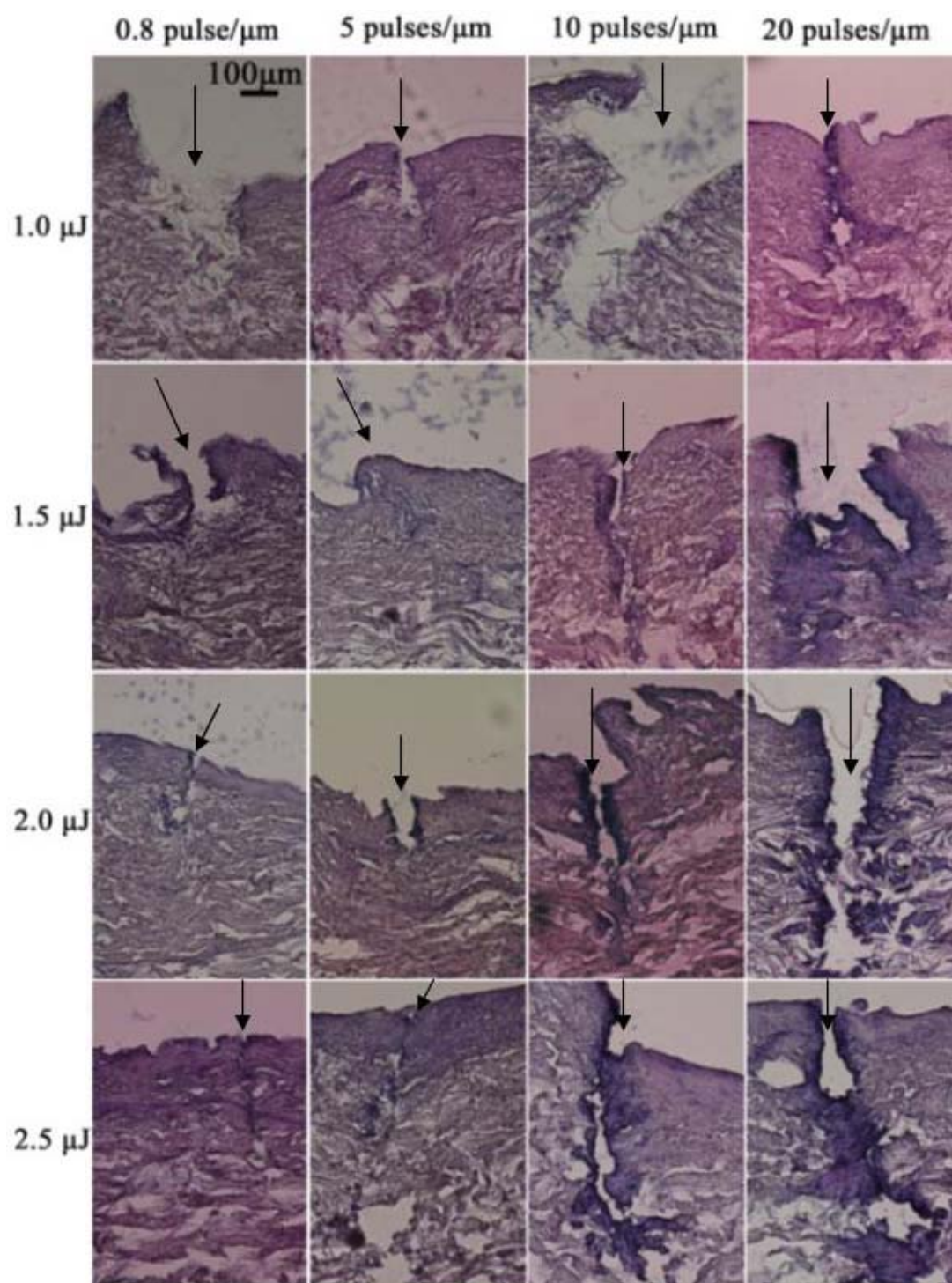


Figure 3.9. Histological Views of Multi-line Ablation at Wet Tissue.

From Fig. 3.7, it is obvious that ablation scanning of multiple lines is required in order to achieve practical tissue separation or cutting. Some representative histological results of multi-line ablation are available in Fig. 3.9 for evaluation and comparison, where the sectional views (200X magnification) of 16 ablation processed tissue samples with different laser parameters are illuminated. Each tissue sample was repeatedly line scanned for 100 times using experimental setup II. During the processing, the ablation interface was always renewed via the tension through the two opposite tension forces. The selected pulse energies are 1.0, 1.5, 2.0 and 2.5  $\mu\text{J}$ , respectively. The pulse overlap rates are 0.8, 5, 10 and 20 pulses/ $\mu\text{m}$ , respectively. The irradiation surface in each picture faces up and the beam focal spot is around the middle. Now clear cuts to a certain depth in all the samples are observed. Comparing Figs. 3.8 and 3.9, the underlying thermal damages in the cases of multi-line ablation are smaller than those in the cases of single line ablation, because the accumulation of the multi-line energy will take away the material in the underlining thermal damage zone. In practical tissue separation or cutting, the underlying damage is not a concern because the tissue has to be cut through.

**Table 3.2. Lateral Thermal Damage Zones Results from 100-line Ablation.**

$\begin{matrix} f/s \\ E \end{matrix}$	20 pulses/ $\mu\text{m}$	10 pulses/ $\mu\text{m}$	5 pulses/ $\mu\text{m}$	0.8 pulse/ $\mu\text{m}$
2.5 $\mu\text{J}$	$67 \pm 10 \mu\text{m}$	$40 \pm 8 \mu\text{m}$	$8 \pm 3 \mu\text{m}$	$6 \pm 4 \mu\text{m}$
2.0 $\mu\text{J}$	$54 \pm 10 \mu\text{m}$	$38 \pm 8 \mu\text{m}$	$6 \pm 4 \mu\text{m}$	$4 \pm 4 \mu\text{m}$
1.5 $\mu\text{J}$	$52 \pm 8 \mu\text{m}$	$18 \pm 5 \mu\text{m}$	$3 \pm 2 \mu\text{m}$	$3 \pm 3 \mu\text{m}$
1.0 $\mu\text{J}$	$26 \pm 6 \mu\text{m}$	$3 \pm 2 \mu\text{m}$	$2 \pm 2 \mu\text{m}$	$2 \pm 2 \mu\text{m}$

Table 3.2 summarizes the sizes of the lateral thermal damage zone around the cut edge for the laser parameter sets considered in Fig. 3.9. The thermal damage behavior for the multi-line scanning cases is very similar to that observed in the single line scanning results, even though the accumulated fluence in multi-line scanning is 100 times stronger than the single line scanning. The reason is that between two successive scans, the lateral accumulation of thermal energy is trivial because the energy has been dissipated into the surroundings. It should be noticed that in the cases of 100-line ablation with pulse overlap rate 5 pulses/ $\mu\text{m}$ , however, lateral thermal damage is observable within a 10  $\mu\text{m}$  zone when the irradiation pulse energy is 2.0  $\mu\text{J}$  or above, and the damage is reduced to 2-3  $\mu\text{m}$  when the irradiation pulse energy is below 2.0  $\mu\text{J}$ . This is because the accumulated energy between two successive scans has not been fully dissipated yet. This problem may be resolved by delaying the repeated scanning time.

Apart from the qualitative examination, Fig. 3.9 also shows the cut (ablation) depths for different pulse overlap rates and pulse energies. It is seen that the ablation depth generally increases as the pulse energy and/or overlap rate increase. In the current experiments, two spring steel clips (SBC-78210) were used as the tension forces and the forces were not optimized in line with the single line ablation depth. Thus, the cutting depth due to multi-line ablation is not a simple multiplication of corresponding single line ablation depth. For example, the 100-line ablation depth for the picture in Fig. 3.9 with pulse overlap rate 5 pulses/ $\mu\text{m}$  and irradiation pulse energy 2.0  $\mu\text{J}$  is only 210  $\mu\text{m}$  although its single line ablation depth from Fig. 3.7 reaches to 4.0  $\mu\text{m}$ . Other reasons that could degrade the multi-line ablation depth include beam block by the edges of the prior

ablation grooves or by the generated residues and debris and beam alignment. It should also be mentioned that in the preparation of samples for the histological view, the samples might be somewhat distorted and this may affect the measurement accuracy as well

Since the cutting efficiency is directly proportional to the ablation depth and scanning speed, it is desirable to operate the laser tissue processing system at high irradiation pulse energy, high pulse repetition rate and high speed of scanning. In the same time, the pulse overlap rate must be controlled to avoid thermal damage. In summary, an optimal set of operation parameters for wet dermis cutting and separation is recommended as follows: irradiation pulse energy = 1.5  $\mu\text{J}$ , stage moving speed = 25 mm/s (the maximum of the current instrument), pulse repetition rate = 125 kHz, and pulse overlap rate = 5 pulses/ $\mu\text{m}$ .

### **3.3.3. Wet Dermis Separation by USP Laser Ablation**

We have tried two different set ups to demonstrate the wet dermis tissue separation via USP laser ablation. The first set up is shown in Fig. 3.1(b) and this set up is the finally-adopted set up for the separation. Another set up we tried is shown in Fig. 3.10, which is simple and easy to keep the tissue wet during the processing, but experiments show that it is very difficult to achieve the goal via this set up and we will discuss this set up first and explain why this set up is difficult.

The wet tissue sample was sandwiched by a bottom sapphire window and a glass



slides on top in the chamber and was kept flat by adding a proper weight (such as a steel gasket in Fig. 3.10(b)) on the top glass slide. The sample chamber was kept wet by adding a few drops of water. The laser beam passes through the bottom sapphire window with negligible power loss and is focused into a certain depth inside the wet tissue to ablate the wet tissue inside. To ensure that the focal plane was inside the tissue sample, the focal spot was firstly adjusted to the top surface of the bottom glass slide through the observation of the third harmonic generation of green spark; and keep focal spot moving towards the sample until the green spark almost vanished, then the desired depth was adjusted through the Z-axis motion inside the sample. Then we used repeat area scanning method to try to separate the tissue into layers like the PDMS thin layer separation in Chapter 2.

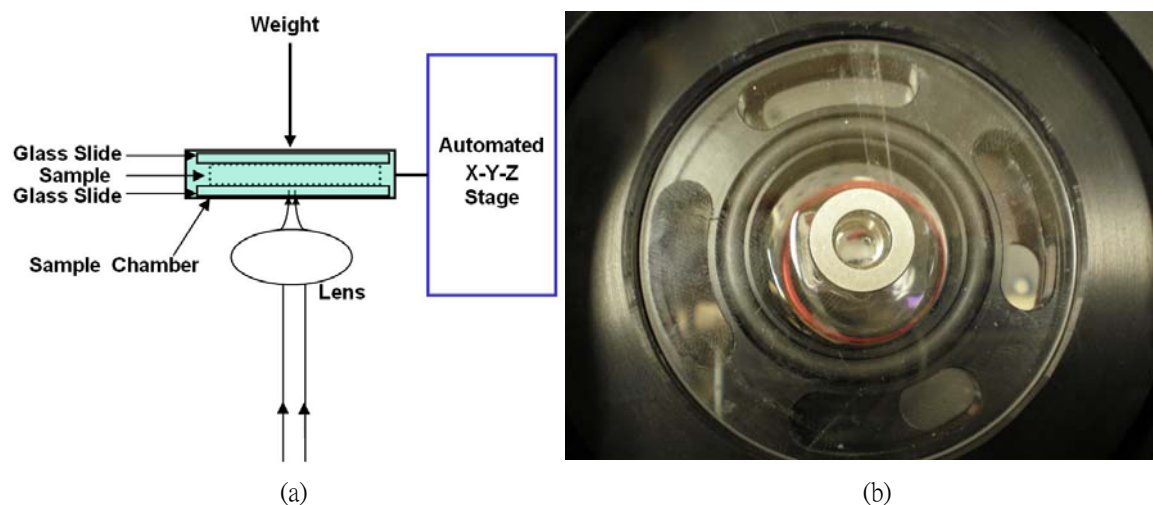


**Figure 3.10. Alternative Set up of Wet Dermis Separation.**

**(a) Experimental Setup Sketch, and (b) Top View of the Sample Chamber.**

Figure 3.11 shows the picture of the ablation spark during the area scanning processing. The laser beam was focused about 100  $\mu\text{m}$  deep into the tissue and the laser

parameters used are 2.5  $\mu\text{J}$  pulse energy and 25 pulses/ $\mu\text{m}$  overlap rate. We can see from Fig. 3.11 that the color of the spark is mainly white surrounded by third harmonic green light.

Figure 3.12 shows the microscopic view of the separation result on the bottom window after two times repeat area scanning over the entire wet dermis with 2.5  $\mu\text{J}$  pulse energy and 1 pulses/ $\mu\text{m}$ . The sample dimension is about 7 mm long and 2.5 mm wide. The laser beam was focused 20  $\mu\text{m}$  inside the tissue for the area scanning. We can see from Fig. 3.12, there are fragmentary separated wet dermis layers on the sapphire window after the repeat area scanning and the whole piece of separated wet dermis layer can not be obtained. Figure 3.13 shows the microscopic view of another separation results with 100  $\mu\text{m}$  focal spot inside the sample and five time repeated area scan with 2.5  $\mu\text{J}$  pulse energy and 20 pulses/ $\mu\text{m}$ . Although more repeated scan and higher pulse overlap rate can improve the separation results, the results of separation are not acceptable and a whole piece of separation could not be achieved. The main reason why this set up is not successful is the strong attenuation of the laser energy inside the tissue because of absorption and scattering. The energy attenuation measured when the laser beam passes through a piece of wet dermis sample with 100  $\mu\text{m}$  average thickness is around 82%. We can see that most of the laser beam energy has been attenuated when focused inside the tissue and the plasma-mediated ablation can not be generated continuously.

So an alternative method for separation together was used, in which a tissue feeding and pulling scheme was designed as shown in Fig. 3.1(b) in experimental setup II

such that the separation interface was always exposed to the laser focal spot through the pulling of two opposite tension forces. Therefore, one does not have to focus the beam into deep tissue and the strong attenuation of biological tissues against light was not a concern. With laser ablation at the exposed interface, the two opposite tension forces pull and split the dermis into two separate layers. In order to avoid the deformation, a moisture chamber that keeps the tissue wet during the laser processing was utilized.

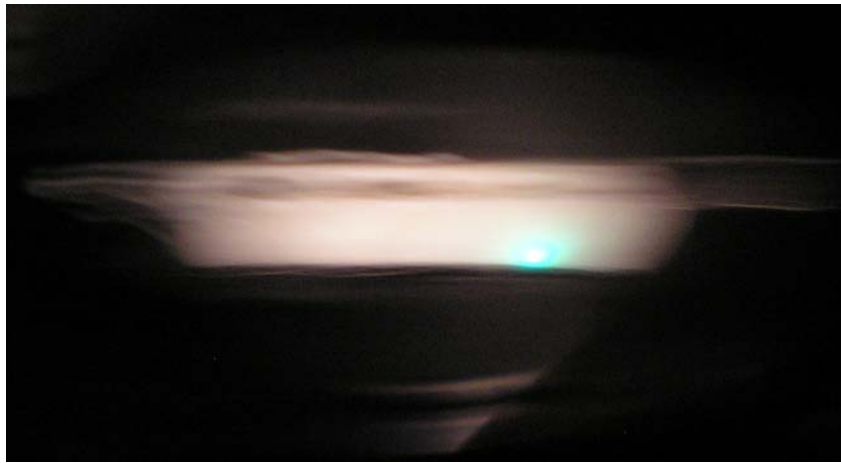


**Figure 3.11. Ablation Spark from Wet Dermis Separation with 100  $\mu\text{m}$  Deep into Dermis and 250 kHz Repetition Rate.**



**Figure 3.12. Microscope View of Separated Wet Dermis Layer on Sapphire Window after 2 times Repeat with 20  $\mu\text{m}$  Increase (40X).**



**Figure 3.13. Microscope View of Wet Dermis Residue on Sapphire Window (20 pulses/ $\mu\text{m}$  & 2.5  $\mu\text{J}$ , 40X)**

The USP laser thin layer separation of wet dermis is demonstrated in Figs. 3.14 and 3.15. Figure 3.14 (a) shows one original wet dermis sample before laser ablation. The sample was 30 mm long, 8 mm wide and 1.4 mm thick. Then the tissue was processed with experimental setup II with pulse overlap rate 5 pulses/ $\mu\text{m}$  and pulse energy 1.5  $\mu\text{J}$ .

Figure 3.14(b) shows the two separated layers that are about 500  $\mu\text{m}$  and 800  $\mu\text{m}$  thick with about 10% unevenness, respectively for the upper and lower pieces. Both layers are slightly deformed because of two reasons: tension forces applied to the tissue during the feeding and pulling process and dehydration of the separated layers due to long-time back and forth motion with the work stage. The separation procedure took about 4 hr in the current instrument.

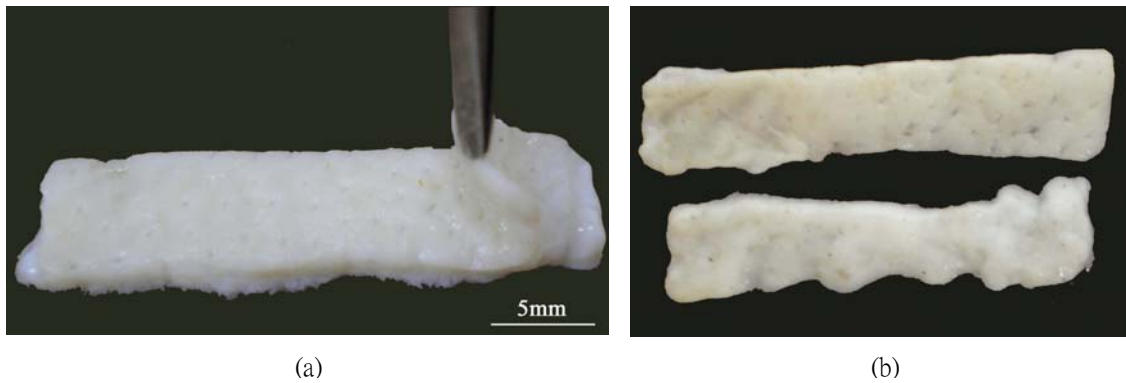


**Figure 3.14. Wet Tissue Separation by the USP Laser Ablation.**

**(a) The Dermis before Laser Ablation, and (b) The Two Separated Thin Layers.**



**Figure 3.15. An Image of a Partially Separated Dermis.**

The separated dermis layers can be further split. Figure 3.15 shows the partially separated result of another dermis layer of 20 mm long, 6 mm wide and 560  $\mu\text{m}$  thick

with the same laser parameters. The thickness of the further separated dermis thin layer is about 220  $\mu\text{m}$  with about 20  $\mu\text{m}$  unevenness. Inspection of the separated layers in Figs. 3.14 and 3.15, no severe thermal damage like charring or melting was found. However, the color in part of the separation surface turned into light yellow. Minor lateral thermal damage to the level of about 0.01 mm might have happened in the light yellow region. One big issue is that the current tissue feeding and pulling system is not very precise and optimal. For example, adjustments to keep the tissue moving and addition of water to the moisture chamber were needed during the processing, which may cause unexpected irradiation of the separated edge area. Further improvement of the experimental setup to eliminate the thermal damage and distortion to the separated dermis layer is the future direction. Table 3.3 lists several dermis tissue separation results via the current instrument and methodology. The separated layers have a uniform thickness with less than 10% uncertainty.

**Table 3.3. Results from Several Dermis Separation Tests.**

Sample No.	Thickness of the Original Dermis (mm)	Thickness of the Separated Thinner Layer (mm)
1	0.56	$0.22 \pm 0.02$
2	0.60	$0.23 \pm 0.02$
3	0.80	$0.32 \pm 0.02$
4	0.80	$0.33 \pm 0.02$
5	1.40	$0.50 \pm 0.03$
6	2.00	$0.56 \pm 0.03$

### 3.4. Summary

In this chapter, *In vitro* human dermis separation into thin layers for enhanced usage has been studied via the USP laser ablation for the first time. Several dermis samples are separated into thin layers with thickness ranging from 200 to 600  $\mu\text{m}$ . The unevenness of the separated layers is under 10%. The plasma-mediated ablation mechanism is found to cause less thermal damage to the ablation lines and separation interfaces. The histological evaluations reveal that there is no thermal damage in the single line ablation results when the pulse overlap rate is 5 pulses/ $\mu\text{m}$  and below. In the 100-line repeated ablations, the lateral thermal damage zone is insignificant and generally within 5  $\mu\text{m}$ . In the layer separation with millions of line ablation, the thermal damage is also confined in a small zone of 10  $\mu\text{m}$ . There is no severe thermal damage like charring or melting existed in the multi-line ablation and layer separation results. The slight thermal damage is caused by the current crude device for tissue feeding and pulling during the laser processing. Design and fabrication of a precise work stage is required in future studies.

The fundamental ablation features of wet dermis are investigated. The ablation threshold for the dermal tissue is found to be  $9.65 \pm 1.21 \text{ J/cm}^2$ . The accumulation effect is very obvious in dermis ablation and its incubation factor is found to be 0.46. The rough surface of the dermis leads to strong scattering of light at the surface. When the pulse overlap rate is 5 pulses/ $\mu\text{m}$ , the calculated effective spot radius is about 15% larger than the diffraction-limit prediction. With further increasing of the pulse overlap rate, the accumulated fluence increases and the deviation between the calculated effective radius

and the diffraction-limit prediction widens. The ablation width and depth increase as the pulse energy and/or overlap rate increase. In terms of cutting efficiency, it is desirable to operate the laser tissue processing system at high irradiation pulse energy, high pulse repetition rate and high speed of scanning. In the same time, the pulse overlap rate must be controlled to avoid thermal damage. There exists a trade-off of balance between the productivity and the minimization of thermal damage.



## **Chapter 4.**

# **Freeze-dried Dermis Tissue Cut and Stripping via USP Laser Ablation**

### ***4.1. Introduction***

In Chapter 3, we have investigated the ablation and separation of wet human dermis with no obvious sign of thermal damage to the surrounding materials via the USP laser plasma-mediated ablation. However, soft tissues like wet dermis are deformable and apt to dehydrate during laser processing. Deformation degrades the ablation accuracy and increases the difficulty of manipulation. Undesired dehydration may alter the tissue morphology and property. To overcome these shortcomings, it is worth considering soft tissue lyophilization. Freeze-drying is a common method for tissue preservation that has many advantages, such as decreasing of both surgical time and surgical morbidity, eliminating antigenicity and preventing a foreign body type of reaction, and simplifying storage and distribution of donor tissues [106]. For freeze-dried bone graft, it may be stored in sealed evacuated container for several years and then be successfully used clinically [107]. According to private communications with Schuler and Gertzman at the MTF [1], freeze-dried soft tissue can be fully re-hydrated in a sterile solution and positioned or draped wherever it is needed for implantation.

By using freeze-dried dermis, the experimental setup and manipulation of tissues can be simplified and water absorption of light in the tissue is not a concern anymore.

This provides another method for the micro-processing of tissue via USP laser with simpler experimental set up, especially for the thin layer stripping of tissue. Besides, it is possible to compare the differences of wet dermis and freeze-dried dermis ablation and micro-processing of real tissue.

## ***4.2. Materials and Methods***

### **4.2.1. Experimental Set up**

The main experimental setup for fundamental study of freeze-dried dermis is same as wet dermis tissue experiment. The tissue sample was mounted to a work stage and the work stage was fixed to the 3-D automated translation stage through which the alignment of optics and laser scanning were realized. For the fundamental study of freeze-dried dermis, the experimental setup with a plate fixture for sample mounting as shown in Figure 3.1(a) in Chapter 3 was used. An evacuator system (FX225, EDSYN) was also employed to collect plasma plume residue and debris during the laser processing. The power loss through the beam delivery system is 50%, which has been accounted for in the irradiation pulse energy values stated hereafter.

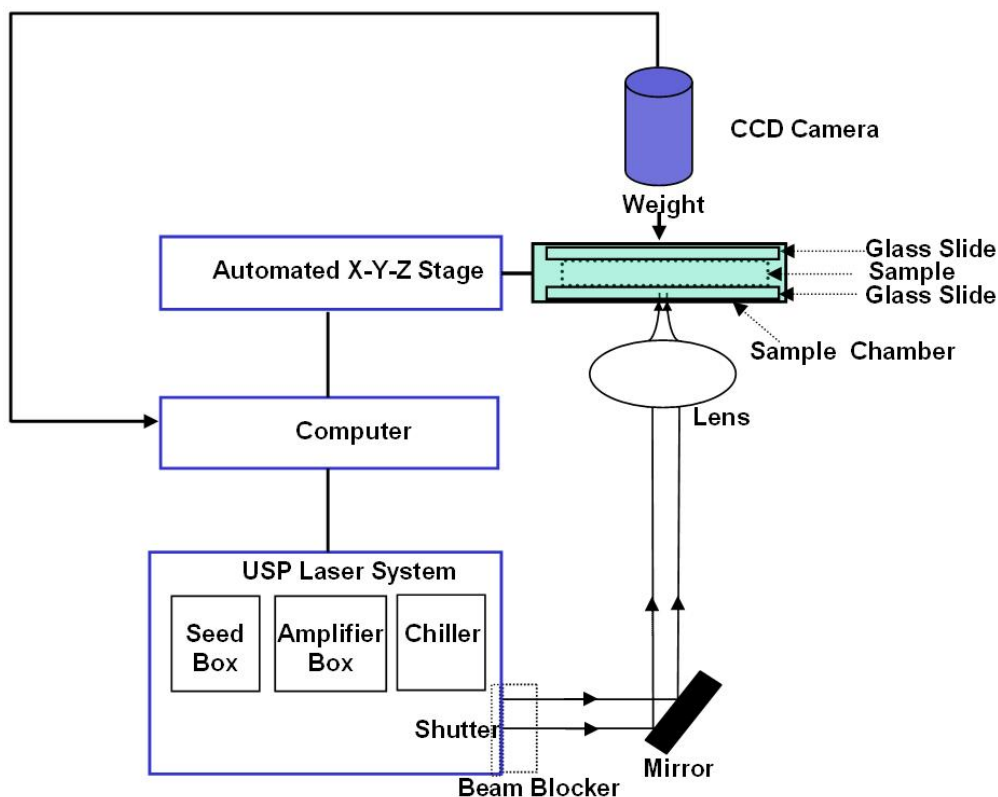


**Figure 4.1. Experimental Setups for the USP Laser Freeze-dried Tissue Layer Stripping.**

For freeze-dried dermis stripping, the setup shown in Fig 4.1 was adopted designed by Raydiance, Inc. The tissue sample was sandwiched by two glass slides in the sample chamber and was kept flat by adding a proper weight on the top glass slide. The laser beam passes through the bottom glass slide with negligible power loss and is focused into a certain depth inside the tissue for stripping by area scan ablation. To ensure that the focal plane was inside the tissue sample, the focal spot was firstly adjusted to the top surface of the bottom glass slide through the observation of the third harmonic generation of green spark; and keep focal spot moving towards the sample until the green spark almost vanished, then the desired depth was adjusted inside the sample for the focal plane.

### **4.2.2. Tissue Sample Preparation**

Freeze-dried dermal tissues were prepared from wet dermis samples packaged in hydrated state provided by MTF. The wet soft tissue was precut into proper portions and put into a freezer (-20°C). The tissue will become completely dry over a period of 12 hours and the samples can be stored at room temperature over a long period - months to years. Water absorption of light that impedes laser ablation inside wet tissues can be avoided in the freeze-dried dermis samples. Nevertheless, light scattering still exists in the freeze-dried tissues.

### **4.2.3. Measurements**

Following the ablation experiment, an upright digital microscope (National Optical DC3-156-S) was utilized to examine the micro topography and surface quality of the ablated tissue samples. Precise inspection and measurement of the ablation features were conducted by SEM (AMRAY 1830I). The ablation depths and thin layer tissue thickness were measured by a surface profiler (DEKTAK 3030). For histological evaluation, the samples were routinely processed as the wet dermis tissue preparation in Chapter 3. The analysis and photograph were performed by a Nikon ECLIPSE E600 microscope system.

### **4.3. Results and Discussion**

#### **4.3.1. Single Line Surface Ablation**

Similar to wet dermis sample, we have used line scanning surface ablation on the freeze-dried dermis tissue to determine the ablation threshold. Because the ablation crater for single spot ablation on the freeze-dried dermis surface is still hard to check and the energy level of the laser system is not high enough to exceed the ablation threshold for single pulse ablation and easily generate ablation crater, although it is dry and not deformable.

Multiple tissue samples have been chosen to study single line scanning ablation features on sample surface with different laser parameters. After irradiation, digital microscopy was used to inspect the ablated features of the tissue sample and the measurements of ablation line features were conducted by SEM. Figure 4.2(a) shows the microscopic view (400X magnification) of four laser scanned lines on the surface of freeze-dried dermis with different irradiation pulse energies (0.75  $\mu\text{J}$  - 2.5  $\mu\text{J}$ ) and the same pulse overlap rate - 20 pulses/ $\mu\text{m}$ . Figure 4.2(b) shows the microscopic view (400X magnification) of five laser scanned lines on the surface with the same pulse energy (2.5  $\mu\text{J}$ ) and different pulse overlap rate (1.25 - 20 pulses/ $\mu\text{m}$ ). Each line was scanned only once.

However, further inspection of the ablation lines from SEM reveals that there are bumps along the edges of the ablation grooves which can not be seen from microscopy

view, as shown in Fig. 4.3. So the microscopy view of the freeze-dermis tissue gives us misleading measurements that can not provide accurate results for ablation line width because of the bumps on the edge. To obtain accurate measurement of ablation features, such as ablation line width or depth, SEM image section view could be a proper way to check and measure the features.

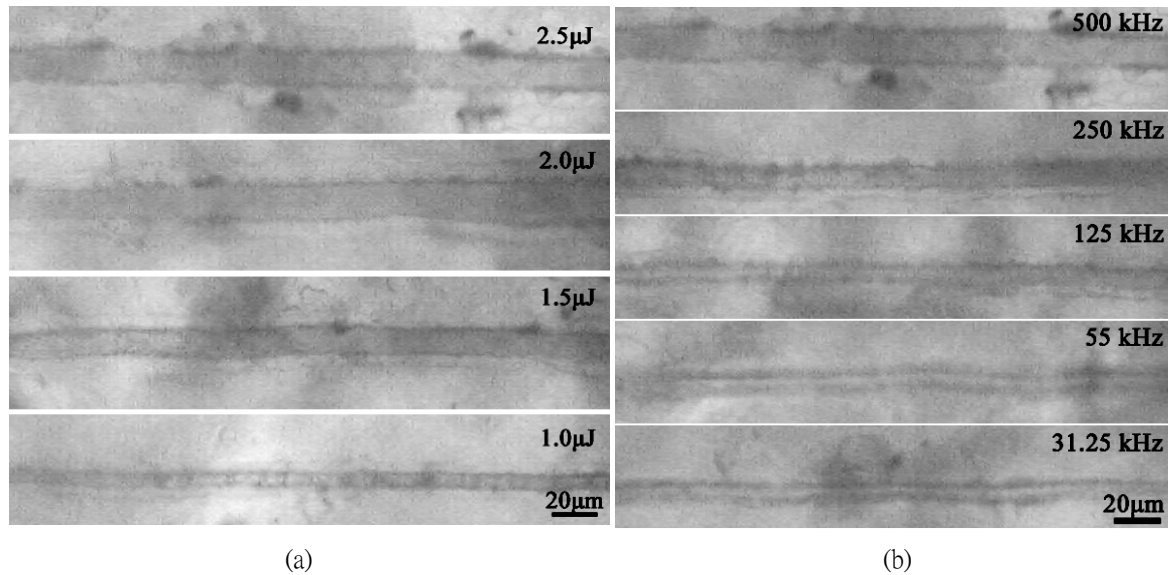


**Figure 4.2. Microscopy View of Single Line Ablation at the Freeze-dried Dermis Surface with Different Laser Parameters.**

**(a) Different Pulse Energy (20 pulses/μm), and (b) Different Repetition Rate (2.5 μJ).**

Four representative SEM images of the ablation lines shown in Fig. 4.3 were generated with different irradiation pulse energies and the same pulse overlap rate 20 pulses/μm (500 kHz repetition rate and 25 mm/s stage moving speed). Figs. 4.3 (a) and (b) show the top-view images for the cases of 2.5 and 2.0 μJ irradiation pulse energies, and one can measure the ablation line width as  $17.8 \pm 1.1 \mu\text{m}$  and  $14.9 \pm 0.5 \mu\text{m}$ , respectively. The measurements were averaged from three experimental samples and the deviation represents the uncertainty. Figures 4.3 (c) and (d) show the SEM views with a tilt angle

for the ablation lines of 1.5 and 1.0  $\mu\text{J}$  irradiation pulse energies, respectively. One can see the surface roughness of the tissue samples. Bumps along the edges of the ablation grooves in the freeze-dried dermis are more obvious. This is different from our previous wet dermis ablation results [108], where no such bumps were formed. The height of the bulge is about 2-5  $\mu\text{m}$ . What caused the bulge is still not very clear; but similar phenomenon was observed in laser micromachining of grooves in silicon by Crawford *et al.* [109] and in laser cutting of FPCB by Shin *et al.* [110].

The measured ablation line widths and depths (represented by the symbols) for various pulse irradiation energies are displayed in Figs. 4.4(a) and (b), respectively. After obtaining the line widths, the effective radius,  $r_{\text{eff}}$ , of the focal spot and the ablation threshold  $F_{\text{th}}$  can be calculated from Eq. (2.1-2.2). The linear fittings of the square of the ablation line width versus the logarithm of the pulse irradiation energy are also drawn in Fig. 4.4(a). The calculated effective radii of the focal spots and ablation thresholds are listed in Table 4.1. The effective size of the focal spot increases with increasing pulse overlap rate and is in a range of 9 - 19  $\mu\text{m}$ , showing the same tendency and similar range like the wet dermis ablation [108]. It should be mentioned that the accumulated fluence for the present ablation lines is very high, especially for the case with 20 pulses/ $\mu\text{m}$  pulse overlap rate; and thus, the equivalent pulse number  $N$  is very large as calculated in Table 4.1. As mentioned by Bonse *et al.* [103], the data at high fluence points should be excluded from the linear fitting as for wet dermis sample in Chapter 3. Therefore, only low fluence points in Fig. 4.4(a) are adopted for the linear fitting to obtain the slope of the curve with 20 pulses/ $\mu\text{m}$  pulse overlap rate.

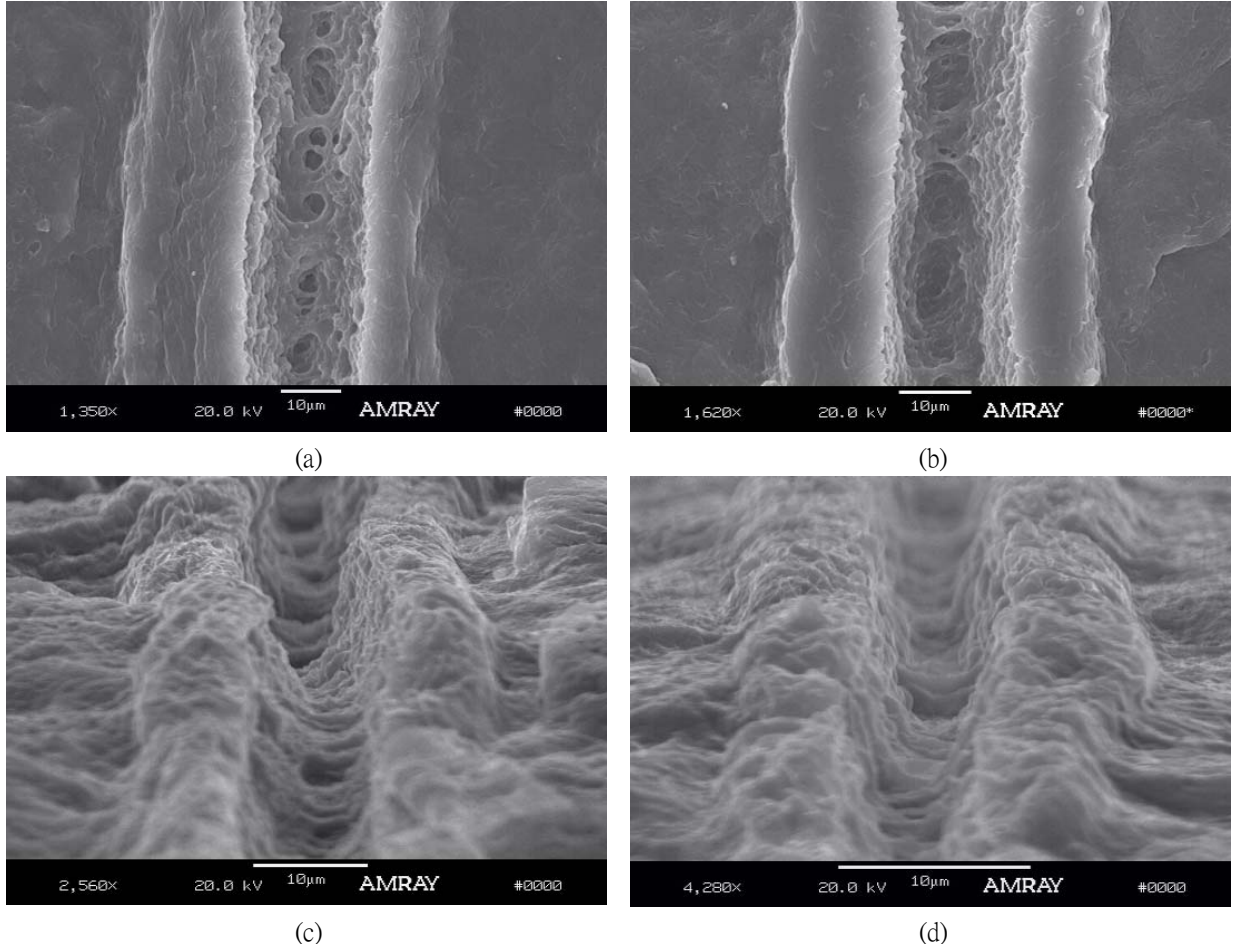


**Figure 4.3. SEM Images of Single Line Ablation at the Freeze-dried Dermis Surface with Different Irradiation Energies.**

**(a) 2.5  $\mu\text{J}$ , (b) 2.0  $\mu\text{J}$ , (c) 1.5  $\mu\text{J}$ , and (d) 1.0  $\mu\text{J}$ .**

**Table 4.1. Effective Focal Spot Radius and Ablation Threshold for Different Pulse Overlap Rates.**

Pulse Overlap Rate, $f / s$ (pulses/ $\mu\text{m}$ )	2	5	10	20
Equivalent Pulse Number, $N$	18	51	124	372
Effective Focal Spot Radius $r_{eff}$ ( $\mu\text{m}$ )	4.4	5.1	6.2	9.3
Threshold, $F_{th}$ ( $\text{J}/\text{cm}^2$ )	2.21	1.41	0.92	0.56



From Table 4.1, it is seen that the ablation threshold decreases as the pulse overlap rate increases. The incubation factor  $\xi$  calculated from the data in Table 4.1 is  $0.54 \pm 0.01$  for the freeze-dried dermis. Further, the ablation threshold  $F_{th}(1)$  for the freeze-dried dermis is determined as  $8.32 \pm 0.37 \text{ J/cm}^2$ . Comparing the freeze-dried dermis results with wet dermis experimental results in Chapter 3, it is found that the ablation threshold of the freeze-dried dermis is smaller than that of the wet dermis ( $9.65 \pm 1.21 \text{ J/cm}^2$ ). This is because there is no water absorption of light in dry tissues. A similar difference was noticed by Daminelli *et al.* [111] for silicon ablation in air and in water. As for the incubation factor, the current value for the freeze-dried is bigger than that of the wet dermis ( $0.38 \pm 0.03$ ). It means that the accumulation effect of continuous pulses for the freeze-dried dermis is not as profound as for the wet dermis.

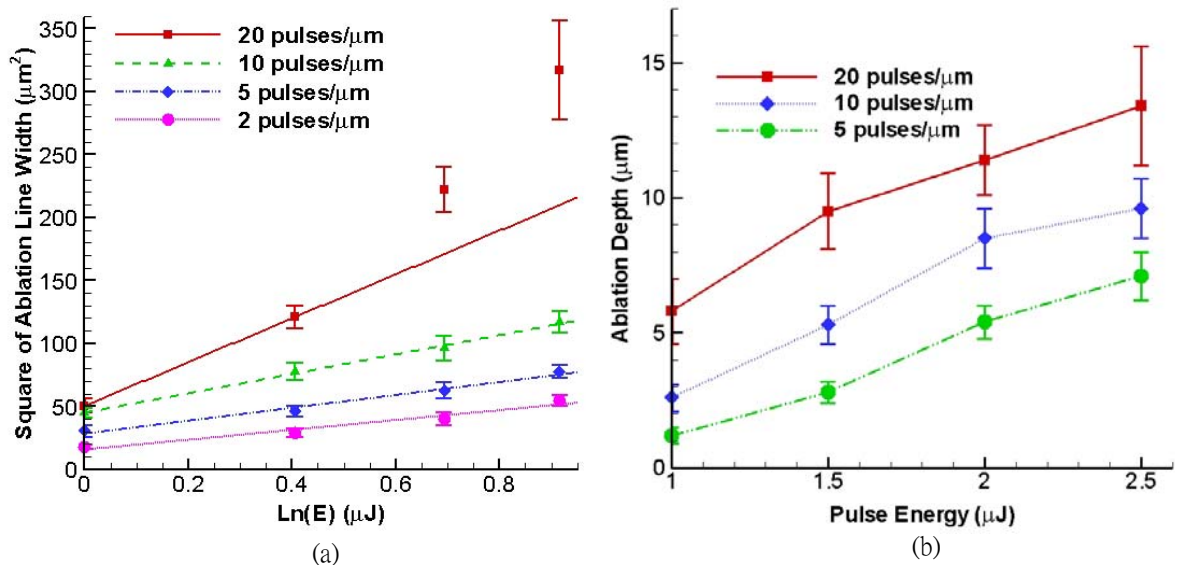
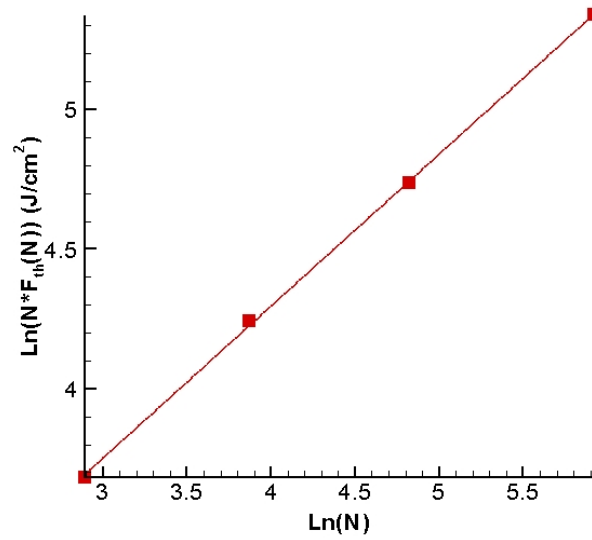


Figure 4.4. (a) Square of Ablation Line Width versus Pulse Irradiation Energy, and (b) Single Line Ablation Depth versus Pulse Irradiation Energy.



**Figure 4.5. Incubation Effect on Freeze-dried Dermis Single Line Ablation with Different Pulse Overlap Rate.**

### **4.3.2. Multi-line Surface Ablation**

Figure 4.6 shows the microscope view of multi-line scanning surface ablation on freeze-dried dermis sample (100X magnification) for different number of repeated lines ablation (1 line-200 lines) with 20 pulses/ $\mu\text{m}$  pulse overlap rate and 2.5  $\mu\text{J}$  pulse energy. Figure 4.7 shows the SEM images of multi-line surface ablation results (10 - 200 repeated lines) as shown in Fig. 4.6. During the processing of multi-line ablation, the ablation interface was always renewed by adjusting the laser beam focal spot position so that the laser ablation can be continued to the deep bottom of the grooves. As shown in the top-view images of Figs. 4.7(a) and (b), the ablation grooves become more clear and deeper when more repeated lines are scanned. However, the opening in the repeated scanning was not widened so that the repeated line ablation width is similar to that due to single line ablation. The SEM images viewed with a tilt angle in Figs. 4.7(c) and (d)

show details of the ablation line walls. Again bumps along the groove edges are observable.

Figure 4.8 shows the measured ablation line features due to multi-line repeated ablation. It is seen that, with increasing repeated lines, the ablation line width increases and the width increase slows down. The ablation depth increases rapidly when the repeated lines increase from 1 to 10 lines. However, statistically there is no change when the repeated lines increase from 50 to 200 lines. Thus, the ablation depth due to multi-line repeated ablation is not a simple multiplication of the corresponding single line ablation depth. This can be attributed to several factors. A major factor is the partial blockage of the laser beam to deep tissue due to the narrowness of the ablation channel and/or debris.

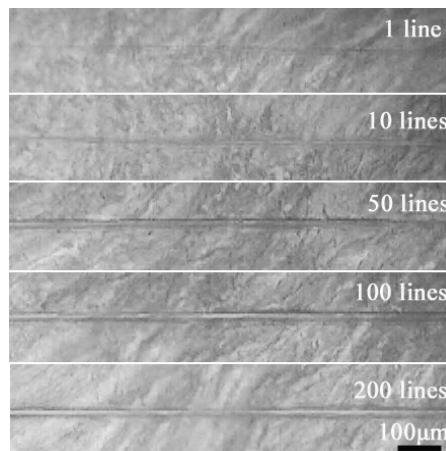


**Figure 4.6. Microscopy View of Multi-line Ablation at the Freeze-dried Dermis Surface with Different Repeat Lines (20 pulses/ $\mu\text{m}$ , 2.5  $\mu\text{J}$ ).**

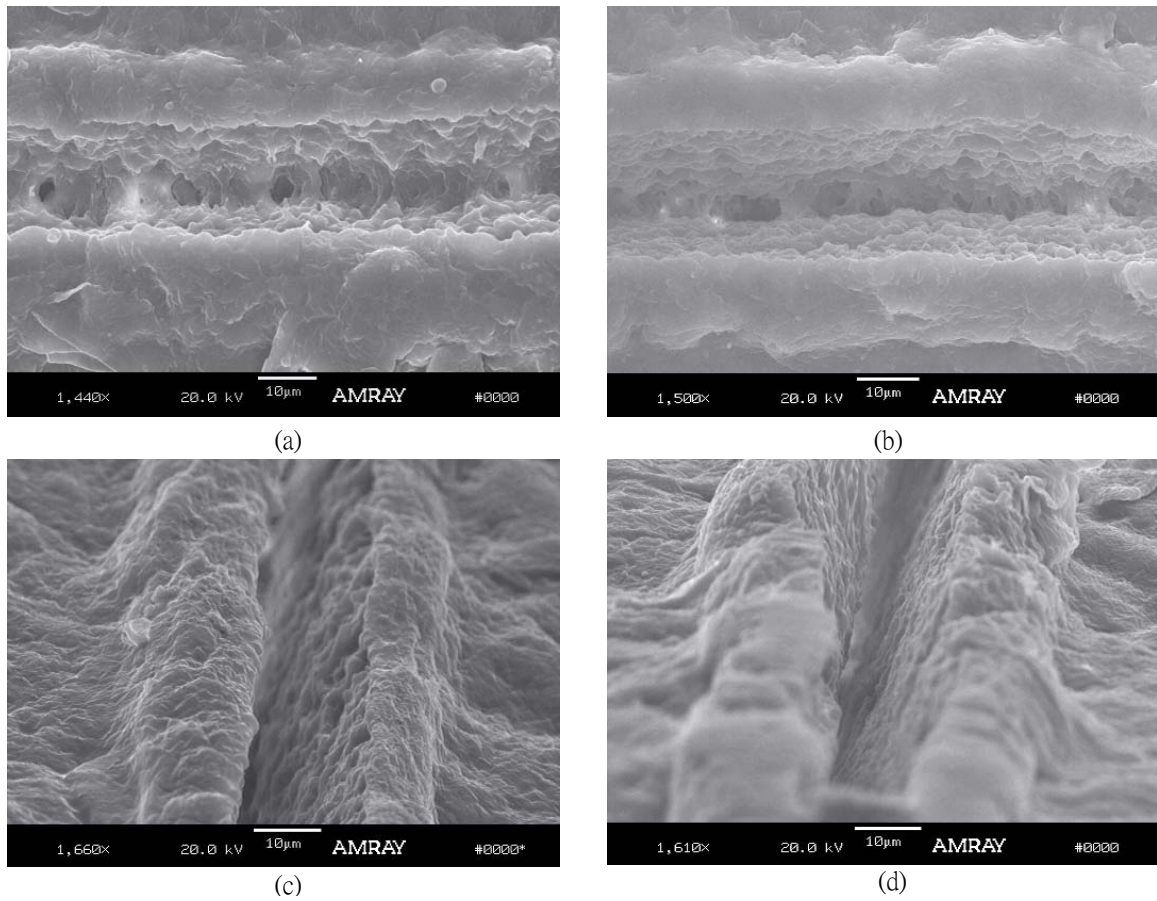


**Figure 4.7. SEM Images of Multi-line Surface Ablation at Freeze-dried Dermis with Pulse Irradiation Energy  $2.5 \mu\text{J}$  and Overlap Rate 20 pulses/ $\mu\text{m}$ .**

**(a) 10 Repeated Line Scanning, (b) 50 Repeated Line Scanning, (c) 100 Repeated Line Scanning, and (d) 200 Repeated Line Scanning.**

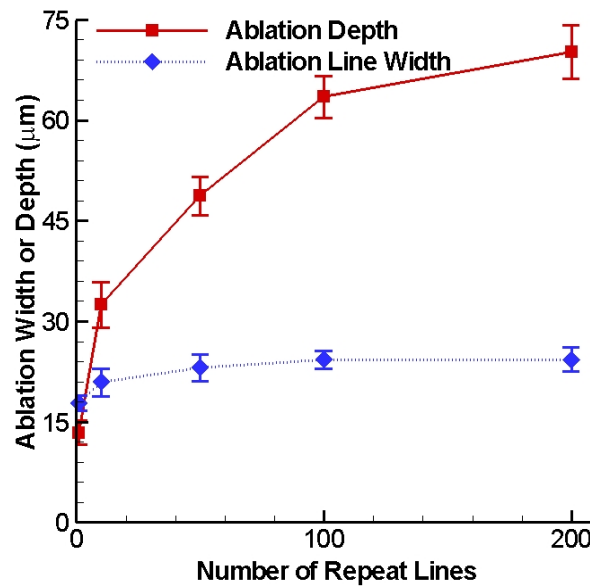
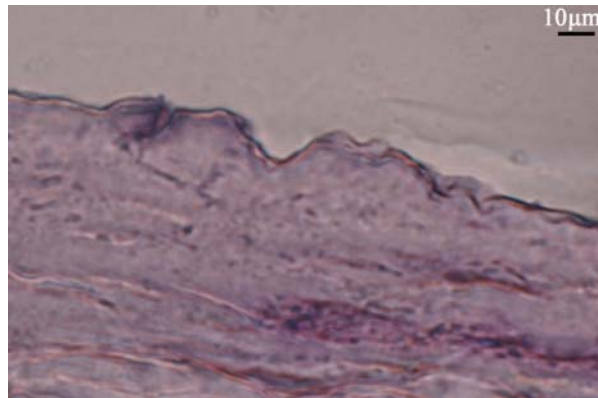


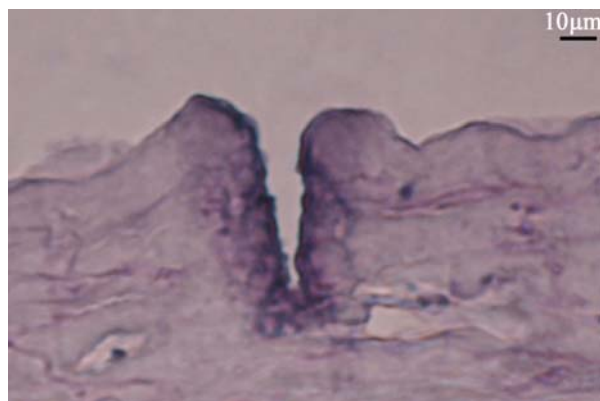
Figure 4.8. Ablation Depths and Widths Subject to Repeated Line Ablation with 2.5  $\mu\text{J}$  and 20 pulses/ $\mu\text{m}$ .

#### 4.3.3. Thermal Damage Investigation

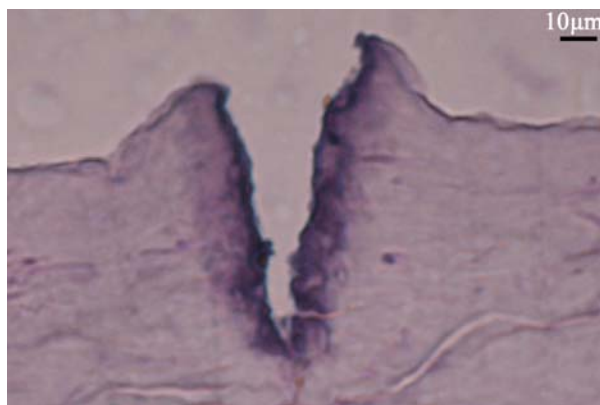
In order to judge the degree of thermal damage, the histology of the ablated tissue samples was analyzed. Figure 4.9 shows the routinely stained sections (1000X magnification) of slots cut in the freeze-dried dermis samples with same laser parameters (20 pulses/ $\mu\text{m}$  & 1.0  $\mu\text{J}$ ) and different repeated lines. The irradiation surface in the pictures faces up and the beam spot is around the middle in each picture. No thermal damage occurs for the single line ablation, as shown in Fig. 4.9(a). A clear cut to a certain depth can be observed in Figs. 4.9 (b) and (c) for multi-line ablation, in which a darkly stained lateral layer near the cut is observable. The thickness of the lateral thermal damage layer is less than 10  $\mu\text{m}$  for the 100 repeated line ablation. The more repeated lines scanned, the larger and the severer (darker) is the thermal damaged zone, because the accumulation of irradiation fluence is the key factor for causing thermal damage.



(a)



(b)



(c)

**Figure 4.9. Histological Views of the USP Laser Ablation in the Freeze-dried Dermis with Pulse Irradiation Energy 1.0  $\mu$ J and Overlap Rate 20 pulses/ $\mu$ m.**

**(a) Single Line Ablation; (b) 50 Repeated Line Ablation and Cut; and (c) 100 Repeated Line Ablation and Cut.**

#### 4.3.4. Freeze-dried Dermis Cut and Stripping

After parametric study of freeze-dried dermis, thin layer cut and stripping have been performed. Figure 4.10 shows the microscopic view (400X magnification) of partially successful cut through for a freeze-dried dermis sample with repeated line scanning (2.5  $\mu$ J pulse energy and 1 pulse/ $\mu$ m pulse overlap rate). The average thickness of the original freeze-dried dermis sample is about 0.2 mm. The tissue sample was repeatedly line scanned for 300 times and during the experiment, adjustment of the Y-axis position of the tissue sample was necessary to re-align the deeper un-ablated tissue to the laser beam focal position. At the edge of the tissue sample, about 50  $\mu$ m long scanned line has been totally cut through, which is indicated by the solid arrow in Fig. 4.10, since the edge area is thinner (about 100  $\mu$ m). The hollow arrow refers to the ablation area with partially cut inside the sample since the total depth is larger than the ablation depth limit. As shown in Fig. 4.10, no visible thermal damage was found in the cut edges after experiment. Figure 4.11 shows the microscope view of the back side of the partially cut of the freeze-dried dermis by repeated line scanning ablation, and discontinuous ablation dots can be seen.

To demonstrate a potential of the USP laser ablation in freeze-dried dermis for enhancing the harvest of donor tissues or for preparing grafted tissues for proper transplantation and/or therapies, stripping of a thin-layer dermis slide has been performed and the results are shown in Fig. 4.12. The original freeze-dried dermis sample was about 12 mm long, 4 mm wide and 0.5 mm thick. The tissue sample was processed using the experimental setup shown in Fig. 4.1(b) by five times repeated area scanning (2  $\mu$ m apart

between successive scanning lines) with pulse irradiation energy 2.5  $\mu\text{J}$  and pulse overlap rate 1 pulse/ $\mu\text{m}$ . After the laser processing, the top glass slide was removed and the sample was peeled off from the bottom glass slide. The stripped thin-layer dermis in the photo of Fig. 4.12(a) sticks to the glass slide, remaining its shape and dimension. The stripped thin layer is 12 mm long, 0.6 mm wide and 0.027 mm thick. It could be rehydrated in water and peeled off from the glass slide when it is to be used. The removed tissue showing in the top of the photo is somewhat distorted and cocked up because of the force applied to during the peeling process. The stripping leaves a clear imprint in this tissue piece. Figure 4.12(b) is an SEM view of an edge in the stripped freeze-dried dermis layer.

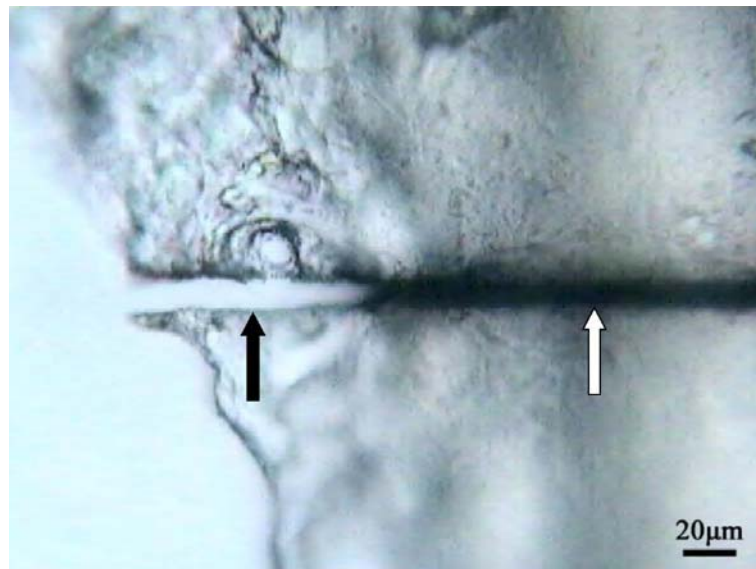


**Figure 4.10. Freeze-dried Dermis Cut by Repeated Line Scanning Ablation (Solid Arrow: Cut Through Area; Hollow arrow: Partially Cut Through Area).**



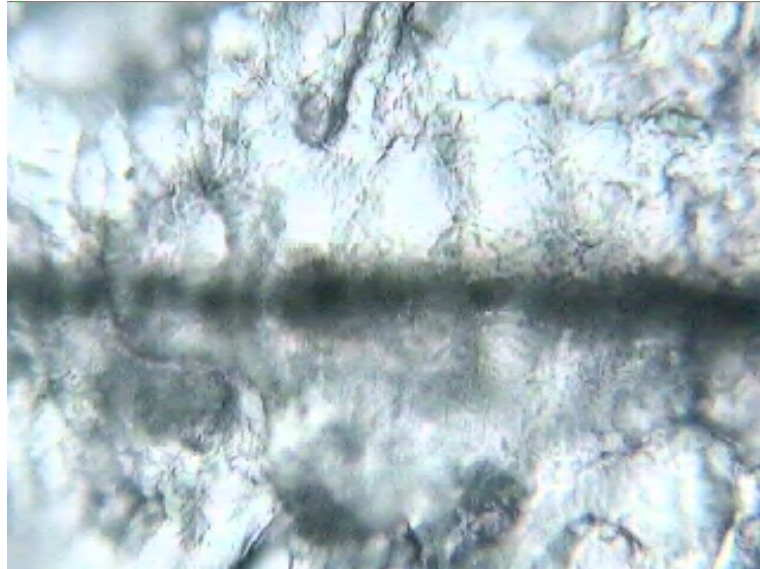


**Figure 4.11. Back Side Freeze-dried Dermis Cut by Repeated Line Scanning Ablation.**

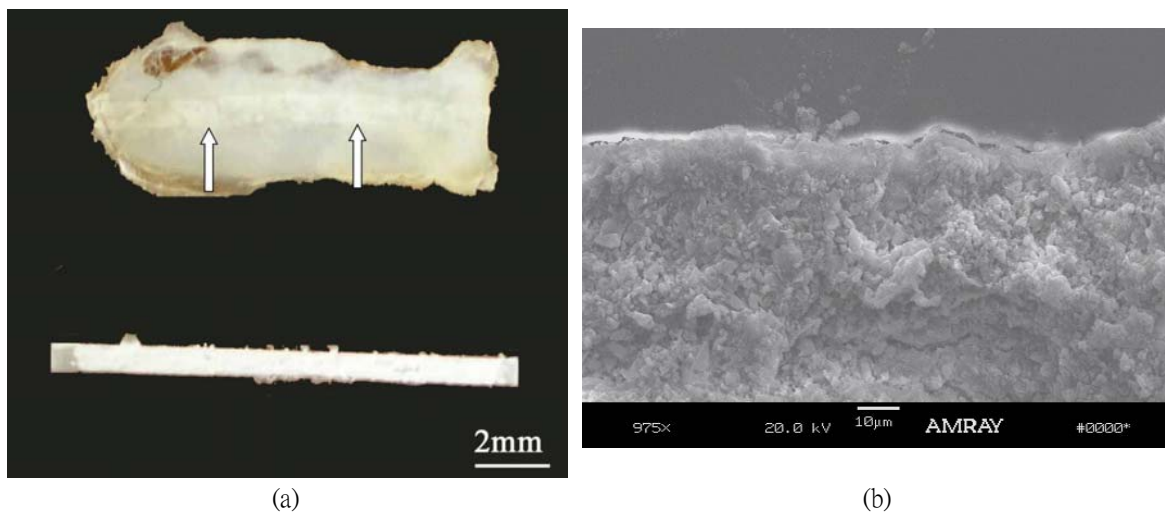


**Figure 4.12. Thin-layer Stripping from a Freeze-dried Dermis.**

**(a) Photo of the Dermis Sample (Upper Part) and Stripped Layer (Lower Part); Arrows in the Sample Show Where the Stripe Comes from, and (b) SEM Image of an Edge of the Stripped Thin Layer.**

Because of the strong attenuation of light scattering, there is a depth limit for the laser beam to be focused inside the freeze-dried dermis. So the thickness of the stripped

layer using the present method is limited to about 40  $\mu\text{m}$  for the freeze-dried dermis. Several freeze-dried dermis samples have been successfully stripped via the current instrument and the thicknesses of the thin layers are listed in Table 4.2. It is seen that the stripped dry dermis layers are much thinner than the separated thin layers of wet dermis in chapter 3. As compared with the wet dermis thin-layer separation, the present instrument for freeze-dried dermis stripping is simpler and more efficient. In particular, no specific feeding mechanism or design is needed.

**Table 4.2. Results from Several Freeze-dried Dermis Stripping Tests.**

Sample No.	Original Thickness of Dermis ( $\mu\text{m}$ )	Thickness of the Stripped Thin Layer ( $\mu\text{m}$ )
1	460	$22.3 \pm 8.1$
2	500	$26.9 \pm 7.7$
3	400	$32.5 \pm 9.5$
4	380	$33.8 \pm 9.9$

#### **4.4. Summary**

In this chapter, we have successfully achieved *in vitro* cut and stripping of freeze-dried human dermis via the USP laser plasma-mediated ablation. Firstly the parametric study of single line surface ablation was conducted to obtain the ablation threshold and incubation factor. Results were compared with previous study on wet dermis ablation. It is found that the threshold of single pulse ablation for the freeze-dried dermis ( $8.32 \pm 0.37 \text{ J/cm}^2$ ) is slightly smaller than that of wet dermis ( $9.65 \pm 1.21 \text{ J/cm}^2$ ) due to the light absorption of water in wet tissues. The incubation factor of the freeze-dried tissue

( $0.54 \pm 0.01$ ) is bigger than that of the wet dermis. Then the ablation features of multi-line surface scanning ablation were investigated. After that, histological examinations were performed and no thermal damage was found in the single line ablation results. Even in multi-line ablation, thermal damage was insignificant and the lateral damage zone was generally within 10  $\mu\text{m}$  in the results for continuously multi-line scanning. Finally the stripping of thin dermis layers was demonstrated by the USP laser ablation. The thickness of the stripped freeze-dried dermis was in the range of 20 - 40  $\mu\text{m}$ . No severe thermal damage like charring existed in the cut and layer stripping results. This project has provided a simpler yet effective method that can precisely and non-intrusively process soft tissues via the USP laser plasma-mediated ablation with minimized thermal damage.

## Chapter 5.

### Theoretical Analysis of Thermal Damage

#### ***5.1. Introduction***

From a practical point of view, ultra-short pulse ablation suffers from the problem of relatively small amount of ablated tissue per pulse. Attempting to increase the ablation rate by increasing pulse fluence is frustrated because of plasma shielding effects. More importantly, when ultra-short laser pulses are applied at high repetition rates, residual heat remaining in the non-ablated tissue may accumulate and lead to larger zones of thermal damage if the laser beam is applied to a single spot or even to laterally scanned line during ablation. This excessive heating at high pulse repetition rate as well as excessive mechanical stresses generated by each pulse significantly limits the ability of USP laser systems. A high repetition rate of the laser pulses can evoke an additional increase in temperature if the rate of heat transport is less than the rate of heat generation. When multiple pulses are delivered to a single location, both the extent of the thermal damage zone and the degree of thermal damage are influenced by heat accumulation from previous pulses. The time gap between continuous pulses for higher repetition rate is not large enough as compared with the thermal relaxation time. The thermal relaxation time is usually defined as the time needed for the temperature drops to 37% of the peak temperature. And generally if the time between two consecutive pulses is larger than the thermal relaxation time, thermal damage is minimized. However, for cases in which high peak temperatures are expected, the temperature value may still be sufficiently large to

induce thermal damage after thermal relaxation time has elapsed. For example, assuming an initial temperature of 20°C and a laser induced temperature rise to 80°C, the peak temperature will be approximately 42.2°C after the thermal relaxation time has elapsed. If another laser pulse is applied to the tissue at this point, thermal effects could be severer due to the superposition effects.

A practical USP laser tool must incorporate a pulse train of high pulse repetition rate. To anticipate the effect of such high pulse energy, high pulse repetition rate systems, the possible interaction between the pulses must be considered. For low repetition rate the effect of importance can be material modification by previous pulses. However, for USP laser the seed electrons for avalanche are produced by the multi-photon absorption and energy deposition are not sensitive to defects and impurities. The single pulse damage threshold is controlled by multiphoton ionization and electron avalanche development. It depends only on the pulse duration. For fixed pulse duration, the threshold is well defined and independent of beam size and repetition rate. An alternative source of decreased thresholds is “incubation” of electronic defects with finite absorption. This mechanism exhibits repetition rate dependence because of the finite lifetimes of the defects.

Modeling indicates that the thermal damage to tissue ablation is from material modification due to heat accumulation, rather than to incubation of electronic defects. Thus, thermal damage can be very important for high repetition rate USP laser ablation. The dependence of temperature on repetition rate of the laser pulses was modeled by van Gemert and Welch [112]. The significance of the repetition rate becomes evident when

the laser beam was focused on the same spot of a human tooth at a repetition rate of 1 kHz. Although, usually such short pulses do not evoke any thermal effect, radial cracking and melting obviously occurred at the surface of the tooth [39]. Roider *et al.* [113] studied the selective damage to absorbing structures with repetitive exposure and pulse energies below ablation threshold by a 5  $\mu$ s pulse laser at 500 Hz. And a thermal model was developed and applied to the experiments. Choi *et al.* [114] in vivo clinically investigated the raster scans of pulsed CO<sub>2</sub> laser skin irradiation and it is found that although the time between pulses was greater than the thermal relaxation time of the skin, the peak temperature can reach 400 °C due to pulse stacking. And it is also shown that the concept of thermal relaxation time does not adequately provide a measure of time that can be used during multiple-pulse irradiation of tissue [115]. Neev *et al.* [116] showed that the thermal heating by the ultra-short (350 fs) pulse train caused much smaller collateral damage and small temperature increase compared with long pulses (1 ns). And Feit *et al.* [117] indicated by calculations that repetition rate of over 1 kHz should not result in serious thermal problems in most cases for 0.5 ps ultra-short pulses. Kim *et al.* [118] reported that the ablation threshold decreases with higher repetition rate and larger beam size due to heat accumulation and thermal damage can be important for high repetition rate ultra-short pulse laser ablation.

When intense pulses of laser radiation ablate biological tissue by depositing the energy in a very narrow layer near surface, the incident laser energy is partitioned into several components: part of the pulse energy is reflected by the plasma created during the pulse; part is ejected with the vapors during the ablation; part is used to break the bonds

in the material; and the rest is for material heating. To study the thermal effects in the irradiated tissue, we consider the absorption coefficient  $\alpha_0$ , which corresponds to the portion of the incident energy transferred to the material heating. If phase transition does not occur, an alternation in heat content  $\Delta Q$  induces a linear change in temperature  $\Delta T$  according to a basic law of thermodynamics

$$\Delta Q = mc\Delta T, \quad (5.1)$$

where  $m$  is the mass and  $c$  is the specific heat capacity. During the laser-tissue interaction, the main cause of the resulting thermal damage is the heat transfer, which includes heat conduction, heat convection and heat radiation. Usually, due to the moderate temperature achieved in most laser-tissue interactions and the low perfusivity of most tissues, heat radiation and convection can be neglected. Heat conduction is the primary mechanism by which heat is transferred to unexposed tissue structures.

The spatial extent of heat transfer is described by the time-dependent thermal penetration depth ( $\delta$ ), and the thermal penetration depth is the distance in which the temperature has decreased to  $1/e$  of its peak value and can be obtained by

$$\delta = \sqrt{4\alpha t} \quad (5.2)$$

where  $\alpha$  is the thermal diffusivity defined by

$$\alpha = \frac{k}{\rho c} \quad (5.3)$$

where  $\rho$  is the density. The thermal relaxation time is obtained by equating the optical penetration depth to the thermal penetration depth, hence

$$\tau = \frac{d^2}{4\alpha} \quad (5.4)$$

where  $\tau$  is the thermal relaxation time. For laser pulse duration,  $t_p < \tau$ , i.e. for USP lasers, heat does not even diffuse to the distance given by the optical penetration depth  $d$ . Hence, the thermal damage to non-decomposed tissue is negligible. For  $t_p > \tau$ , i.e. for long-pulsed lasers, heat can diffuse to a multiple of the optical penetration depth, and thermal damage to the tissue adjacent to the decomposed tissue is possible. From the thermal relaxation time of water [39], the shortest thermal relaxation time of approximately 1  $\mu s$  occurs at the absorption peak of water near 3  $\mu m$ . It was concluded that laser pulse durations  $\tau < 1 \mu s$  are usually not associated with thermal damage and this statement is also referred to as the “1  $\mu s$  rule”. For real human tissue like dermis, the thermal relaxation time may be much larger due to the smaller thermal diffusivity.

For the heat effect, the first mechanism by which tissue is thermally affected can be attributed to conformational changes of molecules. These effects, accompanied by bond destruction and membrane alternations, are summarized in the term “hyperthermia”



ranging from 42 - 50°C. If hyperthermia lasts for several minutes, a significant percentage of tissue will undergo necrosis as described by the Arrhenius relationship [39]. A measurable reduction in enzyme activity is observed beyond 50°C, resulting in a reduced energy transfer within the cell, immobility of cells. At 60°C, denaturation of proteins and collagen occurs, which leads to coagulation of tissue and necrosis of cells. At even higher temperatures (>80°C), membrane permeability is drastically increased, thereby destroying the otherwise maintained chemical concentrations. At 100°C, water molecules contained in most tissues start to vaporize. The large vaporization heat of water (2257 kJ/kg) is advantageous since the vapor generated carries away excess heat and helps to prevent any further increase in the temperature in adjacent tissue. Only if all the water molecules have been vaporized, and the laser exposure is still continuing, does the increase in temperature proceed. In excess of 150°C, carbonization occurs, which can be seen by the blackening of the tissue and the escaping of smoke.

In general, the exact temperature for the onset of the cell necrosis is rather difficult to determine. As a matter of fact, it was observed that not only the temperature achieved but also the temporal duration of this temperature plays a significant role for the induction of irreversible damage to the tissue. For the quantitative approximation, we use an Arrhenius relationship to quantify the severity of thermal damage [39]:

$$\frac{d\Omega}{dt} = A_0 e^{-\frac{\Delta E}{R_0 T}} \quad (5.5)$$

where  $\Omega$  is the index to quantify the severity of thermal damage;  $A_0$  is Arrhenius' constant,  $R_0$  is the universal gas constant,  $\Delta E$  is specific tissue property constant. For skin tissue, we assume complete necrosis occurs when  $\Omega = 1$ . By inserting an appropriate value of the tissue constants, it is capable to calculate the probable damage degree ( $^{\circ}\text{C}$ ) as a function of time  $t$ . Some experimental data for the two parameters  $A_0$  and  $\Delta E$  can be found in literatures, although it is difficult to obtain due to the inhomogeneity of most tissues. For skin tissue,  $A = 3.1 \times 10^{98} \text{ s}^{-1}$  and  $\Delta E = 6.3 \times 10^5 \text{ J/mol}$  and the critical temperatures for the occurrence of cell necrosis is shown in Fig. 5.1.

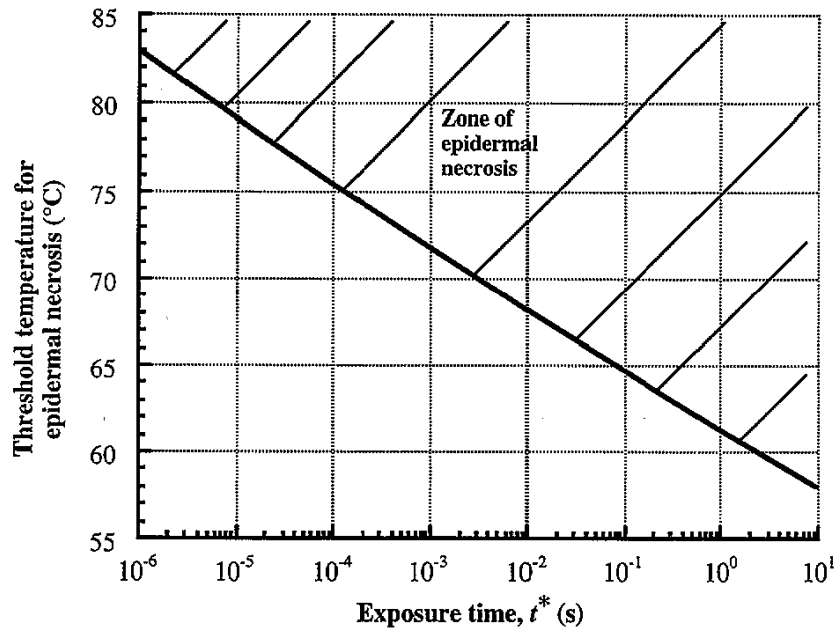


Figure 5.1. Threshold temperatures for thermal damage as a function of exposure time [119].

In this study, the pulse repetition rate is relatively high (usually above 20 kHz) and the time gap (2 - 50  $\mu\text{s}$ ) between two continuous pulses is less than the thermal relaxation time of dermis tissue (56  $\mu\text{s}$  for characteristic length of the focal spot radius).

Meanwhile, the pulse overlap rate is usually above 5 pulses/ $\mu\text{m}$  and for a given location along the scanning path, there are tens of equivalent pulses irradiated on this unit area as calculated and a condition where ablation may occur at pulse fluence smaller than that required for ablation with a single pulse. So because of this and the fact that the tissue may not cool completely between continuous pulses, a cumulative temperature build up can take place, resulting in thermal damage of the tissue.

The study in this chapter is trying to find the analytical formulation between laser parameters (pulse energy, repetition rate and pulse overlap rate) and thermal damage zone size and give a proper range of laser parameters used for larger material volume removal while, at the same time, still confining and minimizing thermal damage and the cumulative thermal effects will not be generated. USP laser systems could, therefore, become practical tools in many hard and soft tissue applications.

## ***5.2. Physical Model***

For USP laser line scanning ablation with higher pulse overlap rate, there are intensive pulse overlap for a unit focal spot location, and multiple pulses are deposited on this unit area and the ablation depth and width increase with the pulse numbers, as described in Chapter 3 & 4. Furthermore, the plasma-mediated ablation process is very complicated and the laser energy is mainly absorbed by non-linear absorption. Figure 5.2 shows an ideal 2-D sketch of multiple pulses (three) ablation processing, for the first laser pulse, ablation volume No.1 will be generated as a cylinder and the ablation depth and width will be increased for the second and third pulses. In this processing, the thermal

heating processing is also coupled and the part of laser energy for thermal heating will be absorbed along the ablation volume edges. The tissue domain is very large compared with the ablation volume and constant temperature may be assumed for the outer tissue boundaries, except for the top surface there is convection heat transfer with ambient air. So this is a complex 2-D heat conduction problem with non-homogeneous boundary condition. In this study, the analytical solution to the 2-D inhomogeneous heat conduction equation will be very complicated, so one simplified 1-D physical model was established to analyze the thermal effect.

To simplify the analysis, several assumptions have been made as listed below: (1) The plasma-mediated ablation processing is not considered here and the side effects such as shock wave, cavitation and jet formation are not considered. It is assumed that there is no influence for the boundary conditions of this problem from the electron temperature in the ablation process, and only the portion of the incident energy transferred to the material heating will be considered as the energy source for thermal damage analysis; (2) The lateral directional temperature increase and thermal damage (radius direction) is considered only and the vertical direction is not considered since the sample will be separated vertically finally; (3) It is assumed that the material is homogeneous and the thermophysical properties are independent on temperature, even though thermal and optical properties may change during the pulse and for consecutive pulses; (4) It is also assumed that there is no phase change for the lateral directional temperature increase.

In this study, the physical model for the thermal damage analysis is based on 1-D

cylindrical coordinate's heat transfer problem with consecutive laser pulses as the heat source. The studied domain is shown in Fig. 5.3 and the analysis is based on a 1-D heat transfer problem with  $a \leq r \leq b$ .

### 5.3. Initial and Boundary Conditions

For the initial conditions, since the experiments were conducted in the room temperature and the tissue has the same temperature with the room temperature -  $20^{\circ}\text{C}$ , the initial temperature difference for the tissue domain with air is zero.

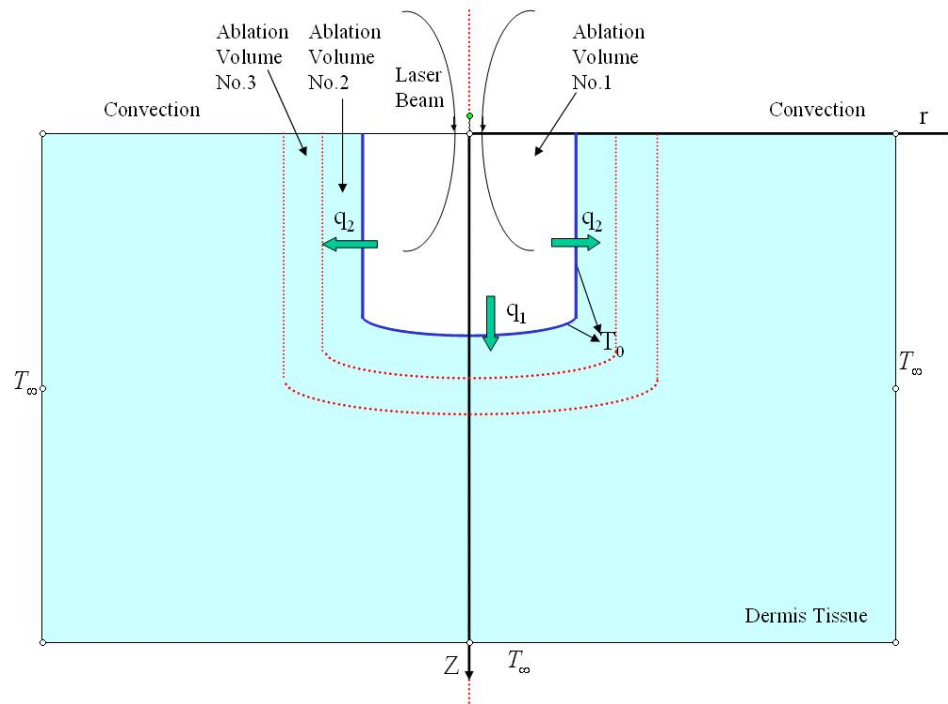
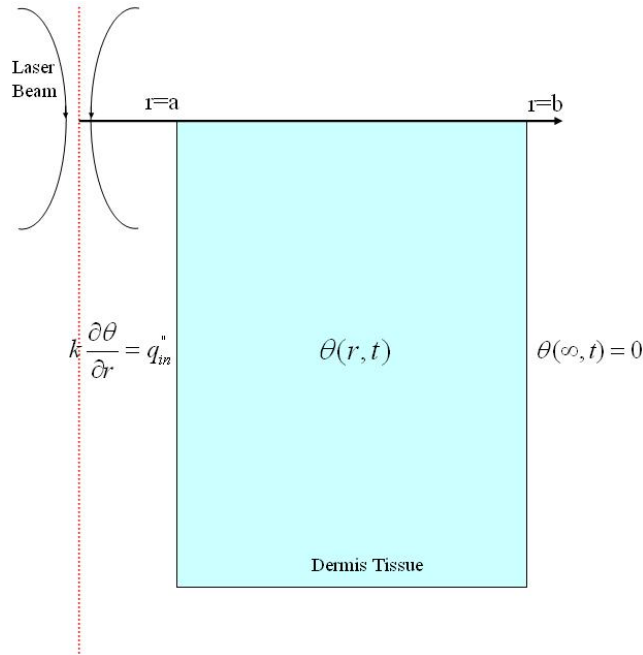


Figure 5.2. 2-D Cylindrical Coordinates Domain Sketch for Multi Pulse Ablation.



**Figure 5.3. 1-D Cylindrical Coordinates Domain for Thermal Damage Analysis.**

For the boundary condition, we can firstly consider that the convection heat transfer for the top surface is negligible here; the boundary condition for the top surface is thermal insulation. We can use the effective thermal conductivity and diffusivity when considering the convection term for the top surface, and available reference data for the effective thermal conductivity can be found for cool human skin tissue or in vivo skin tissue with blood perfusion [120, 121]. For the left boundary ( $r = a$ ), since the laser pulse will be deposited continuously, there is an instantaneous heat flux for left boundary as the pulses are deposited. Meanwhile immediately after the pulse incidence (pulse duration), thermal insulation is assumed for the time between two consecutive pulses since the ablation volume is so small compared with the whole domain and the heat transfer for the left boundary can also be neglected. For the right boundary ( $r = b$ ), the temperature ( $T_{\infty}$ ) is assumed to be constant as  $20^{\circ}\text{C}$  since the tissue volume is very large

compared with the ablation volume.

### 5.4. Mathematical Formulation

Considering the cylindrical ring domain ( $a \leq r \leq b$ ) in the 1-D model shown in Fig. 5.3, the net rate of heat gain by conduction minus rate of heat loss by convection equals the rate of energy stored. So the heat diffusion equation can be obtained as:

$$-\frac{\partial}{\partial r}(A_1(-\frac{\partial T(r,t)}{\partial r}))dr - h[T(r,t) - T_\infty]A_2 = \rho c \frac{\partial T(r,t)}{\partial t} \Delta V \quad (5.6)$$

where  $T(r,t)$  is the temperature of the domain with time and space (radius) variables;  $h$  is the convection heat transfer coefficient with air on the top surface;  $A_1$  is the surface area for conduction;  $A_2$  is the surface area for convection on the top surface;  $\Delta V$  is the confined volume considered. And we can have the Eq.(5.6) simplified as:

$$\frac{\partial^2 T(r,t)}{\partial r^2} + \frac{1}{r} \frac{\partial T(r,t)}{\partial r} - \frac{h}{kd}(T - T_\infty) = \frac{1}{\alpha} \frac{\partial T(r,t)}{\partial t} \quad (5.7)$$

If we define  $\theta(r,t) = T(r,t) - T_\infty$  for the temperature difference and firstly consider the situation without the heat convection term, Eq. (5.7) becomes:

$$\frac{\partial^2 \theta}{\partial r^2} + \frac{1}{r} \frac{\partial \theta}{\partial r} = \frac{1}{\alpha} \frac{\partial \theta}{\partial t} \quad (5.8)$$

For the situation with heat convection term, we can use the effective thermal diffusivity  $\alpha_{eff}$  to simplify the solving processing of the non-homogeneous equation. The boundary conditions and initial conditions are described as Eq. (5.9)-(5.11):

$$k \frac{\partial \theta}{\partial r} = q_{in}'' = f_1(r, t), \text{ at } r = a, t > 0 \quad (5.9)$$

$$\theta(b, t) = 0, \text{ at } r = b, t > 0 \quad (5.10)$$

$$\theta = 0, \text{ in the domain region } a \leq r \leq b, t = 0 \quad (5.11)$$

where  $q_{in}''$  is the heat flux from laser pulse energy and  $f_1(r, t)$  is the distribution function for the heat flux term for thermal heating.

Since the boundary condition (Eq. (5.9)) is non-homogeneous, different methodologies can be used to solve this partial differential equation, such as Duhamel's theory and Green's function. Duhamel's theorem provides a convenient approach for developing solution to heat conduction problems with time-dependent boundary conditions and it is based on superposition principle. Green's function method is flexible and systematic and it can give 2-D and 3-D transient problem solutions by multiplication of 1-D cases. Here we used Green's function since the Green's functions for pulse incidence situation and between two consecutive pulses situation are the same and it is convenient for future 2-D problem analysis. We firstly obtain the solution of the Eq. (5.8)



with homogeneous boundary conditions Eq. (5.12) to replace Eq. (5.9), and by using Green's function, the solution to the non-homogeneous problem can be obtained.

$$k \frac{\partial \theta}{\partial r} = 0, \text{ at } r = a, t > 0 \quad (5.12)$$

For the homogeneous heat conduction problem in the cylindrical coordinate system, by using separation of variables, it can be solved as a space and time-dependent functions. And for the time variable, the function is given by  $e^{-\alpha \beta_m^2 t}$ , and for space variable, the space-variable function is  $R(r)$  and listed as Eq. (5.13)-(5.15) [122].

$$\frac{\partial^2 R(r)}{\partial r^2} + \frac{1}{r} \frac{\partial R(r)}{\partial r} + \beta_m^2 R(r) = 0 \quad (5.13)$$

$$\frac{\partial R(r)}{\partial r} = 0, \text{ at } r = a \quad (5.14)$$

$$R(r) = 0, \text{ at } r = b \quad (5.15)$$

Finally, the complete solution  $\theta(r, t)$  can be written as Eq. (5.16):

$$\theta(r, t) = \sum_{m=1}^{\infty} C_m e^{-\alpha \beta_m^2 t} R(\beta_m, r) \quad (5.16)$$

$$C_m = \frac{1}{N(\beta_m)} \int_{r=a}^b r' R(\beta_m, r') F(r') dr' \quad (5.17)$$

and

$$\frac{1}{N(\beta_m)} = \frac{\pi^2}{2} \frac{\beta_m^2 J_0'^2(\beta_m a)}{J_0'^2(\beta_m a) - J_0'^2(\beta_m b)} = \frac{\pi^2}{2} \frac{\beta_m^4 J_1^2(\beta_m a)}{\beta_m^2 J_1^2(\beta_m a) - J_0^2(\beta_m b)} \quad (5.18)$$

where  $\beta_m$  are the eigenvalues and the eigenfunctions are shown as Eq. (5.19):

$$R_0(\beta_m, r) = J_0(\beta_m r) Y_0(\beta_m b) - J_0(\beta_m b) Y_0(\beta_m r) \quad (5.19)$$

The eigen-values are the positive roots of Eq. (5.20):

$$J_0'(\beta_m a) Y_0(\beta_m b) - J_0(\beta_m b) Y_0'(\beta_m a) = 0 \quad (5.20)$$

The desired Green's function is obtained by replacing  $t$  by  $(t - \tau)$  in the Eq. (5.16):

$$G(r, t | r', \tau) = \sum_{m=1}^{\infty} \frac{1}{N(\beta_m)} e^{-\alpha \beta_m^2 (t - \tau)} R_0(\beta_m, r) R_0(\beta_m, r') \quad (5.21)$$

So, finally the solution of the non-homogeneous problem (Eq. (5.8)-(5.11)) is in

terms of the above Green's function as:

$$\begin{aligned} \theta(r, t) = & \int_{r'=a}^b r' G(r, t | r', \tau) \Big|_{\tau=0} F(r', \tau) dr' \\ & + \frac{\alpha}{k} \int_{\tau=0}^t [f_1(r', \tau) r' G(r, t | r', \tau)] \Big|_{r'=a} d\tau - \alpha \int_{\tau=0}^t \left[ r' \frac{\partial G(r, t | r', \tau)}{\partial r'} \right] \Big|_{r'=b} f_2(\tau) d\tau \end{aligned} \quad (5.22)$$

The first term on the right-hand side of the Eq. (5.22) is for the contribution of the initial temperature distribution; that is, Green's function evaluated for  $\tau = 0$  is multiplied by  $F(r', \tau)$  and integrated for  $r'$ . The second term represents the contribution of the non-homogeneous term  $f_1(r', \tau)$  for boundary condition of the laser irradiation at  $r = a$ ; the third term represents the contribution of the non-homogeneous term  $f_2(\tau)$  for the boundary condition on the temperature at  $r = b$ .

So for the first pulse incidence, the temperature increase for the non-homogeneous problem can be obtained from Eq. (5.22):

$$\theta_1(r, t) = \frac{\alpha}{k} \int_{\tau=0}^{t_p} [r' G(r, t | r', \tau)] \Big|_{r'=a} q_{in}'' d\tau \quad (5.23)$$

where  $F(r', \tau) = 0$  for the initial condition  $\theta = 0$  for  $t = 0$ , and  $f_1(r', \tau) = q_{in}''$  is the part of the laser energy flux for thermal heating; So after obtaining the eigenvalues from Eq. (5.20), the temperature increase  $\theta_1(r, t)$  for different location ( $r$ ) and time ( $t$ ) can be

solved after the first pulse incidence by Eq. (5.23).

Then after the first laser pulse, there is a time gap  $t_g$  between two consecutive pulses before the second pulse so that the first laser pulse energy will be dissipated during this period. During this period, the heat conduction problem can be solved using the same method and the Green's function is the same as Eq. (5.21) since the homogeneous problem is the same. But for the final temperature increase  $\theta_2(r, t)$ , the initial condition is different since there is a temperature increase  $\theta_1(r, t)$  after the first incident pulse and there is no heat flux for the left boundary. So the final temperature increase after this dissipation time can be obtained by the following equation:

$$\theta_2(r, t) = \int_{r'=a}^b r' G(r, t | r', \tau) \big|_{\tau=0} \theta_1(r, t) dr' \quad (5.24)$$

So the temperature increase  $\theta_2(r, t)$  for different location ( $r$ ) and time ( $t$ ) can be solved after the first pulse incidence by Eq. (5.24). For the second pulse incidence, we can use the same heat flux for the left side boundary for the domain, and the temperature increase for the non-homogeneous problem can be obtained from the Green's function and the Green's function is also the same as previous situation. In the same way, we can have temperature increase  $\theta_3(r, t)$  for different location ( $r$ ) and time ( $t$ ) by Eq. (5.25).

$$\theta_3(r, t) = \int_{r'=a}^b r' G(r, t | r', \tau) \big|_{\tau=0} \theta_2(r, t) dr' + \frac{\alpha}{k} \int_{\tau=0}^{t_p} [r' G(r, t | r', \tau)] \big|_{r'=a} q_{in}'' d\tau \quad (5.25)$$

For the rest of consecutive pulses, we can obtain the temperature increase immediately after the  $N^{th}$  laser pulse incidence -  $\theta_{2N-1}(r, t)$  from Eq. (5.26):

$$\theta_{2N-1}(r, t) = \int_{r'=a}^b r' G(r, t | r', \tau) \big|_{\tau=0} \theta_{(2N-2)}(r, t) dr' + \frac{\alpha}{k} \int_{\tau=0}^t [r' G(r, t | r', \tau)] \big|_{r'=a} q_{in}'' d\tau \quad (5.26)$$

In the above equation, there are totally  $(2N-2)$  integration for  $dr'$  and  $m$  integration for  $d\tau$ . This iterative formulation gives the final solution immediately after the  $N^{th}$  pulse incidence together with  $(N-1)^{th}$  dissipation time between two consecutive pulses. And after the  $N^{th}$  pulse incidence, there is a diffusion time and the temperature increase is:

$$\theta_{2N}(r, t) = \int_{r'=a}^b r' G(r, t | r', \tau) \big|_{\tau=0} \theta_{(2N-1)}(r, t) dr' \quad (5.27)$$

So the final problem is to try to find the maximum  $r_{\max}$  where  $\theta_{2N}(r_{\max}, t) > \Delta T_{critical}$ ,  $t > 0, a \leq r \leq b$ , where  $\Delta T_{critical}$  is the critical temperature increase for thermal damage.

Meanwhile, the pulse number for a single pulse with pulse energy  $E$  and assume the laser energy is approximated by time average for the pulse duration, the energy flux for thermal heating ( $q_{in}''$ ) by this pulse can be obtained by Eq. (5.28):

$$q_{in}'' = \frac{\alpha_0 * E}{t_p * 2\pi * r * Z_r} \quad (5.28)$$

where  $Z_r$  is the Rayleigh length of the laser beam - the distance along the propagation direction of a beam from the waist to the place where the area of the cross section is doubled ( $Z_r = \frac{\pi r^2}{\lambda}$ ).

So the final formulation for the temperature increase with laser parameters is:

Find the maximum  $r_{\max}$ , where

$$\theta_{2m}(r, t) = \int_{r'=a}^b r' G(r_{\max}, t | r', \tau) |_{\tau=0} \theta_{(2m-1)}(r_{\max}, t) dr' > 40, t > 0, a \leq r \leq b.$$

For different pulse overlap rates used in the experiment, we can have the equivalent accumulated pulse number  $N$  from Eq. (2.4) for the same focal spot, and we can have the laser pulse energy and other information, such as the time gap between pulses for the specific repetition rate. Then from the analytical solution, we can get the temperature distribution for the whole processing, especially the temperature distribution after the total number of accumulated pulses incident on the target area. From the temperature increase for all the laser pulse incidence -  $\theta_{final}(r, t)$ , we can obtain how large is the region where  $\theta_{final}(r, t) \geq \Delta T_{critical}$ , and this region is defined as the thermal damage zone.

## 5.5. Results and Discussion

### 5.5.1. Wet Dermis Tissue Sample Ablation

Firstly and most importantly, the temperature distribution and thermal damage for line ablation of human dermis tissue were analyzed. It is assumed that 7% of the total pulse energy ( $\alpha_0 = 0.07$ ) is the part of energy for thermal heating, which is in the same range compared with results from experimental study and numerical modeling [39, 116, 123]. And the part of laser energy for thermal heating is divided by the fraction of the column size of the hollow cylinder to the whole ablation volume area, and we can assume the ablation crater diameter is equal to the ablation depth, so we can have  $q_{in}'' = 2.36 \times 10^{14} \text{ W/m}^2$  for pulse energy  $E = 2.5 \text{ } \mu\text{J}$ ,  $t_p = 900 \text{ fs}$ , and  $r = 4 \text{ } \mu\text{m}$ ). For the analytical calculation, initially  $\theta = 0$  and at a certain time ( $1 \text{ } \mu\text{s}$ ) the laser pulses begin to incident. And the pulse duration is 900 fs. The other properties of dermis tissue are listed in Table 5.1.

**Table 5.1. Thermal Properties for Dermis Tissue [35].**

Parameter	$\rho$	$k$	$\alpha$
Values	1125 kg/m <sup>3</sup>	0.30W/(m*K)	$7.21 \times 10^{-8} \text{ (m}^2/\text{s)}$

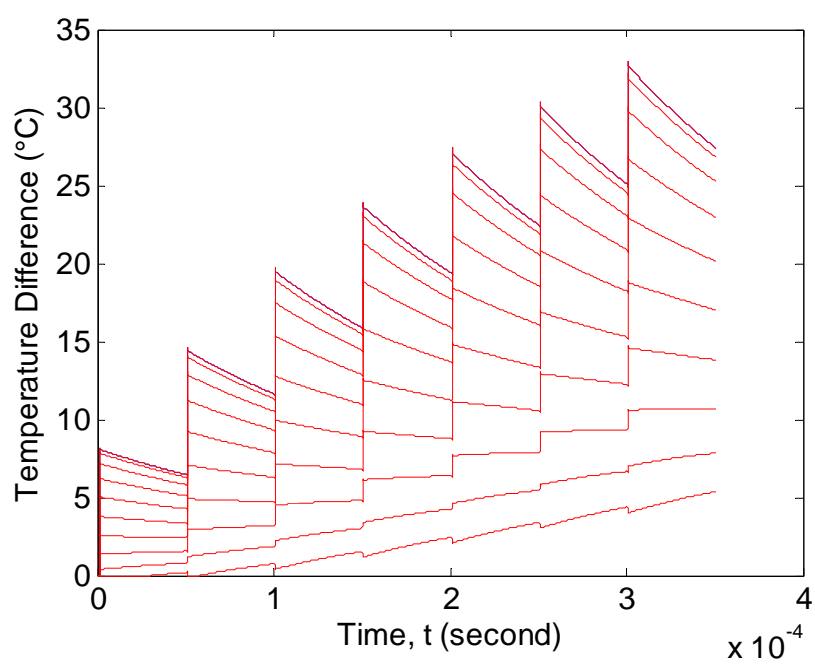
From the domain in this study, we have calculated the temperature distribution from  $4 \text{ } \mu\text{m} \leq r \leq 400 \text{ } \mu\text{m}$  (a=4  $\mu\text{m}$  is the left boundary and b=400  $\mu\text{m}$  is the right boundary). Before the analysis, model verifications with different domain and grid size

and time step have been checked to make sure the variation of the results are acceptable.

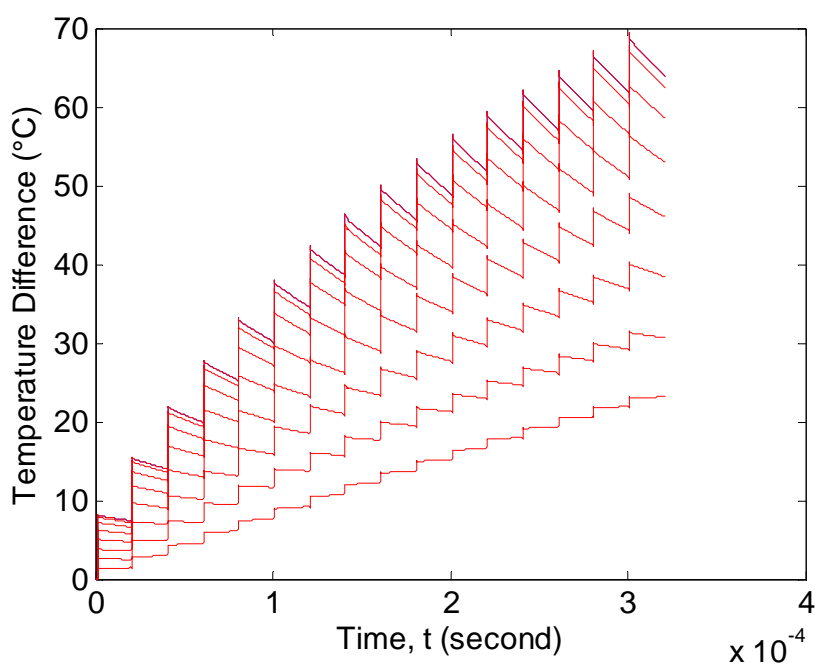
For the different pulse overlap rates used for wet human tissue single line ablation, the equivalent pulse number can be obtained by Eq. (2.4) and the total time for this  $N$  pulses deposition is usually in the time scale of  $10^{-4}$  s, for example, for 0.8 pulses/ $\mu\text{m}$  pulse overlap rate: the repetition rate  $f$  is 20 kHz, the time gap between two pulses is 50  $\mu\text{s}$  and the equivalent pulse number is 7. The total time ( $t_{total}$ ) for this 7 pulses incidence is:  $t_{total} = \frac{7}{20 \times 1000} = 3.5 \times 10^{-4} \text{ s}$ ; for 2 pulses/ $\mu\text{m}$  pulse overlap rate, the repetition rate  $f$  is 50 kHz, the time gap between two pulses is 20  $\mu\text{s}$  and the equivalent pulse number is 16. The total time ( $t_{total}$ ) for the total pulse incidence is:  $t_{total} = 3.2 \times 10^{-4} \text{ s}$ . For this time scale, the critical temperature needed for thermal damage from Fig. 5.1 is at least  $75^\circ\text{C}$ , so the critical temperature increase should be larger than  $55^\circ\text{C}$ .

Figure 5.4 shows the temperature increase with time for the pulse overlap rates - 0.8 pulse/ $\mu\text{m}$  (totally 7 pulses), 2 pulses/ $\mu\text{m}$  (totally 16 pulses) and 5 pulse/ $\mu\text{m}$  (totally 45 pulses) for different location. In Fig. 5.4(a), the top curve represents the temperature increase for  $r=4 \mu\text{m}$  and the lower curves represent  $r=5 - 13 \mu\text{m}$  with  $1 \mu\text{m}$  step increase for  $r$ . In the same way, Figure 5.4(b) represents the temperature increase for  $r=4 - 11 \mu\text{m}$  for the curves from top to bottom. From Fig. 5.4(a) and 5.4(b), we can see the temperature increase after the total pulses does not exceed  $55^\circ\text{C}$  for at least  $10^{-4}$  s, so there is no thermal damage zone for these two pulse overlap rates.





(a)



(b)

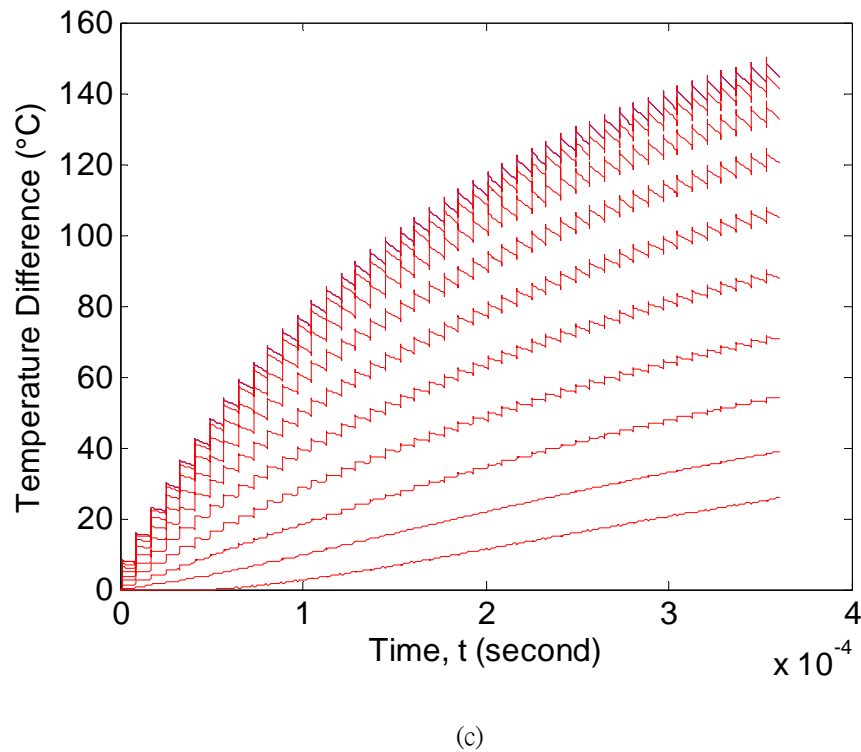


**Figure 5.4. Temperature Increase with Time for Different Location ( $4\mu\text{m} \leq r \leq 13\mu\text{m}$ ):**  
**(a) 0.8 pulses/ $\mu\text{m}$ , (b) 2 pulses/ $\mu\text{m}$ , and (c) 5 pulses/ $\mu\text{m}$ .**

However, Figure 5.4(c) shows the temperature increase of 5 pulses/ $\mu\text{m}$  ( $r = 4 - 11\mu\text{m}$  for the curves from top to bottom) for the left region exceeds the critical temperature increase -  $55^\circ\text{C}$  for over  $10^{-4}\text{s}$ , so there is thermal damage zone for this pulse overlap rate. Figure 5.5 plots the temperature increase profile versus different location (radial direction) with different pulse overlap rates (0.8 - 20 pulses/ $\mu\text{m}$ ) and  $2.5\mu\text{J}$  pulse energy right after all the pulse incidence. And as shown in Fig. 5.5, the temperature increase for the same left boundary location becomes larger with the increase of pulse overlap rate since the incident pulse number becomes larger, and for higher pulse overlap rate (5-20 pulses/ $\mu\text{m}$ ), the temperature increase is above  $100^\circ\text{C}$  or even higher. By selecting the critical temperature increase -  $55^\circ\text{C}$ , we can obtain the thermal damage zone size as indicated by

the red horizontal broken line. Table 5.2 lists the thermal damage zone size for different pulse overlap rates and 2.5  $\mu\text{J}$  pulse energy. As shown in Fig. 5.2, for lower pulse overlap rate (0.8 pulse/ $\mu\text{m}$ ), even for the highest pulse energy, there is no thermal damage zone. With higher pulse overlap rates used, the thermal damage zone becomes larger in the lateral direction.

Furthermore, there is convection heat transfer with ambient air from the top surface and this will decrease the thermal damage zone. This can be considered with effective heat thermal properties. Table 5.3 lists the thermal damage zone size considering the convection heat transfer with the ambient air for different pulse overlap rates and 2.5  $\mu\text{J}$  pulse energy. Here the effective thermal conductivity  $k_{eff}=0.55 \text{ W}/(\text{m}\cdot\text{K})$  and the effective thermal diffusivity is  $\alpha_{eff}=1.32 \times 10^{-7}(\text{m}^2/\text{s})$  [121]. And the thermal damage zone size becomes less for the same pulse overlap rates since the convection heat transfer with ambient air will dissipate the heating energy from laser pulse and reduce the thermal accumulation in the tissue target.

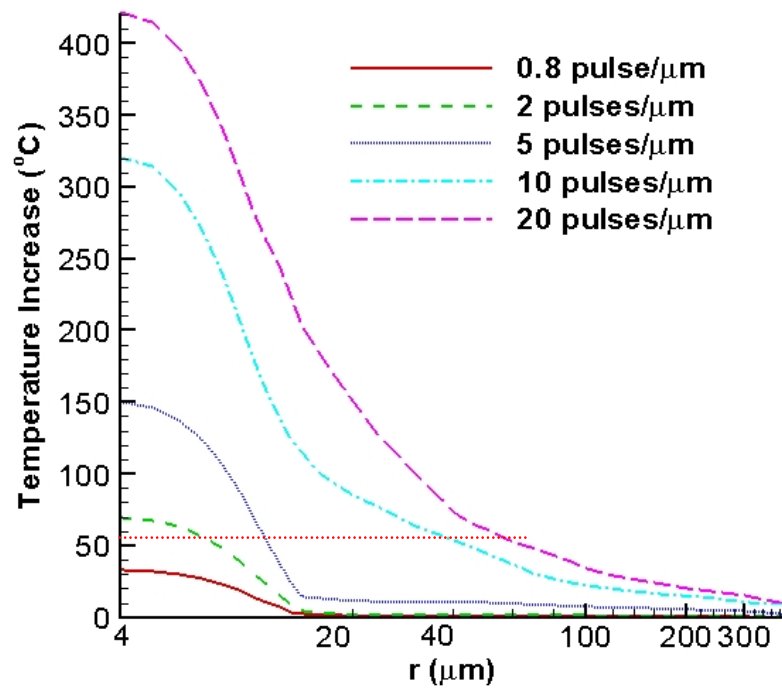


Figure 5.5. Temperature Increase along Different Location for Different Pulse Overlap Rates. (2.5  $\mu\text{J}$  Pulse Energy)

Table 5.2. Thermal Damage Zone for Different Pulse Overlap Rate. (2.5  $\mu\text{J}$  Pulse Energy)

Pulse Overlap Rate (pulses/ $\mu\text{m}$ )	0.8	2	5	10	20
Thermal Damage Zone ( $\mu\text{m}$ )	0	0	6	39	58

Table 5.3. Thermal Damage Zone for Different Pulse Overlap Rate with Effective Thermal Properties. (2.5  $\mu\text{J}$  Pulse Energy)

Pulse Overlap Rate (pulses/ $\mu\text{m}$ )	5	10	20
Thermal Damage Zone ( $\mu\text{m}$ )	5	31	47

### 5.5.2. Comparison with Experimental Results

Figure 5.6 shows the comparison thermal damage zone size between analytical results and experimental results. The isolated symbols represent the experimental results and the continuous curves represent the analytical results without considering convection heat transfer term. A good agreement is found between histological view results and analytical results for the increasing trend. But the thermal damage zone size from analytical result is relatively higher, one possible reason is that in the real experiments the absolute temperature in the tissue sample target area may be above  $100^{\circ}\text{C}$  and there is water evaporation in this region and this will consume large amount of energy for thermal heating and reduce the thermal damage zone. And another reason is the convection heat transfer with the ambient air has not been considered yet. If we consider the convection heat transfer term by using the effective thermal conductivity and diffusivity, the thermal damage zone size as listed in Table 5.3 becomes smaller and closer to the experimental results.

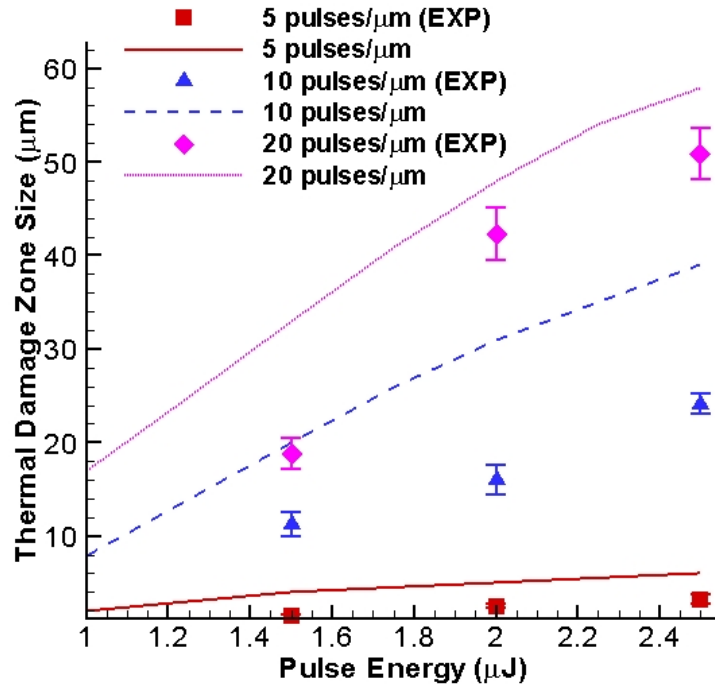


Figure 5.6. Thermal Damage Zone Size Compared with Experimental Investigations for Different Pulse Overlap Rates.

### 5.5.3. Key Laser Parameters

For line scanning ablation, there are many laser parameters that can influence the size of thermal damage zone, such as pulse energy ( $E$ ), pulse repetition rate ( $f$ ), stage moving speed ( $s$ ), laser beam focal spot size ( $r$ ), absorption coefficient ( $\alpha_0$ ) and pulse duration ( $t_p$ ). All of them are very important for the thermal damage zone, such as absorption coefficient -  $\alpha_0$ , it depends not only on material properties, but also on pulse duration, laser intensity, and other time dependent beam parameters. It is, therefore, difficult to reliably estimate and researchers have used the experimental data to define it [39, 116, 123]. Meanwhile, from the thermal damage check and measurement by histological view, we can estimate the absorption coefficient through the theoretical

analysis in this model. From the comparison of thermal damage zone sizes from histological view and theoretical calculation, the absorption coefficient used in the analysis is reasonable and can be used for further estimation of thermal damage zone. However, for a given laser system already focused, the pulse duration and the focal spot size are constant, and there are some key laser parameters that we can choose in real experiments, such as  $E$ ,  $f$  and  $f/s$ , and they have stronger impact for the thermal damage severity and the relationship between these parameters and the thermal damage zone size is desired.

#### **5.5.3.1. Pulse Energy**

The first important parameter for the thermal damage zone size is the pulse energy -  $E$  since it determines the total energy for thermal heating during the pulse incidence. With higher pulse energy for individual pulse, the portion of energy for thermal heating will become larger and the thermal damage will become severer, especially for higher pulse overlap rate since the ablation threshold is reduced due to the effects of accumulation by previous pulses. So the pulse energy level should be chosen to be close to the ablation threshold to ensure the ablation can happen continuously and the thermal damage is reduced or even eliminated. As shown in Fig. 5.6, the thermal damage zone size increases with the increasing of pulse energy for different pulse overlap rates. And for higher pulse overlap rate, the increase of thermal damage zone size is steeper since the ablation threshold for higher pulse overlap rate is reduced and the portion of pulse energy becomes larger for thermal heating in target in the ablation processing.

### 5.5.3.2. Pulse Overlap Rate

Differed from pulse repetition rate, pulse overlap rate determines the total pulse number for the unit deposited area and it represents the combined effect of pulse overlap rate and stage moving speed for line scanning ablation.

As shown in Fig. 5.4, the more pulses deposited, the higher temperature accumulated. And the thermal damage zone becomes very large for extremely high pulse overlap rate, such as 20 pulses/ $\mu\text{m}$ , and this is also consistent with previous histological results for single line and multi line scanning ablation.

Pulse repetition rate determines the time gap between two consecutive pulses and the length of this time gap determines how much heat will be dissipated further rather than stored locally. If the pulse repetition rate is small enough, the time gap between consecutive pulses is large enough for the energy dissipation from the edge to the inner materials, so the temperature increase will have an obvious reduction after the laser pulse incidence, such as for 0.8 pulse/ $\mu\text{m}$  as shown in Fig.5.4(a), for the first three pulses, the temperature drops about 2 - 3°C in the dissipation period; later on when the temperature goes higher, the range of the temperature drop also goes up to above 5°C, and this largely reduce the temperature increase and shrink the thermal damage zone. However, if the pulse repetition rate is high, the time gap between two consecutive pulses is very small and there is almost no dissipation for the instantaneous temperature increase on the edge between two pulses, as shown in Fig 5.4(c) for 5 pulses/ $\mu\text{m}$ , the temperature increase very fast as more pulses deposited in the same area, so the thermal damage zone becomes



larger.

## **5.6. Summary**

In this chapter, an analytical solution based on Green's function method is developed to analyze the temperature distributions and heat effected zones in materials irradiated by line scanning. We have theoretically analyzed the relationships between thermal effect and laser parameters based on several assumptions and a simplified 1-D physical model in cylindrical coordinates was established to solve the non-homogeneous heat conduction problem in the thermal heating processing. An analytical formulation was given to describe the temperature increase in the studied domain which considers all the laser parameters used, and the thermal damage zone criteria was defined by an Arrhenius relationship which considers both the achieved temperature and the temporal duration of this temperature.

To compare with real experiment, different temperature profiles and thermal damage zone was calculated with different laser parameters for wet dermis line scanning ablation. And the thermal damage zone size was also compared with the experimental results from histological check in Chapter 3. Both results show that the thermal damage can be confined in a small zone about 10  $\mu\text{m}$  with proper pulse energy and overlap rate. The significant effect of two key factors - pulse energy and pulse overlap rate were specifically discussed with relation to the thermal damage zone by parametric studies. This study gives a criteria for how to obtain the relationship between laser parameters (pulse energy, repetition rate and pulse overlap rate) and thermal damage zone size for

line scanning ablation, and it also provides guidance and proper range of laser parameters used for larger material volume removal while, at the same time, still confining and minimizing thermal damage. USP laser systems could, therefore, become practical tools in many hard and soft tissue applications.

## **Chapter 6.**

### **Near-field Nano-fabrication Based on Monolayer Spherical/Cylindrical Particles**

#### ***6.1. Introduction***

Laser, as a monochromatic and coherent light source, has been widely used in various areas such as tissue engineering, chemistry and biology, and for broad applications, such as optical imaging, laser surgery and laser fabrication. Examples of these applications have been introduced in previous chapters - polymer fabrication and tissue micro-processing. However, most of the applications are limited to micro scales, which results from the optical diffraction limit associated with classic optics. The classic optics, however, has the difficulty in confining optical fields to volumes sufficiently small for the purposes of characterization and fabrication in nano-scales. The smallest volume of a laser beam generated by conventional optics is governed by the optical diffraction limit.

Meanwhile, nanoscience and nano-fabrication of various materials have attracted growing scientific and industrial attention in the past decades due to their potentiality and applications in communications, biomedicine, chemistry, space exploration, tissue engineering and biomedical engineering, such as high-resolution lithography for nano-devices, nano-biotechnology applications, ultra-sensitive sensors and high-volume data storage. Therefore, to deal with structures with features less than 100 nm, fundamental

scientific breakthrough is needed if we want to apply technologies to nanoscience and nanotechnology. Several technologies have been investigated for nano-fabrication, such as the electron-beam lithography and imprint lithography. But for electron-beam lithography, it is a serial process and has low sample throughput and high sample cost; and for imprint lithography, mold is needed and hard to fabricate. Therefore an alternative approach is desired wherein a massive and parallel pattern in nano-scale can be achieved with high throughput and low cost. Optical near-field enhancement technology is one of the most promising techniques to circumvent the optical diffraction limit and produce nano-scale structures on the substrate. The main objective of this chapter is to explore the possibility and extend the capability of USP laser technology into this rapid developing field.

### **6.1.1. Near-field Optics and Intensity Enhancement**

Near-field optics is a branch of optics that considers configurations that depend on the passage of light to, from, through, or near an element with subwavelength features and the coupling of that light to a second element located a subwavelength distance from the first. A strong local optical field is established in the subwavelength region between the two objects, usually between nano-particles and substrates. This intensity enhancement is mainly due to the scattering and near-field effects by the nano-particles when the light travels through the particles and reaches the substrates.

Due to the intensity field enhancement in the near-field region, the optical power on the substrate surface can exceed the ablation threshold of the substrate material and

nano features can be generated. And this would lower the ablation threshold of the substrate material with direct irradiation and the feature size fabricated by this technique can be smaller than the half size of the incident light wavelength. As an evanescent wave, the optical field from near-field optics exhibits exponential decay with distance along the optical propagation direction. Due to their rapid decay, they are of importance only close to the interface.

### **6.1.2. Approaches to Achieve Near-field Intensity Enhancement**

Different approaches and techniques to achieve near-field enhancement techniques have been reported, such as near-field scanning optical microscope (NSOM) patterning technique, laser-assisted atomic force microscopy/scanning tunneling microscopy (AFM/STM)-tip patterning technique, nanolithography and nano particle-assisted near-field technique. In NSOM and AFM/STM systems, near-field enhancement can be achieved from an aperture or an apertureless metallic tip by creating a localized optical field in nano-scale at the tip apex. A strong local optical field is established between the sample surface and the sharp tip when the surface-to-tip gap is a few nanometers. Structures with dimensions below the minimal resolvable feature size of half a wavelength of the light were produced underneath the tip. However, this kind of near-field technique is difficult to control the sophisticated hardware systems used in these systems and the throughput is limited and has rarely been used in an industrial setting. Nanolithography needs a nanometer-scale circular- or square-shaped aperture as the mask, and suffers from extremely low light transmission.

Instead of tips, nano-particles can be used for creating nano-structures by utilizing the intensity enhancement in the near-field region. When the laser beam is incident on the top surface of particles, there is a field enhancement around the particles. This optical field enhancement by nano-particles can be explained by Rayleigh and Mie scattering theories. Such optical enhancement can lead to ablation of the substrate materials for nano-scale surface patterning. By using nano-particles, the diffraction limit of light has been circumvented and nano-features can be created on different substrate materials. In addition, this method is simple and is capable for massively parallel nano-fabrication on the surface.

### 6.1.3. Literature Review

For near-field enhancement techniques, the study by Grigoropoulos *et al.* [124] performed NSOM surface nano-structuring with minimum lateral dimension of ~10 nm and various complex nano patterns; Yi *et al.* [125] used laser-assisted STM to fabricate nano-scale dots and lines with high electrical conductivity on *p*-type silicon substrate with 30 nm dimension; Hong *et al.* [126] reported laser nano-fabrication with the combination of AFM, NSOM and transparent particles mask with feature size down to ~20 nm; Murphy-DuBay *et al.* [127] demonstrated experimental results of NSOM field enhancement using bowtie shape ridge antenna apertures for nanometer size structures manufacturing; Srituravanich *et al.* [128] demonstrated high-density nanolithography by utilizing surface plasmons and generated 90 nm dot array patterns with 365 nm wavelength light source.

For nano-particle assisted near-field fabrication technique, Heltzel *et al.* [129] reported micro-sphere based near-field nanofabrication with femtosecond laser irradiation with 300 nm and 250 nm for the feature diameters and depths, respectively. Huang *et al.* [130] both experimentally and theoretically studied the near-field effects of monodisperse silica and polystyrene spheres on Aluminum substrate using 248 nm and 23ns laser light with different particle size and laser fluence. Sakai *et al.* [131] reported dielectric particles sized mounted on glass surface by femtosecond laser pulses to produce 84 - 170 nm nano-hole overcome the diffraction limit. Munzer *et al.* [132] showed the results of utilizing small particles to produce holes on silicon and glass surfaces with femtosecond (100 fs) and nanosecond (8 ns) laser pulses; Guo *et al.* [133] demonstrated laser parallel writing of different profiled nano features on a 20-nm-thick eutectic  $\text{Sb}_{70}\text{Te}_{30}$  film coated on a polycarbonate substrate with multiangle scanning of laser irradiation. Li *et al.* [134] obtained 90 nm diameter of cavity by laser nano-imprinting with 0.16  $\mu\text{m}$  silica particles. Above all, the existing spherical particle based technique is usually a single-angle (normal to the sample surface) processing technique. And parallel continuous nano features, such as nano lines on substrates have not been demonstrated yet.

#### **6.1.4. Objectives**

The purpose of this project is trying to develop an effective, precise nano particle assisted nano-fabrication method by near field enhancement. By the alignment of the nano particles, we can further demonstrate parallel fabrication of nano line which is a very attractive and promising method for large volume nano-fabrication. The specific aims of this project include: (1) Design and build of a high-precision laser near-field

nano-fabrication set up; (2) Develop a cylindrical nano particle assisted near-field nano-fabrication technique on different substrate materials; (3) Analyze both with simulation model and experiment to study the mechanism (field intensity distribution) and influence of laser conditions and particle size for the nano feature fabrication, and optimize the fabrication process; (4) Establish a parallel large volume nano feature fabrication technique by using alignment and array of particles deposition method and laser scanning method.

The successful completion of the project provides an effective method for nano line fabrication, in particular for parallel large volume fabrication. And it will also provide a clear understanding of the physical basis to achieve more efficient and precise laser nano-fabrication with nano particles. This near-field laser fabrication technique has the following advantages: (1) It is simple and clean, with very straightforward and simple set up. Only a lens and a scanning stage are needed. (2) It can ensure precise surface processing with limited heat affected zone with the USP laser; (3) It is low cost and efficient for parallel large volume fabrication for industrial applications; (4) It can generate nano line pattern with controlled or even user-defined pattern; (5) It is material-independence due to the USP laser ablation mechanism;



## **6.2. Experiment**

### **6.2.1. Experiment Set up and Design**

In this study, a Tsunami mode-locked Ti:sapphire USP laser from Spectra-Physics (Fig. 6.1) was used as the laser source. It is pumped by a Millennia Vs J diode-pumped CW visible laser. The wavelength turning range for the Ti:sapphire laser is 710 - 980 nm and the repetition rate is 80 MHz. Its average power is to 800 mW at 790 nm wavelength. And the pulse duration can push to 80 fs. The optical delivery and alignment system is simple. An objective lens with short focal length (5 mm) is needed to focus the laser beam to be less than 10  $\mu\text{m}$  (from Eq. (1.1)) for the focal spot diameter so that the energy flux in the focal spot is strong enough for the experiment. A high-precision translation stages is needed for the sample position control and laser scanning. So the experimental set up is same as the set up for the USP line scanning ablation of tissue sample, as shown in Fig. 3.1(a).

Since the focal plane position is very critical to the near-field enhancement and the fabrication, the enhancement factors for different relative locations towards the particles are different. So by changing the focal plane position towards the particles, we can study the enhancement factor by measuring the fabricated features and give a relation between the focal plane position and the fabricated nano feature dimensions.

Furthermore, the nano particles should be scanned by the laser beam to generate nano line feature, so the high-precision translation stage should have high resolution of

around 10 nm and a good stage movement control system is also important for continuous nano feature generation. Nano line near-field fabrication is different with nano-hole fabrication with spherical particles since the length of the nano rod may be larger than the focal spot size and the laser beam should scan along the cylindrical particles to fabricate continuous lines.



**Figure 6.1. Ti:Sapphire Femtosecond Laser System.**

### **6.2.2. Particle Sample & Deposition Method**

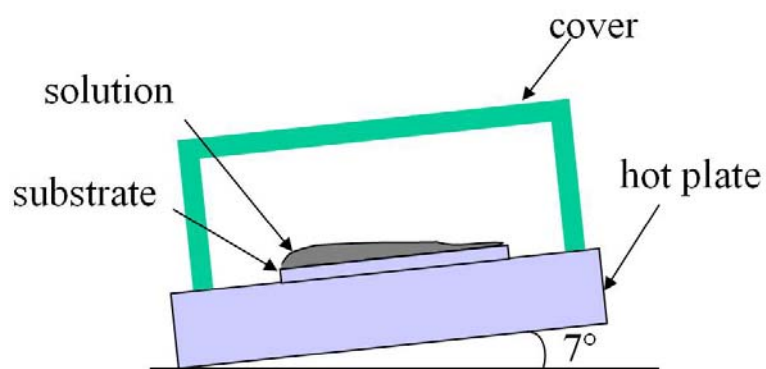
Firstly nano-hole fabrication demonstration was conducted by using spherical particles. The spherical particles used in this study are silica particles with 0.54  $\mu\text{m}$  diameter and 1.43-1.46 index of refraction (Bangs Lab). The deposition of nano particle is the first step for the near-field nano-fabrication. For monolayer spherical nano particles deposition, different methods and techniques have been tried, such as spinning and evaporation method [130, 135, 136]. One simple method is to use the self-assembly characterization of the spherical particles with tilt angle on a hot plate. For this method, a simple chamber consisting of a hot plate (30°C - 35°C) and a glass cover was used to

control the temperature and humidity for the evaporation processing. As shown in Fig. 6.2(a), the sample substrate was placed on the hot plate and covered by the glass cover. The chamber was tilted with an angle of  $7^\circ$ . The glass cover provided a relatively good thermal stability as well as protected the surface from the external air flow, which could disturb the self arrangement. The substrate materials used include PDMS and silicon in this study. A few drops of 0.05% colloids of silica spheres were applied onto the silicon or PDMS substrate. The monolayer silica spherical particles deposition has been developed very well and large area of monolayer deposition on silicon and PDMS can be achieved so far for further fabrication. Figure 6.2(b) shows the microscope view of monolayer silica spherical particle on silicon substrate. The monolayer particles can aggregate with each other and can be aligned very well with hexagon shape, as shown in Fig. 6.2(c).

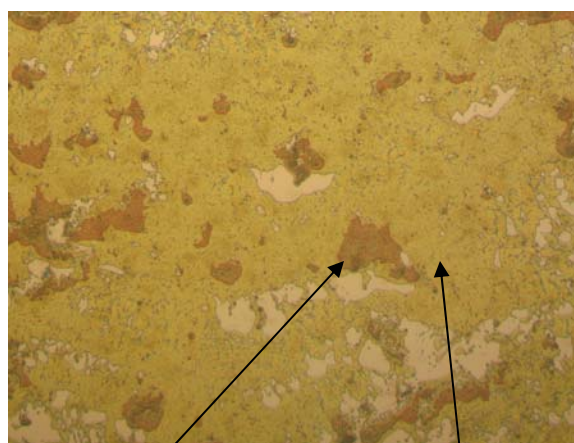
For nano line fabrication, cylindrical particles were used, such as Carbon Nano-Tube (CNT) or silica fiber rod. And the substrate materials used include PDMS and silicon. It is important to investigate the laser nano line processing with a single isolated cylindrical particle on the substrate at first. So for single cylindrical CNT particle deposition, we used the same method (Fig. 6.2(a)) as spherical silica particles to obtain single isolated cylindrical particle deposition on substrates. For single cylindrical silica fiber particle, a simple bond method was used with tape on both ends and ethanol was used to help the attachment of the tiny silica fiber rod on the substrates.

For large area multiple nano line fabrication, a particle deposition method to

obtain monolayer cylindrical particles on the substrate is needed. Here the deposition is different with spherical particles because self-assembly is not suitable for cylindrical particle alignment. There are different ways to align the particles. One simple way is to add an electrical field during the evaporation processing so that the cylindrical particles will be aligned with the same angle due to the electrical field force, as demonstrated by Park *et al.* [137] for the alignment of single wall CNT along the applied electric field.



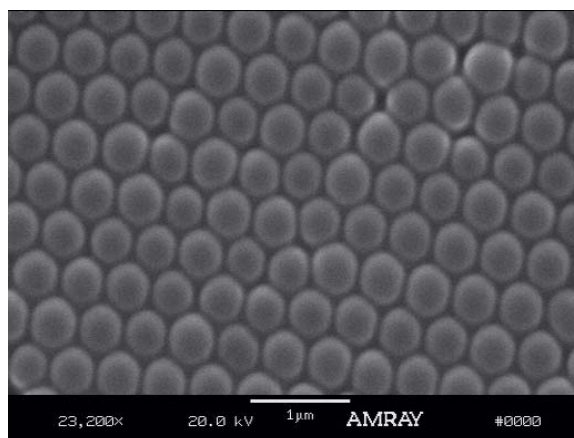
(a)



Multi layer

Mono layer

(b)



(c)

**Figure 6.2. (a) Set Up of Monolayer Spherical Nano Particle Deposition; (b) Microscope View of Monolayer Silica Spherical Particle on Silicon Substrate (0.05% DI Water Suspension, 200x); (c) SEM Image of Monolayer Deposited Spherical Particles on Substrate.**

Furthermore, Bangar *et al.* [138] and Nocke *et al.* [139] demonstrated the dielectrophoretic alignment method for the alignment of Ppy nanowire and polymer compounds, respectively. Yan *et al.* [140] successfully fabricated silica nanowire arrays through a self-supplied vapor-liquid-solid (VLS) mechanism by a sandwich-like structure and gas-flow. In this study, we consider the electric field method for the alignment of cylindrical particles since it is simple and low cost, and only an AC power supply and two electrodes are needed to provide the electric field.

### 6.2.3. Experimental Results and Discussion

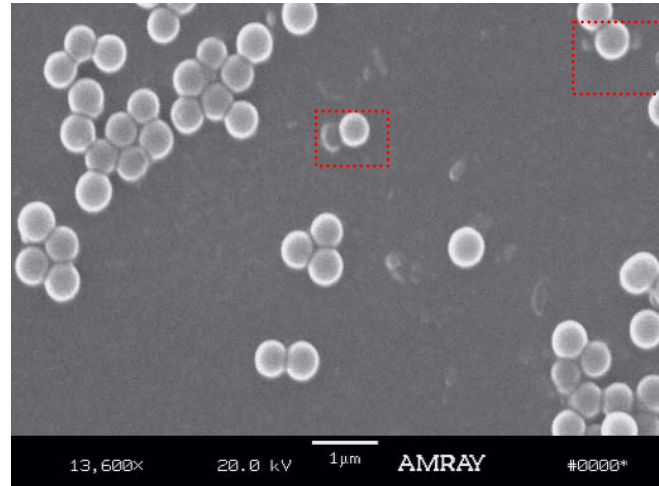
Firstly, we have demonstrated the nano-hole fabrication results with spherical particles on the substrates. After the monolayer deposition of the spherical silica particles, we used the Ti:sapphire USP laser to irradiate the particles on the substrate with area scanning. The laser parameters used include 810 nm wavelength, 100 fs pulse width and 10 nJ pulse energy. The focus lens has focal length of 5 mm and the diffraction limit spot size is 9.4  $\mu\text{m}$ . The laser beam was focused on the top surface of the spherical particles. We used multiple line scanning ablations with 3  $\mu\text{m}$  space between two lines to form an area scan so that the target area with monolayer particle deposition can be irradiated. The stage moving speed is 5 mm/s and the whole area was scanned only once.

After irradiation the samples were put in ultra-sonic bath for 30 minutes to remove the remaining particles, and put on hot plate to dry for 10 minutes and then the samples were checked for the substrate morphology with SEM. The nano-holes can be observed on PDMS substrate and silicon substrate, as shown in Fig. 6.3(a) & (b)

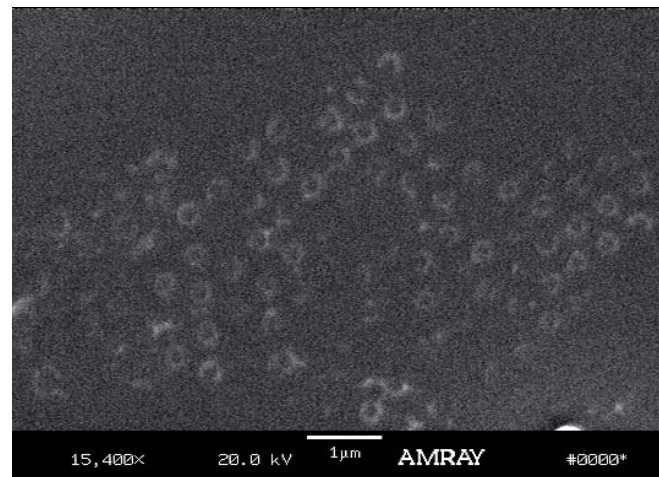
respectively. And as shown in Fig. 6.3(b), the nano-hole array is in the same hexagon shape as the deposited spherical particles before the irradiation. The size of the nano-holes are about 268 nm which is about half of the diameter of the spherical particle.

For nano-line fabrication, we firstly used multi-wall CNT as the cylindrical particle, and the diameter of the CNT is about 110 - 170 nm and the length is about 5 - 9  $\mu\text{m}$ . Firstly, we tried to use the same method as spherical silica particles to obtain single isolated cylindrical particle deposition on substrates. The isolated CNT particles were randomly distributed on a specific area of the silicon substrate and monolayer particles can be seen on the silicon substrate, as shown in Fig 6.4(a).

The monolayer CNT particle deposited area has been irradiated with Ti:sapphire laser at 810 nm wavelength with area scanning (5 mm/s stage moving speed). Before the experiment, the silicon substrate was adjusted so that it is perpendicular to the laser beam. The particles on the substrates were put in the focus position and during the experiment, occasional white sparking can be seen when the laser was scanning in the CNT deposition area because of burning of the CNT particles in ambient air. The target area with monolayer particle deposition was irradiated by area scanning with 3  $\mu\text{m}$  space between two lines. After irradiation, the samples were cleaned with ultra sonic bath for one and half hours. Then the substrate surfaces were checked by SEM. As shown in Fig. 6.4(b), we did observe the nano line segment feature on the silicon substrate after irradiation. But the repeatability of the experiment is not good for this nano line results.



(a)

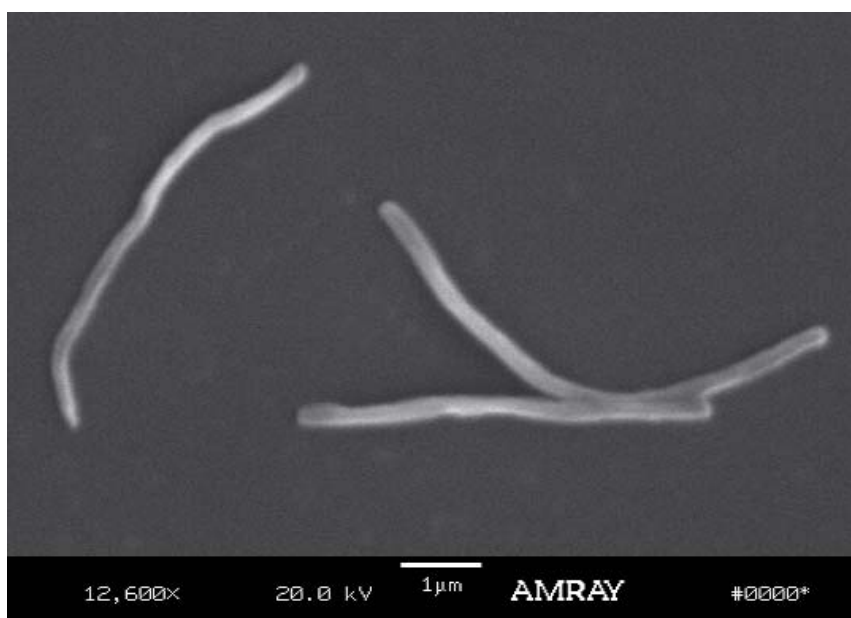


(b)

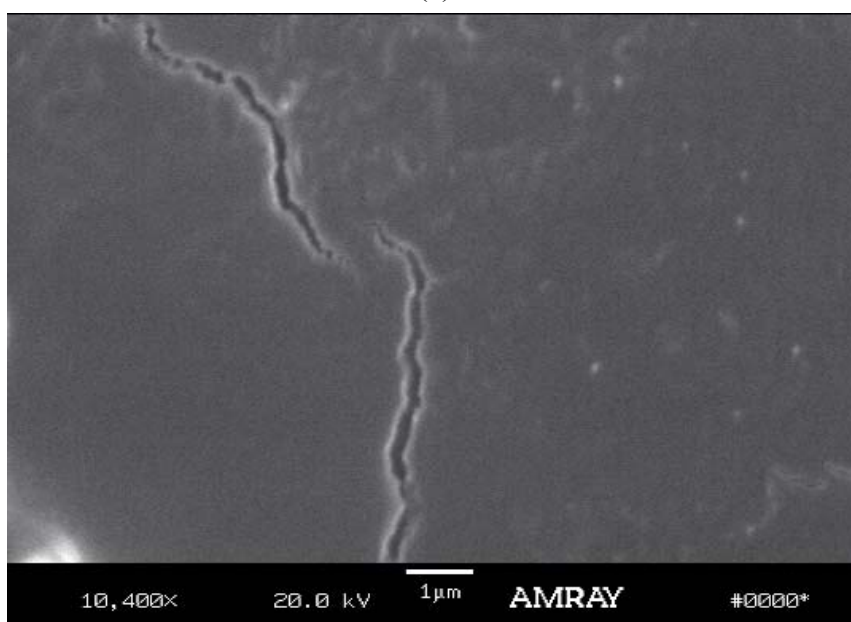
**Figure 6.3. (a) PDMS Substrate with Nano Holes after Irradiation; (b) Silicon Substrate with Nano Holes after Irradiation and Particle Removal.**

Because of the burning of the CNT particles, another cylindrical particle - silica fiber nano rod has been used for nano line fabrication. The silica fiber nano rod can be fabricated by pulling the optical fiber core together with oxy-hydrogen flame (2400 K) heating beneath the fiber after removing the cladding of the fiber. Usually the stretched fiber rod diameter reduced to several hundred of nanometers.





(a)



(b)

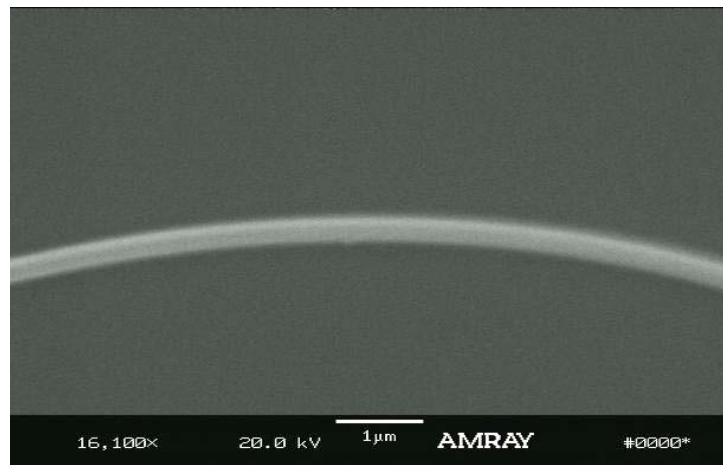
**Figure 6.4. (a) CNT on Silicon Substrate; (b) Nano Line Feature on Silicon Substrate.**

The first step desired is to demonstrate the feasibility of nano line fabrication with a single isolated cylindrical particle on the substrate. At first, a single silica nano rod with 1 - 5 mm length and less than 1 μm diameter was successfully deposited on the silicon

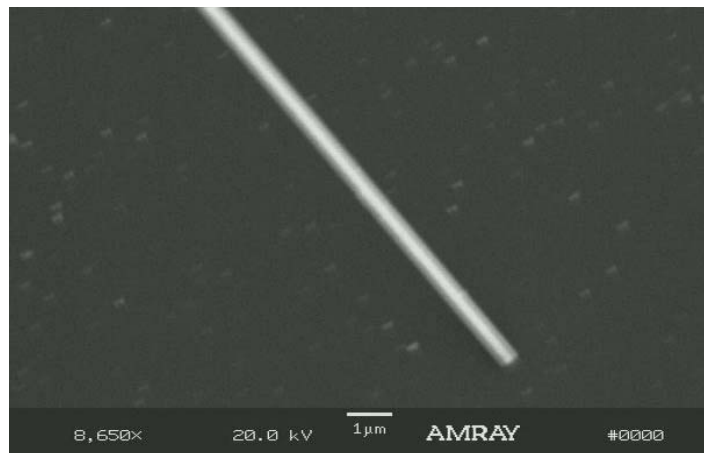
substrate, as shown in Fig. 6.5. Then the silica nano rod was irradiated with femtosecond laser pulses with multi-line scanning. The scanning lines were perpendicular to the outstretched direction of the rod to ensure part of the rod length was covered during the area scanning and there is 50  $\mu\text{m}$  space between two lines and the stage moving speed was 5 mm/s. The focus position was on the nano rod as well. After experiments, we removed the nano rod and checked the substrate underneath the rod for the scanned area underneath the nano rod. Since we have marked the area around the fib tip so that we can know the line ablation trace and by tracking the scanning lines we can know where the scanned fiber covered area is and check whether there is any ablation feature, such as line segments. So far, we have not succeeded to achieve nano line segment feature by using this method.

There are several possible reasons. The first one is that the laser irradiation direction is not scanning along the cylindrical particle outstretched direction. To better demonstrate the feasibility of nano line fabrication by using single cylindrical particle on the substrate. Precise control may be needed to let the laser focal spot follow the nano rod outstretched direction and a full length scanning is a better way to generate the nano line features; Secondly, the laser focus position is critical for the enhancement factor and the current experimental set up (lens and stage) is not accurate enough for the focus position control and measurement, especially when the laser beam is scanning over the rod; Finally, the laser energy level is a low (10 nJ pulse energy). Using higher pulse energy can enhance the possibility of exceeding the ablation threshold although the enhancement of laser intensity has reduced the ablation threshold.

After the demonstration of nano line fabrication with single cylindrical particle on substrate, we can further study the influence of various laser parameters and conditions for nano line fabrication. This includes laser beam focus position, cylindrical particle size, laser wavelength and laser fluence. We can check the differences for the fabricated nano line features including different line widths and depths to get the relationship between the laser parameters and the nano features, respectively.



(a)



(b)

**Figure 6.5. (a) Silica Nano Rod on Silicon Substrate (260 nm diameter); (b) Another Silica Nano Rod on Silicon Substrate (500 nm diameter).**

(a) Laser beam focus position

With different laser beam focusing position, the enhancement factor in the near-field region is different as demonstrated for single silica micro-sphere particle on substrate by Cai *et al.* [141]. So for cylindrical particle, the shift of laser beam position laterally or axially will also induce the enhancement factor change in the near-field region and the fabricated feature (line width and depth) will also be changed.

And the laser beam irradiation angle is also important to the fabrication process. There are two possible angles: perpendicular to the substrate ( $90^\circ$ ) or parallel to the substrate. It is desirable to investigate the impact of the irradiation angle for the fabrication for future experiment.

(b) Cylindrical particle size

Since the cylindrical particle size fabricated can vary from 100 nm to 1  $\mu\text{m}$  or even larger, the influence of cylindrical particle size on the nano feature fabricated can be studied by using different particle size. As demonstrated by Huang *et al.* [130], Sakai *et al.* [131] and Zhou *et al.* [142], the intensity distribution in the near-field region with different particle sizes is different by calculation and experiment for spherical particles.

(c) Laser wavelength and pulse duration

Like the particle size, the laser wavelength can be adjusted to study the relation between the enhancement factor and the wavelength. The Ti:sapphire laser wavelength range is 710 - 980 nm. Besides, the pulse duration can be also adjusted (50 - 80 fs), these different conditions can be summarized for the influence of the near-field fabrication.

(d) Laser fluence

The pulse energy can not be adjusted for the current laser system. But with additional amplifier or attenuator later, the effect of laser fluence for the nano line feature can be also studied.

(e) Substrate materials

Two kinds of substrate materials will be used for the fabrication - polymer (PDMS) and silicon. PDMS is one of the common materials for the fabrication of micro-fluidic system and its property is stable and PDMS will be the primary material for the nano-fabrication study.

After these parametrical studies for the nano fabrication, we can demonstrate the feasibility of parallel large volume fabrication of continuous nano line features. With good alignment of cylindrical particles, we can demonstrate parallel large area nano line fabrication on substrates with designed pattern.

## 6.3. Simulation

### 6.3.1. Introduction

Meanwhile, it is desired to know the optical field distribution in the near-field region along the light propagation direction to optimize the experimental conditions under which the enhancement can be maximized or the smallest nanostructures could be achieved.

For the near-field enhancement calculation and simulation, different algorithms, including the Finite-Different-Time-Domain (FDTD) method, the Discrete Dipole Approximation (DDA) method, the Multiple Multipole (MMP) method, the Finite Element method (FEM), and the Modified Long Wavelength Approximation (MLWA) method, have been developed to calculate the field distribution underneath the tip or around nano particles when illuminated by lasers.

Yi *et al.* [125] conducted numerical simulations based upon the FDTD algorithm to study the spatial distribution of the enhanced optical field underneath the tip and the results show that the optical field can be more strongly enhanced with silicon substrate. Chimmalgi *et al.* [143] also used FDTD method to obtain the electric field intensity distribution underneath the tip and the simulation results confirmed the high spatial resolution observed experimentally and suggest that the enhanced electric field under the tip is the main mechanism for the nano-fabrication results. Bohn *et al.* [144] investigated the near field of an apertureless NSOM with the Multiple Multipole method to obtain

optical fields underneath the tip, and they found that if a certain geometric condition is satisfied, an enhancement factor of 250 can be achieved. Cai *et al.* [141] presented near field calculation using a generalized Lorentz-Mie scattering method and demonstrated that the consistence of local field enhancement between experimental results and numerical modeling. Micic *et al.* [145] studied the electric field distribution of an AFM tip using finite element method and found that the field enhancement changes only a factor of 2 when the nano-particle size changes from 10 to 80 nm and the laser beam propagation orientation angle is important to the field intensity enhancement.

Because of the presence of the substrate, the problem of calculating the electromagnetic field scattered for particle on substrate is not a simple one as isolated particles. Several theoretical approaches and simulation methods have been developed to solve this scattering problem, each one corresponding to a particular set of conditions affecting the problem. The simplest system, in which the microstructure is much smaller than the wavelength, can be modeled by a dipole. This approach is valid when the field with the particle is nearly constant and the particle is not too close to the interface. As the particle-substrate separation decreases, the dipole model begins to fail because higher order multi-poles become significant through particle-substrate interaction. Most simple models assume that the dipole is illuminated by the superposition of the direct and reflected plane waves. The total scattered field from the dipole is the superposition of the direct and image scattered fields. [146]

Initially researchers have considered particles whose shape conforms to regular

geometries such as a sphere, cylinder and spheroid. The Mie theory provides the exact analytical description of the behavior of the electric field surrounding isolated spherical nano-particles but is unfortunately strictly limited to the spherical geometry. It cannot be employed to irregularly shaped structures that are arbitrarily positioned in space. The analysis of such geometries requires numerical methods to solve Maxwell's equation in the computational domain via iterative procedures. Nahm and Wolfe [147] used a double interaction model to calculate the scattering by a sphere over a perfectly conducting mirror. In this model, the sphere is illuminated by the beam both directly and after specular reflection from the surface. Some researchers reduce the problem of light scattering by a sphere on a substrate to the problems of scattering by a sphere in a homogeneous medium and of the reflection of spherical waves by the substrate. They solve the first by using the Mie theory, whereas for the second one they use an extension of Weyl's method to calculate the reflection of dipole radiation by a flat surface. Videen expanded the interaction field about the image location to solve the scatter from a sphere in front of and behind a smooth arbitrary substrate [148], and later provided an exact theory for an arbitrary particle system in front of and behind a perfectly conducting substrate [149]. For non-perfectly conducting substrates, some numerical method or simplifying assumption must be used. Borghi *et al.* [150] presented a method for treating the two-dimensional scattering of a plane wave as an arbitrary configuration of perfectly conducting circular cylinders in front of a plane surface with general reflection properties.

Much research on the problem of the scattering by substrates has been formulated in terms of exact integral equations for the electromagnetic fields that are solved by



standard numerical methods [146]. It should be stressed that the formulation is exact in the sense that no additional physical assumptions or approximations are needed. Integral equations are derived from integral theorems that combine differential Maxwell equations and appropriate boundary conditions. One of the methods most widely used is the extinction theorem (ET) of physical optics [151, 152] which produces a surface integral equation relating both the incident field to the sources on the surface, and these to the scattered fields. Although the ET method was initially used to calculate the scattering by random rough surfaces, different authors have extended it to calculate the near-field scattering by small metallic particles on flat conducting substrates. The exact character of the formulation takes into account multiple interactions between particle and substrate. This improvement allows numerical simulation of the scattering from systems composed of surfaces belonging to separated bodies of arbitrary shape and with different optical properties.

Many other approaches to the problem of scattering from particles on surfaces can be found in the literature. One simple approach among them is the ray-tracing solution. From a geometrical viewpoint, a plane wave incident on a metallic object is a beam of parallel rays of uniform density that is reflected by the sphere-substrate system. The scattered field is obtained as the coherent sum of the group of rays emerging from the surface with a common angle.

### 6.3.2. Mathematical Formulation

The problem of electromagnetic analysis on a macroscopic level is the problem of solving Maxwell's equations subject to certain boundary conditions. Maxwell's equations are a set of equations, written in differential or integral form, stating the relationships between the fundamental electromagnetic quantities. These quantities are the electric field intensity  $\hat{E}$ , the electric displacement or electric flux density  $\hat{D}$ , the magnetic field intensity  $\hat{H}$ , the magnetic flux density  $\hat{B}$ , the current density  $J$  and the electric charge density  $\rho$ .

The equations can be formulated in differential or integral form. The differential forms are presented here, because it leads to differential equations that the finite element method can handle. For general time-varying fields, Maxwell's equations can be written as

$$\nabla \times \hat{H} = J + \frac{\partial \hat{D}}{\partial t} \quad (6.1)$$

$$\nabla \times \hat{E} = -\frac{\partial \hat{B}}{\partial t} \quad (6.2)$$

$$\nabla \cdot \hat{D} = \rho \quad (6.3)$$

$$\nabla \cdot \hat{B} = 0 \quad (6.4)$$

The first two equations are also referred to as Maxwell-Ampère's law and Faraday's law, respectively. Equation three and four are two forms of Gauss' law, the

electric and magnetic form, respectively. Another fundamental equation is the equation of continuity, which can be written as

$$\nabla \cdot \mathbf{J} = -\frac{\partial \rho}{\partial t} \quad (6.5)$$

Out of the five equations mentioned, only three are independent. The first two combined with either the electric form of Gauss' law or the equation of continuity form such an independent system.

For dielectric and isotropic media,  $\rho = 0$ ,  $\mathbf{J} = 0$ , and the two constitutive relationships are as follows:

$$\hat{\mathbf{D}} = \epsilon \hat{\mathbf{E}} \quad \text{and} \quad \hat{\mathbf{B}} = \mu \hat{\mathbf{H}} \quad (6.6)$$

where  $\epsilon = \epsilon_r \epsilon_0$  and  $\mu = \mu_r \mu_0$ ,  $\epsilon_0$  and  $\mu_0$  are the permittivity and permeability of vacuum as well as  $\epsilon_r$  and  $\mu_r$  are the material's relative permittivity and relative permeability respectively.

The equation only of  $\hat{\mathbf{E}}$  can be obtained after taking the curl operation to Eq. (6.2)

$$\nabla \times (\nabla \times \hat{\mathbf{E}}) + \frac{\partial}{\partial t} (\nabla \times \hat{\mathbf{B}}) = 0 \quad (6.7)$$

Thus, using the vector operation and Eqs. (6.1), (6.3) and (6.6), we obtain the wave equation of

$$\nabla^2 \hat{E} = \mu\epsilon \frac{\partial \hat{E}}{\partial t} \quad (6.8)$$

We set the function  $\hat{E}$  has harmonic solution

$$\hat{E} = \bar{E} e^{j\omega t} \quad (6.9)$$

With Eq. (6.6), we can derive the equation for  $\bar{E}$  as follows:

$$\nabla^2 \hat{E} - \mu\sigma \frac{\partial \bar{E}}{\partial t} - \mu\epsilon \frac{\partial^2 \bar{E}}{\partial t^2} = 0 \quad (6.10)$$

where  $\sigma$  is the electrical conductivity. We can transfer the above equation to the form of a time-harmonic wave by setting  $\bar{E}(\bar{r}, t) = \bar{E}_0(\bar{r})e^{i\omega t}$ . The coupled set of Maxwell's equations can be reduced to a simple form:

$$\frac{1}{\mu} \nabla^2 \bar{E} + \omega^2 \epsilon_c \bar{E} = 0 \quad (6.11)$$

where we have introduced the complex permittivity  $\epsilon_c = \epsilon - i(\sigma / \omega) = \epsilon_{rc} \epsilon_0$  and  $\omega = 2\pi c / \lambda$ ; and  $c$  is the speed of light in the medium and  $\lambda$  is the light wavelength. Here, the complex index of refraction,  $m = n - ik$ , is conveniently introduced for the treatment of wave propagation;  $n$  is the real part of the refractive index and represents a

spatial phase change of the electromagnetic wave;  $k$  is the imaginary part of the refractive index (absorption index) and stands for a spatial damping on the electromagnetic wave. The relationship between  $\varepsilon_{rc}$  and  $m$  is expressed by

$$\varepsilon_{rc} = m^2 = n^2 - k^2 - i2nk \quad (6.12)$$

### 6.3.3. Interface and Boundary Conditions

To get a full description of an electromagnetic problem, we also need to specify boundary conditions at material interfaces and physical boundaries. A valid solution to the field equations will automatically result in these conditions being satisfied. For no surface current present at interfaces between two media, the boundary conditions can be expressed mathematically as

$$n_2 \times (E_1 - E_2) = 0 \quad (6.13)$$

$$n_2 \cdot (H_1 - H_2) = 0 \quad (6.14)$$

where  $n_2$  is the outward normal from medium 2. In fact, the exact condition formulas are dependent on which field you are going to solve.

One of the great challenges in finite element modeling is how to treat open boundaries in radiation problems. The COMSOL Module offers two closely related types of absorbing boundary conditions, the scattering boundary condition and the matched boundary condition. The former is perfectly absorbing for a plane wave, whereas the

latter is perfectly absorbing for guided modes, provided that the correct value of the propagation constant is supplied. However, in many scattering and antenna modeling problems, it is hard to describe the incident radiation as a plane wave with a well known direction of propagation. In such situations, we can consider the use of perfectly matched layers (PML). A PML is strictly speaking not a boundary condition but an additional domain that absorbs the incident radiation without producing reflections. It provides good performance for a wide range of incidence angles and is not very sensitive to the shape of the wave fronts. The PML formulation can be deduced from Maxwell's equations by introducing a complex-valued coordinate transformation under the additional requirement that the wave impedance should remain unaffected

For the boundary conditions in this simulation, PML is introduced in the domain representing absorbing layers. In the corners the PMLs absorb the waves in both the x and y directions; on the sides, only the waves propagating in x direction are absorbed and on the top and bottom the waves propagating in the y direction are absorbed. Using the absorbing boundary condition at the outer boundaries of the PML regions improves the efficiency of the PMLs. As a result, use the scattering boundary condition on all outer boundaries. Continuity boundary conditions are used for the particle/substrate interface. The incident electric field is used to specify the incident laser beam with a Gaussian distribution and is defined as  $E_0 * \exp(-y^2 / r^2)$ , where  $E_0$  is the maximum value and  $r$  is the focused beam radius.

#### 6.3.4. Simulation Method

The involved near-field can be described by Maxwell's electromagnetic theory. As described in the previous literature review, a variety of numerical methods were considered for modeling the near-field enhancement effect. The FDTD method is frequently used to simulate all wave effects including propagation, scattering, diffraction, reflection and polarization. It also can be used to model material anisotropy, dispersion, and nonlinearities. In comparison, this approach includes the electromagnetic field effects on nano-particles by considering the optical penetration to the metal surfaces which will affect all the wave properties such as near field, far field, scattering and diffraction. The FDTD method solves the time-dependent Maxwell's equations to calculate electromagnetic scattering in both time and space domain. Maxwell's equations contain space and time derivatives of electric and magnetic fields. These derivatives are approximated by a finite difference scheme and discretized in both space and time domains. This method is popular because of its conceptual simplicity and ease of implementation. But it has drawbacks, such as the staircase approximation in the treatment of irregular configurations, the time consuming for stationary solutions and the large memory requirement.

FEM is another numerical method to solve the time-domain Maxwell's equations. As compared with the FDTD method, FEM has advantages in the near-field simulations, such as meshing method for complicated geometric shapes, controllable for mesh size for different sites, and the memory usage is saved and shorter running time. So we adopt the FEM to solve the Maxwell's equations for the propagation of electromagnetic field and

the radiation energy transport in the domain system.

In order to provide guidance for the experiment and understand the mechanism, studies over a broad range of laser parameters, particle sizes and materials have been conducted. The electric field in the near-field region between the particle and the substrate will be obtained and compared for different cases.

### **6.3.5. Simulation Models**

We will focus on the simulation of cylindrical particles on substrate to study the near-field enhancement with different laser parameters and conditions. For the field enhancement by cylindrical particles, the conditions include the particle material, the laser beam properties (wavelength, pulse duration, pulse energy and incident angle) and the substrate materials (polymer or silicon). And by simulation we can firstly optimize the experimental conditions under which the enhancement can be maximized or the smallest nanostructures could be achieved. And then we can also compare the experimental results with the simulation results for further reference and fabrication process.

The simulations were carried out with the commercial software package COMSOL, which is a powerful interface environment for modeling and solving all kinds of scientific and engineering problems based on partial differential equations. The partial differential equations are solved by using FEM. An important strength of COMSOL is the adaptive mesh and can refine the region of special interest, while FDTD method uses



equally space meshes. This adaptive mesh functionality makes the computation much more efficient and reduces the processing time.

Because of the huge computational resources required for the 3D simulation of spherical particles on substrate, a 2D model is considered since the cylindrical particle is located on the same plane as the substrate. Fig. 6.6(a) shows the 2D model domain for the cylindrical particle on the substrate.

In the model, the in-plane TE wave is propagating from left to right through air. As shown in Fig. 6.6(a), the smaller circle indicates the cylindrical particle and the larger circle surrounding the particle is a defined interested region for finer mesh purpose. The rectangle region on the right of the circle is the PDMS substrate sub-domain. The initial domain size is totally  $7.2\ \mu\text{m}$  by  $6.0\ \mu\text{m}$ . The thickness of the substrate is constant ( $3.0\ \mu\text{m}$ ), and the PDMS domain is  $3.0\ \mu\text{m}$  thick and  $4.8\ \mu\text{m}$  wide. The center of the cylindrical particle is fixed in position  $(0.5, 0)$ . The distance from the left wave incident boundary to the center of the particle is constant ( $2.7\ \mu\text{m}$ ). The complex refractive index of the silica particle the PDMS substrate are set as:  $1.453-0.005*i$  and  $1.450-0.00006*i$  for  $800\ \text{nm}$  wavelength calculated from absorption coefficient [153].  $E_0$  is set as  $1\ \text{V/m}$  if not specified and  $r$  is set as  $1.25\ \mu\text{m}$ .

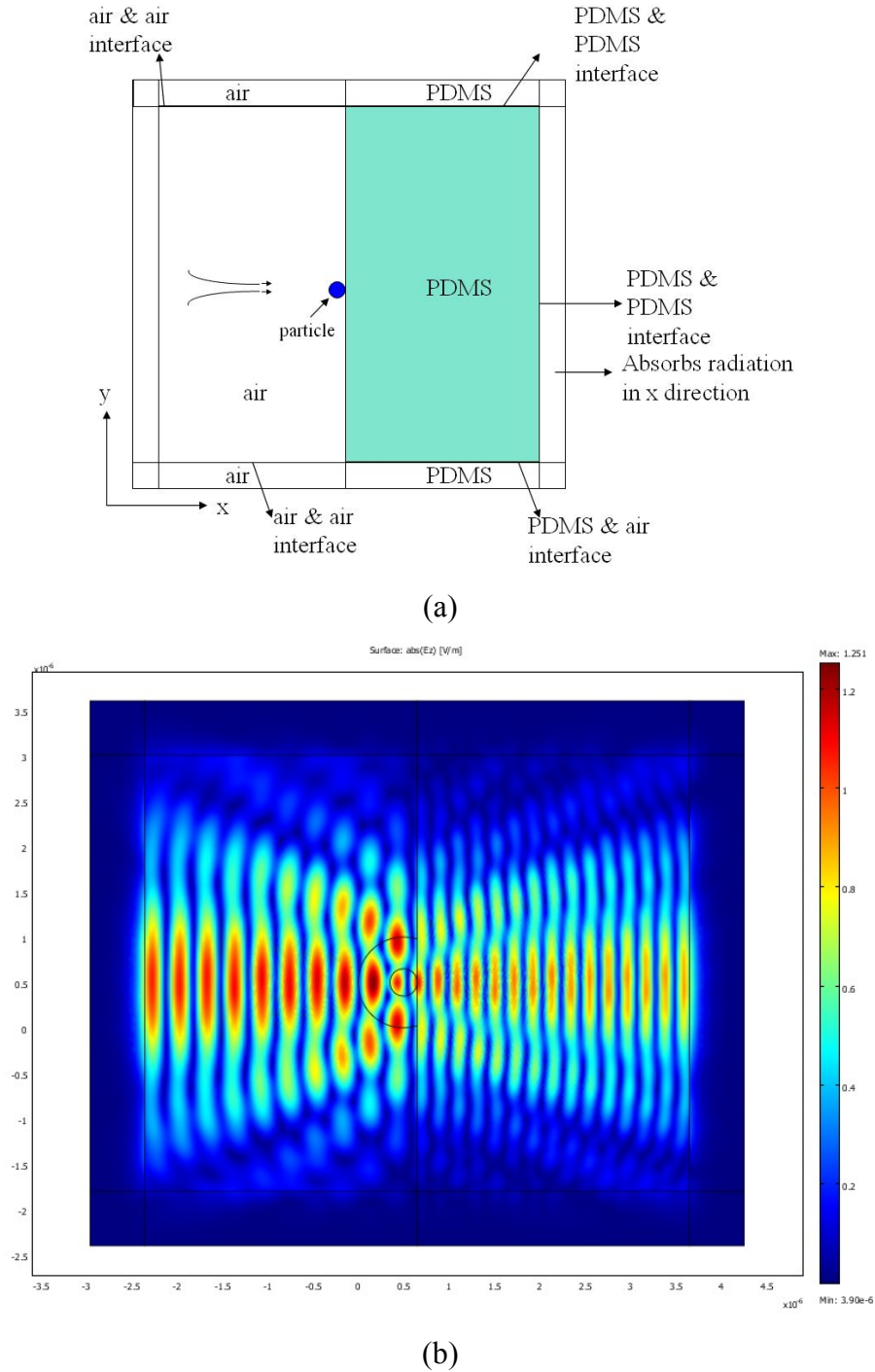


**Figure 6.6. (a) 2D model Domain for COMSOL Simulation Calculation; (c) A Typical Solution of Electric Field Distribution for the Whole Domain (Rod Diameter: 300nm, Wavelength: 600 nm).**

### 6.3.6. Results and Discussion

The mesh size for the important area is at least 1/8 of wavelength. After the

maximum finite element mesh sizes are carefully set, the electric field distribution for the whole domain can be solved rigorously. Fig. 6.6(b) shows a typical solution of a cylindrical particle with 300 nm diameter on PDMS substrate with no gap between them, respectively. After obtaining the electric field for the near-field region, we can get the intensity distribution and calculate the enhancement factor.

#### **6.3.6.1. Model Verification and Comparison**

For the model verification, firstly we need to verify that the computation algorithm can always lead to the same results for a specific case with finer mesh size or step increase time. For example, we can use the 500 nm cylindrical rod size with 0 nm gap on the PDMS substrate and choose different mesh size (7261, 33368 and 72023 nodes) to see the difference of the resulting electric field distribution. It is observed that the distributions of the electric field for the three different computational domains are similar. Meanwhile we can also choose the different time step for the solution. The results also look almost same for different time steps.

Another factor that should be considered in this model also include the PDMS domain size (length and width), because it will influence the reflection portion between air & PDMS interface in the bottom and two sides. And different domain sizes should be selected to see whether there is any influence for the scattering result.

Firstly, we have used the same particle size and different domain size of PDMS to see whether there is any difference for the electric field distribution. For different PDMS

domain width, we have the following comparison results. We have studied different domain thickness from 3.0 - 25  $\mu\text{m}$ . There is no obvious difference for different PDMS domain width, and the width almost has no influence. We have also studied the influence for different Gaussian beam incident position. We have chosen to increase distance from the incident plane to the substrate from 2.95  $\mu\text{m}$  to 3.55  $\mu\text{m}$ , 4.15  $\mu\text{m}$ , 4.75  $\mu\text{m}$  and 5.35  $\mu\text{m}$ . And check the absolute scattered electric field distribution.

Furthermore, the model has been compared with analytical or simulation results from other methods. Valle *et al.* [151] calculated the exact electromagnetic components of the near-field wave scattered from a subwavelength metallic cylindrical protuberance on a conducting substrate by applying the extinction theorem. The scattering geometry used in this research is similar to the model in this study. The cylinder and substrate are assumed to be made of the same material - gold, the wavelength is 600 nm, S (perpendicular) or P (parallel)-incident waves were used for comparison and the y component of the electric field of the scattered wave in the near field as a function of x for different z has been plotted, as shown in Fig. 6.7.

For the model in this study, the same parameters were used to compare the electric field distribution results. The parameters we used in COMSOL model include: Gaussian beam radius - 4.8  $\mu\text{m}$ ; incident beam wavelength - 600 nm; cylindrical rod diameter - 300 nm; After obtaining the solution, we have checked the component of the electric field of the scattered wave in the near field as a function of x for different z, as plotted in Fig. 6.8.

We can see the damping trend looks very nice compared with previous results. And the damping frequency is same as the result in the reference (four peaks for  $4\lambda$ , totally 16 peaks), but for  $y=0.25\lambda$  the magnitude is only half of it especially for the first several peaks.

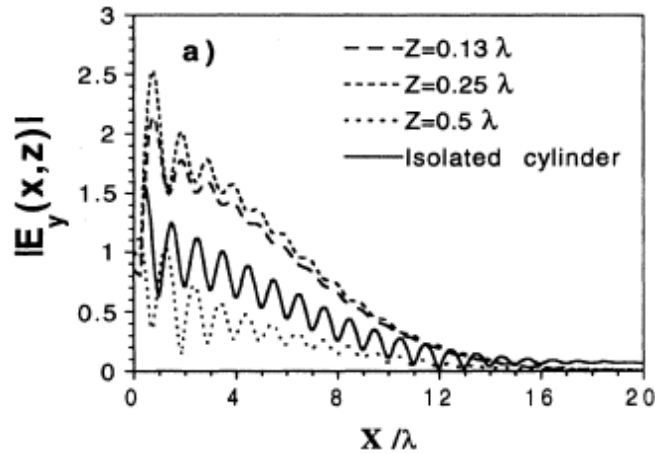
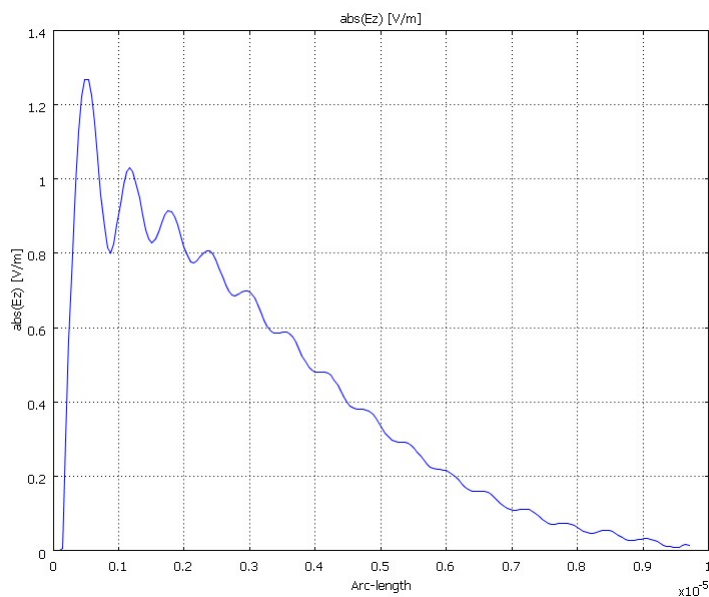


Figure 6.7. y component of the electric field of the scattered wave in the near field as a function of x for different z (S-incident) [151]

### 6.3.6.2. Influence of Different Parameters

The configurations in the 2D model like the cylindrical particle size, the gap between the particle and the substrate, the wavelength propagating in the domain and the particle and substrate material type certainly affect the intensity enhancement in the near-field region. To investigate the parametric influences, we can obtain the enhancement factor in the near-field region with varying propagating frequency for different cylindrical particle sizes, gap distances, and different material properties, respectively.



**Figure 6.8. Z component of the electric field of the scattered wave in the near field as a function of x for  $y=0.25$  by COMSOL (gold on gold substrate)**

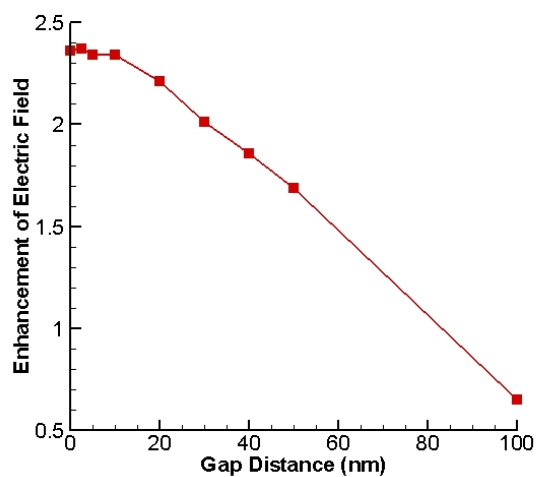


**Figure 6.9. Enhancement Factor for the Center Point Right on Surface of Substrate with 100 nm Rod Diameter (Gap Distance Changes from 0 to 100 nm).**

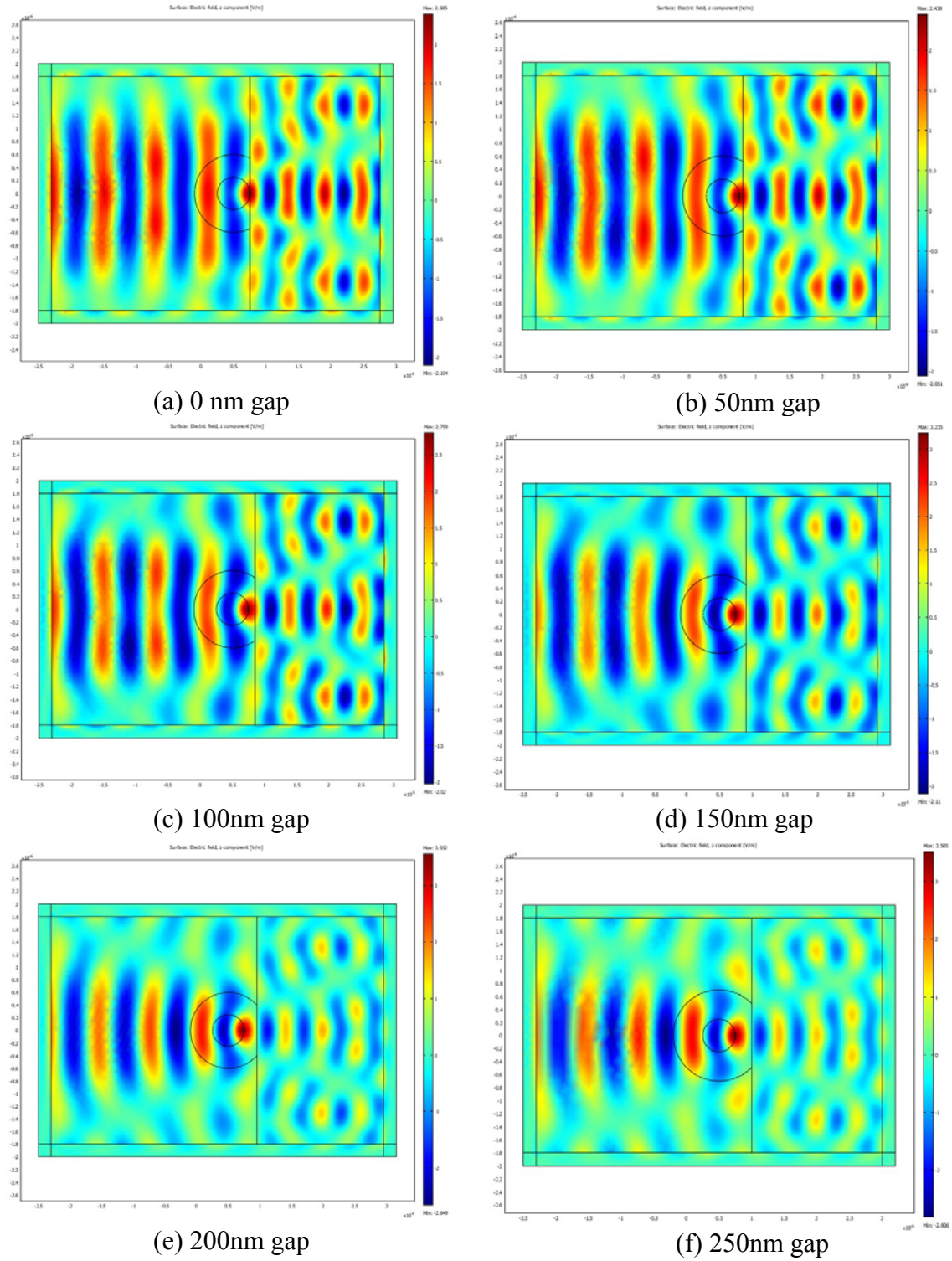


**Figure 6.10. Solution of Silica Cylinder on PDMS Substrate with Different Gaps (Gaussian Beam with 2 v/m Maximum Electric Field for Incident Wave,  $D=500$  nm).**

Figure 6.9 shows the change of enhancement factor of electric field with different gap distance and the cylindrical particle size is 100 nm. And we can see, with the increasing of the gap between the particle and the substrate, the enhancement factor is decreasing and the maximum enhancement factor is about 2.38.

Moreover, we can choose different rod sizes and different gaps to study the change of the enhancement factor of electric field so that we can obtain the relationship between the enhancement factor and the rod size and gap. Figure 6.10 shows a group of representative results of silica cylindrical particle on PDMS substrate with different gaps (0-250 nm) with particle diameter of 500 nm. The maximum electric field for the Gaussian beam distribution is 2 V/m for incident wave, and the wavelength is 800 nm. And we can see from Fig 6.10, the maximum enhancement factor is found as 3.46 for 200 nm gap between the particle and the substrate. Figure 6.11 shows the maximum enhancement factors in the gap with different gap distance for different rod diameters (100-500 nm). Figure 6.12 shows the maximum enhancement factors in the gap with different rod diameters (0-400 nm gap distance).



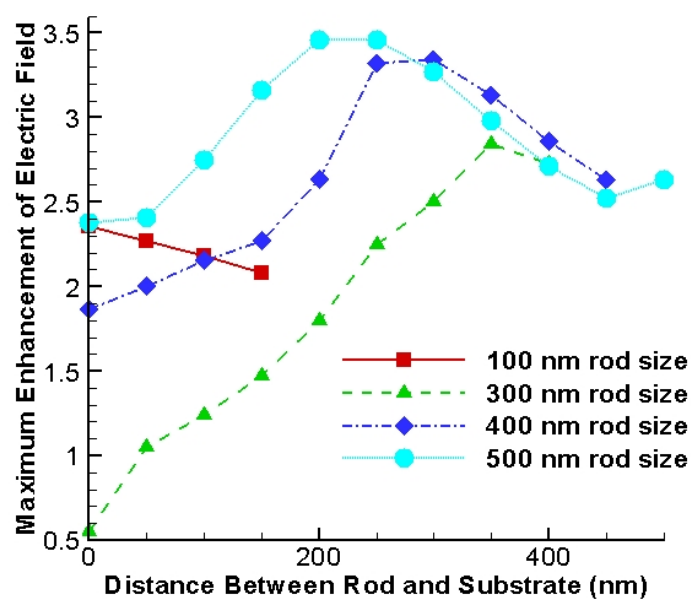


Figure 6.11. Maximum Enhancement Factors in the Gap with Different Gap Distance (100-500 nm Rod Diameters)

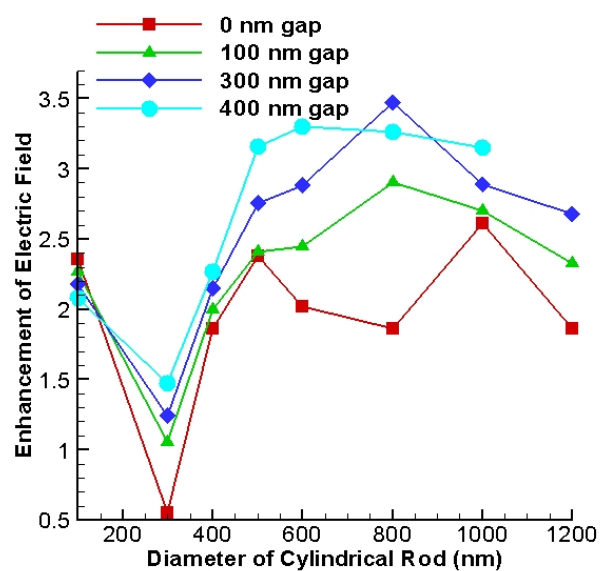


Figure 6.12. Maximum Enhancement Factors in the Gap with Different Rod Diameters (0-400 nm Gap Distance)

### **6.3.6.3. Comparison with Experiment Results**

With the simulation results for different parametric cases, we can obtain the basic relationships between the enhancement factor and different particle sizes, gap distances, propagating wavelength and materials, respectively. And this can give us guidance for the experiment to obtain the maximum enhancement factor. And for the experiment results, we can also compare the resulted nano line feature properties (width & depth) with the simulation for future reference of nano-fabrication. This part will be one portion of the future work.

## **6.4. Summary**

This project has addressed a systematic analytical, numerical and experimental study of the near-field enhancement properties between nano spherical/cylindrical particles and substrates. Nano-hole array with about 268 nm which is about half of the diameter of the spherical particle has been fabricated on PDMS and silicon substrates via the near-field enhancement effect. The diffraction limit of light has been circumvented by using nano cylindrical particles assisted near-field fabrication. And this gives potential applications of parallel large volume nano line fabrication on different substrates for nano devices, ultra-sensitive sensors and high-volume data storage, because this method is simple, precise and low cost.

To investigate the near-field effect phenomena in detail, simulation models based on Maxwell's equations and finite element method were introduced to investigate different parametric cases - particle sizes, gap distances, wavelength and material

properties. This simulation work analyzed the mechanism (field intensity distribution) and influence of laser conditions and particle size for the nano feature fabrication, and provided a solid foundation and guidance for the experiment work. Nano line fabrication with single particle on substrate was firstly studied by experiment and the generated feature sizes were summarized for fabrication purpose. Finally, with proper method of cylindrical particle deposition, we can further demonstrate parallel fabrication of nano line which is a very attractive and promising method for large volume nano-fabrication. The study provides an effective method for nano line fabrication, in particular for parallel large volume fabrication. And it also provides a clear understanding of the physical basis to achieve more efficient and precise laser nano-fabrication with nano particles.

## Chapter 7.

### Conclusions and Future Work

#### ***7.1. Conclusions***

This dissertation has addressed a systematic experimental investigation of the USP laser ablation of polymer material and human skin tissue materials, especially for the potential applications of the USP laser micro-fabrication of polymer, micro-processing of tissue including separation, cut and stripping and nano-fabrication via monolayer nano particles. For polymer ablation study, the ablation thresholds for single spot and single line scanning ablation were both determined and the two results are coincident with each other very well. It shows that both methods can be used to determine the ablation threshold. The ablation threshold reduces with increasing pulses due to the accumulation effect and the incubation factor was also determined. The ablation line width, internal ablation interface depth, and ablation surface quality with different pulse overlap rate and irradiation pulse energy were completely conducted. A parametric study was used to obtain a proper range of laser parameters for PDMS separation. Based on it, thin layer PDMS separation was completed and a multi-width micro-channel interconnected network by USP laser internal ablation was also demonstrated.

To investigate real human tissue (dermis) ablation and separation, single line surface scanning ablation was used and SEM was used to character the ablation features

such as ablation line width and depth. Ablation threshold and incubation factor were also determined. Histological examinations were performed to find proper laser parameters for tissue micro-processing with minimal thermal damage. With the proper pulse overlap rate and pulse energy, the thermal damage zone can be less than 5  $\mu\text{m}$  which is very small compared with CW or long-pulsed laser processing. Both *in vitro* wet tissue separation and freeze-dried tissue stripping were demonstrated by the USP laser ablation with different experimental set up design and mechanism. No sign of visible thermal damage was found for both types of tissue after processing. The cohesion and morphology of the separated tissue layers were not altered and the freeze-dried dermis could be re-hydrated to the original status for future usage.

Furthermore, an analytical solution is developed to analyze the temperature distributions and heat effected zones in materials. We have theoretically analyzed the relationships between thermal effect and laser parameters based on several assumptions and a simplified 1-D physical model in cylindrical coordinates was established to solve the non-homogeneous heat conduction problem in the thermal heating processing. An analytical formulation was given to describe the temperature increase in the studied domain which considers all the laser parameters used, and the thermal damage zone criteria was also defined and compare with real experiment with different laser parameters. Both results show that the thermal damage can be confined in a small zone with proper pulse energy and overlap rate. The significant effect of two key factors - pulse energy and pulse overlap rate were specifically discussed with relation to the thermal damage zone by parametric studies. This provides a method for how to obtain the

relationship between laser parameters (pulse energy, repetition rate and pulse overlap rate) and thermal damage zone size, and guidance of selecting proper ranges of laser parameters used for larger material volume removal with minimal thermal damage.

Finally, monolayer nano particles based near-field nano-fabrication by USP laser has been developed. The monolayer spherical silica particle has been successfully dispersed on different substrates and nano-holes were generated after laser irradiation on silicon and polymer substrates. Then CNT and nano fiber rod have been deposited and studied for nano line fabrication. To investigate the near-field enhancement phenomena, simulation models based on Maxwell's equations and the finite element method were introduced to investigate different nano rod size, materials properties, and laser parameters. Influence of various laser parameters and conditions for the intensity enhancement in the near-field region has been studied. The gap effects were emphasized and studied in detail to find an optimal gap for maximum intensity enhancement. Initial experiments were conducted on the silicon and PDMS substrates and the USP Ti:sapphire laser was used to do the fabrication. We did not obtain enough experimental results to compare and support the simulation results. However, the theoretical and numerical work provides a solid foundation of this near-field nano-fabrication.

## **7.2. Future Work**

For the tissue separation and micro-processing, the thermal damage investigation and analysis can be applied to many other materials, such as hard tissues and other dielectric materials. In future study, the formulation including all the laser parameters –

pulse energy, repetition rate, stage moving speed, focal spot size and tissue properties can be summarized to provide a criteria for thermal damage zone characterization for USP laser ablation. Furthermore, the proposed analysis can provide solutions for cases with temperature dependent heat generation due to the variation of optical properties such as absorptivity and transmissivity. Also, the solution can be extended to a three-dimensional analysis with use of a three-dimensional Green's function with consideration of the dynamic ablation processing, such as the temperature of the ablation volume, ablation width and depth change and phase change.

Another focus of future work should be devoted to the near-field nano-fabrication experiment and modeling, and it includes these parts:

- Further investigation of the theoretical models to better understand and reveal the properties of the near-field enhancement;
- Systematic studies of the simulation models to enrich the parametric study and provide guidance for experiments;
- Experimental studies of the nano particle assisted nano line fabrication on PDMS and other substrates;
- Further investigation of monolayer cylindrical particles distribution method for large area nano line fabrication and its potential tremendous applications

in other related field and industry.



## References

- [1] M. Schuler and A. Gertzman, "private communications," 2007.
- [2] B. D. DeBusschere, D. A. Borkholder, and G. T. A. Kovacs, "Design of an integrated silicon-PDMS cell cartridge," in *Solid State Sens. Actuators Conf.*, pp. 358-362, 1998.
- [3] X. Zhang, X. Jiang, and C. Sun, "Micro-stereolithography of polymeric and ceramic microstructures," *Sensors & Actuators: A. Physical*, vol. 77, no. 2, pp. 149-156, 1999.
- [4] H. Yoshimoto, Y. Shin, H. Terai, and J. Vacanti, "A biodegradable nanofiber scaffold by electrospinning and its potential for bone tissue engineering," *Biomaterials*, vol. 24, no. 12, pp. 2077-2082, 2003.
- [5] V. Kancharla and S. Chen, "Fabrication of biodegradable polymeric micro-devices using laser micromachining," *Biomedical Microdevices*, vol. 4, no. 2, pp. 105-109, 2002.
- [6] N. Bityurin, "Studies on laser ablation of polymers," *Annu. Rep. Prog. Chem., Sect. C*, vol. 101, p. 216-C247, 2005.
- [7] T. Lippert, "Laser application of polymers," *Advances in Polymer Science*, vol. 168, pp. 51-246, 2004.
- [8] P. Pronko, S. Dutta, J. Squier, J. Rudd, D. Du, and G. Mourou, "Machining of sub-micron holes using a femtosecond laser at 800 nm," *Optics communications*, vol. 114, no. 1-2, pp. 106-110, 1995.
- [9] C. Atwood, M. Ensiz, D. Greene, M. Griffith, L. Harwell, D. Reckaway, T. Romero, E. Schlienger, and J. Smugeresky, "Laser Engineered Net Shaping (LENS (TM)): A Tool for Direct Fabrication of Metal Parts," 1998.
- [10] P. Mannion, J. Magee, E. Coyne, and G. O'Connor, "Ablation thresholds in ultrafast laser micro-machining of common metals in air," *Proc. of SPIE*, vol. 4876, p. 470, 2003.
- [11] M. Niemz, E. Klancnik, and J. Bille, "Plasma-mediated ablation of corneal tissue at 1053 nm using a Nd: YLF oscillator/regenerative amplifier laser," *Laser Surg. Med.*, vol. 11, pp. 426-431, 1991.
- [12] J. Fischer, J. Dams, M. Götz, E. Kerker, F. Loesel, C. Messer, M. Niemz, N. Suhm, and J. Bille, "Plasma-mediated ablation of brain tissue with picosecond laser pulses," *Applied Physics B: Lasers and Optics*, vol. 58, no. 6, pp. 493-499, 1994.
- [13] J. Moss, B. Patel, G. Pearson, G. Arthur, and R. Lawes, "Krypton fluoride excimer laser ablation of tooth tissues: precision tissue machining," *Biomaterials*, vol. 15, no. 12, pp. 1013-1018, 1994.
- [14] F. Loesel, J. Fischer, M. Götz, C. Horvath, T. Juhasz, F. Noack, N. Suhm, and J. Bille, "Non-thermal ablation of neural tissue with femtosecond laser pulses," *Applied Physics B: Lasers and Optics*, vol. 66, no. 1, pp. 121-128, 1998.
- [15] S. Chen, V. Kancharla, and Y. Lu, "Laser-based microscale patterning of biodegradable polymers for biomedical applications," *International Journal of Materials and Product Technology*, vol. 18, no. 4, pp. 457-468, 2003.
- [16] C. Aguilar, Y. Lu, S. Mao, and S. Chen, "Direct micro-patterning of biodegradable polymers using ultraviolet and femtosecond lasers," *Biomaterials*,

- vol. 26, no. 36, pp. 7642-7649, 2005.
- [17] H. Huang and Z. Guo, "USP laser PDMS thin-layer separation and micro-fabrication," *Journal of Micromechanics and Microengineering*, vol. 19, p. 055007, 2009.
  - [18] Y. Liu, S. Sun, S. Singha, M. Cho, and R. Gordon, "3D femtosecond laser patterning of collagen for directed cell attachment," *Biomaterials*, vol. 26, no. 22, pp. 4597-4605, 2005.
  - [19] C. Hallgren, H. Reimers, D. Chakarov, J. Gold, and A. Wennerberg, "An in vivo study of bone response to implants topographically modified by laser micromachining," *Biomaterials*, vol. 24, no. 5, pp. 701-710, 2003.
  - [20] Y. Li, K. Itoh, W. Watanabe, K. Yamada, D. Kuroda, J. Nishii, and Y. Jiang, "Three-dimensional hole drilling of silica glass from the rear surface with femtosecond laser pulses," *Optics letters*, vol. 26, no. 23, pp. 1912-1914, 2001.
  - [21] J. Kearney, "Guidelines on processing and clinical use of skin allografts," *Clinics in dermatology*, vol. 23, no. 4, pp. 357-364, 2005.
  - [22] P. Costantino, S. Govindaraj, D. Hiltzik, D. Buchbinder, and M. Urken, "Acellular dermis for facial soft tissue augmentation: preliminary report," *Archives of Facial Plastic Surgery*, vol. 3, no. 1, p. 38, 2001.
  - [23] S. Spear, P. Parikh, E. Reisin, and N. Menon, "Acellular dermis-assisted breast reconstruction," *Aesthetic Plastic Surgery*, vol. 32, no. 3, pp. 418-425, 2008.
  - [24] B. Buck and T. Malinin, "Human bone and tissue allografts: preparation and safety," *Clinical Orthopaedics and Related Research*, vol. 303, p. 8, 1994.
  - [25] M. Jaunich, S. Raje, K. Kim, K. Mitra, and Z. Guo, "Bio-heat transfer analysis during short pulse laser irradiation of tissues," *International Journal of Heat and Mass Transfer*, vol. 51, no. 23-24, pp. 5511-5521, 2008.
  - [26] K. Sasaki, A. Aoki, S. Ichinose, and I. Ishikawa, "Ultrastructural analysis of bone tissue irradiated by Er: YAG Laser," *Lasers in Surgery and Medicine*, vol. 31, no. 5, pp. 322-332, 2002.
  - [27] J. Walsh, T. Flotte, R. Anderson, and T. Deutsch, "Pulsed CO<sub>2</sub> laser tissue ablation: effect of tissue type and pulse duration on thermal damage," *Lasers Surg Med*, vol. 8, no. 2, pp. 108-118, 1988.
  - [28] K. Trauner, N. Nishioka, and D. Patel, "Pulsed holmium: yttrium-aluminum-garnet (Ho: YAG) laser ablation of fibrocartilage and articular cartilage," *The American Journal of Sports Medicine*, vol. 18, no. 3, p. 316, 1990.
  - [29] J. Neev, W. Carrasco, W. Armstrong, L. Da Silva, M. Feit, D. Matthews, M. Perry, A. Rubenchik, and B. Stuart, "Applications of ultrashort-pulse lasers for hard tissue surgery," p. 149, 1996.
  - [30] A. Rode, E. Gamaly, B. Luther-Davies, B. Taylor, J. Dawes, A. Chan, R. Lowe, and P. Hannaford, "Subpicosecond laser ablation of dental enamel," *Journal of Applied Physics*, vol. 92, p. 2153, 2002.
  - [31] B. Kim, M. Feit, A. Rubenchik, E. Joslin, P. Celliers, J. Eichler, and L. Da Silva, "Influence of pulse duration on ultrashort laser pulse ablation of biological tissues," *Journal of Biomedical Optics*, vol. 6, p. 332, 2001.
  - [32] H. Sun, M. Han, M. Niemz, and J. Bille, "Femtosecond laser corneal ablation threshold: Dependence on tissue depth and laser pulse width," *Lasers in Surgery and Medicine*, vol. 39, no. 8, pp. 654-658, 2007.

- [33] M. Göetz, S. Fischer, B. Groh, M. Ott, S. Goelz, and J. Bille, "Plasma-mediated ablation of brain tissue in liquid media and application in stereotactic laser neurosurgery," p. 136, 1996.
- [34] Microscopy with oil immersion. URL: [www.ruf.rice.edu](http://www.ruf.rice.edu)
- [35] J. Jiao and Z. Guo, "Thermal interaction of short-pulsed laser focused beams with skin tissues," *Physics in Medicine and Biology*, vol. 54, pp. 4225-4241, 2009.
- [36] H. Downing and D. Williams, "Optical constants of water in the infrared," *Journal of Geophysical Research-Oceans*, vol. 80, no. 12.
- [37] G. Hale and M. Querry, "Optical constants of water in the 200-nm to 200- $\mu$ m wavelength region," *Applied Optics*, vol. 12, no. 3, pp. 555-563, 1973.
- [38] T. Troy and S. Thennadil, "Optical properties of human skin in the near infrared wavelength range of 1000 to 2200 nm," *Journal of Biomedical Optics*, vol. 6, p. 167, 2001.
- [39] M. Niemz, *Laser-tissue interactions: fundamentals and applications*, Springer Verlag, 2003.
- [40] M. Klingenberg, C. Bohris, M. Niemz, J. Bille, R. Kurek, and D. Wallwiener, "Multifibre application in laser-induced interstitial thermotherapy under on-line MR control," *Lasers in Medical Science*, vol. 15, no. 1, pp. 6-14, 2000.
- [41] D. Wallwiener, R. Kurek, D. Pollmann, M. Kaufmann, H. Schmid, G. Bastert, and F. Frank, "Palliative therapy of gynecological malignancies by laserinduced interstitial thermotherapy," *Lasermedizin*, vol. 10, no. 1, pp. 44-51, 1994.
- [42] A. Vogel and V. Venugopalan, "Mechanisms of pulsed laser ablation of biological tissues," *Chem. Rev*, vol. 103, no. 2, pp. 577-644, 2003.
- [43] N. Bulgakova and A. Bulgakov, "Pulsed laser ablation of solids: transition from normal vaporization to phase explosion," *Applied Physics A: Materials Science & Processing*, vol. 73, no. 2, pp. 199-208, 2001.
- [44] C. Cheng and X. Xu, "Mechanisms of decomposition of metal during femtosecond laser ablation," *Physical Review B*, vol. 72, no. 16, p. 165415, 2005.
- [45] J. Andrew, P. Dyer, D. Forster, and P. Key, "Direct etching of polymeric materials using a XeCl laser," *Applied Physics Letters*, vol. 43, p. 717, 1983.
- [46] J. Brannon, J. Lankard, A. Baise, F. Burns, and J. Kaufman, "Excimer laser etching of polyimide," *Journal of Applied Physics*, vol. 58, p. 2036, 1985.
- [47] A. Vogel, J. Noack, G. Hüttman, and G. Paltauf, "Mechanisms of femtosecond laser nanosurgery of cells and tissues," *Applied Physics B: Lasers and Optics*, vol. 81, no. 8, pp. 1015-1047, 2005.
- [48] W. Leemans, C. Clayton, W. Mori, K. Marsh, A. Dyson, and C. Joshi, "Plasma physics aspects of tunnel-ionized gases," *Physical review letters*, vol. 68, no. 3, pp. 321-324, 1992.
- [49] A. Vogel, "Nonlinear absorption: intraocular microsurgery and laser lithotripsy," *Physics in Medicine and Biology*, vol. 42, pp. 895-912, 1997.
- [50] A. Vogel, "Optical Breakdown in Water and Ocular Media, and Its Use for Intraocular Photodisruption. Aachen," ed: Shaker Verlag, 2001.
- [51] R. Srinivasan and V. Mayne-Banton, "Self-developing photoetching of poly (ethylene terephthalate) films by far-ultraviolet excimer laser radiation," *Applied Physics Letters*, vol. 41, p. 576, 1982.
- [52] E. Jansen, T. Van Leeuwen, M. Motamedi, C. Borst, and A. Welch, "Partial

- vaporization model for pulsed mid-infrared laser ablation of water," *Journal of Applied Physics*, vol. 78, no. 1, pp. 564-571, 1995.
- [53] A. McKenzie, "A three-zone model of soft-tissue damage by a CO<sub>2</sub> laser," *Physics in Medicine and Biology*, vol. 31, pp. 967-983, 1986.
  - [54] A. McKenzie, "An extension of the three-zone model to predict depth of tissue damage beneath Er: YAG and Ho: YAG laser excisions," *Physics in Medicine and Biology*, vol. 34, pp. 107-114, 1989.
  - [55] A. McKenzie, "Physics of thermal processes in laser-tissue interaction," *Physics in Medicine and Biology*, vol. 35, pp. 1175-1210, 1990.
  - [56] D. Rosen, D. Hastings, and G. Weyl, "Coupling of pulsed 0.35- $\mu$ m laser radiation to titanium alloys," *Appl. phys.*, vol. 53, p. 5882, 1982.
  - [57] M. Frenz, A. Zweig, V. Romano, H. Weber, N. Chapliev, and A. Silenok, "Dynamics in laser cutting of soft media," p. 22, 1990.
  - [58] A. Zweig, "A thermo-mechanical model for laser ablation," *Journal of Applied Physics*, vol. 70, p. 1684, 1991.
  - [59] A. Zweig, "Infrared tissue ablation: consequences of liquefaction," *Proc. SPIE*, vol. 1427, p. 2, 1991.
  - [60] B. Majaron, P. Plestenjak, and M. Luka "Thermo-mechanical laser ablation of soft biological tissue: modeling the micro-explosions," *Applied Physics B: Lasers and Optics*, vol. 69, no. 1, pp. 71-80, 1999.
  - [61] L. Zhigilei, P. Kodali, and B. Garrison, "A microscopic view of laser ablation," *Journal of Physical Chemistry B-Condensed Phase*, vol. 102, no. 16, pp. 2845-2853, 1998.
  - [62] L. Zhigilei, P. Kodali, and B. Garrison, "Molecular dynamics model for laser ablation and desorption of organic solids," *J. Phys. Chem. B*, vol. 101, no. 11, pp. 2028-2037, 1997.
  - [63] L. Zhigilei and B. Garrison, "Microscopic mechanisms of laser ablation of organic solids in the thermal and stress confinement irradiation regimes," *Journal of Applied Physics*, vol. 88, p. 1281, 2000.
  - [64] N. Bloembergen, "Laser-induced electric breakdown in solids," *IEEE journal of quantum electronics*, vol. 10, no. 3, pp. 375-386, 1974.
  - [65] A. Epifanov, "Theory of electron-avalanche ionization induced in solids by electromagnetic waves," *IEEE journal of quantum electronics*, vol. 17, pp. 2018-2022, 1981.
  - [66] C. Sacchi, "Laser-induced electric breakdown in water," *Journal of the Optical Society of America B*, vol. 8, no. 2, pp. 337-345, 1991.
  - [67] E. Van Stryland, M. Soileau, A. Smirl, and W. Williams, "Pulse-width and focal-volume dependence of laser-induced breakdown," *Physical Review B*, vol. 23, no. 5, pp. 2144-2151, 1981.
  - [68] R. Taylor, K. Leopold, S. Mihailov, and R. Brimacombe, "Damage measurements of fused silica fibres using long optical pulse XeCl lasers," *Optics communications*, vol. 63, no. 1, pp. 26-31, 1987.
  - [69] D. Du, X. Liu, G. Korn, J. Squier, and G. Mourou, "Laser-induced breakdown by impact ionization in SiO<sub>2</sub> with pulse-widths from 7 ns to 150 fs," *Appl. Phys. Lett.*, vol. 64, no. 23, pp. 3071-3073, 1994.
  - [70] D. Stern, R. Schoenlein, C. Puliafito, E. Dobi, R. Birngruber, and J. Fujimoto,

- "Corneal ablation by nanosecond, picosecond, and femtosecond lasers at 532 and 625 nm," *Archives of ophthalmology*, vol. 107, no. 4, p. 587, 1989.
- [71] M. H. Niemz, T. Hoppeler, T. Juhasz, and J. F. Bille, "Intrastromal ablations for refractive corneal surgery using picosecond infrared laser pulses," *Laser Light Ophthalmol*, vol. 5, pp. 149-155, 1993.
  - [72] A. Vogel, M. Capon, M. Asiyo-Vogel, and R. Birngruber, "Intraocular photodisruption with picosecond and nanosecond laser pulses: tissue effects in cornea, lens, and retina," *Investigative ophthalmology & visual science*, vol. 35, no. 7, p. 3032, 1994.
  - [73] P. Kennedy, O. Div, and A. Brooks, "A first-order model for computation of laser-induced breakdown thresholds in ocular and aqueous media. I. Theory," *IEEE journal of quantum electronics*, vol. 31, no. 12, pp. 2241-2249, 1995.
  - [74] M. Niemz, "Threshold dependence of laser-induced optical breakdown on pulse duration," *Applied Physics Letters*, vol. 66, p. 1181, 1995.
  - [75] B. Stuart, M. Feit, S. Herman, A. Rubenchik, B. Shore, and M. Perry, "Optical ablation by high-power short-pulse lasers," *Journal of the Optical Society of America B*, vol. 13, no. 2, pp. 459-468, 1996.
  - [76] Q. Feng, J. Moloney, A. Newell, E. Wright, K. Cook, P. Kennedy, D. Hammer, B. Rockwell, and C. Thompson, "Theory and simulation on the threshold of water breakdown induced by focused ultrashort laser pulses," *IEEE journal of quantum electronics*, vol. 33, no. 2, pp. 127-137, 1997.
  - [77] J. Noack, A. Vogel, and M. Lubeck, "Laser-induced plasma formation in water at nanosecond to femtosecond time scales: calculation of thresholds, absorption coefficients, and energy density," *IEEE journal of quantum electronics*, vol. 35, no. 8, pp. 1156-1167, 1999.
  - [78] B. Stuart, M. Feit, S. Herman, A. Rubenchik, B. Shore, and M. Perry, "Nanosecond-to-femtosecond laser-induced breakdown in dielectrics," *Physical Review B*, vol. 53, no. 4, pp. 1749-1761, 1996.
  - [79] H. Choi, D. Farson, J. Bovatsek, A. Arai, and D. Ashkenasi, "Direct-write patterning of indium-tin-oxide film by high pulse repetition frequency femtosecond laser ablation," *Applied Optics*, vol. 46, no. 23, pp. 5792-5799, 2007.
  - [80] Y. Dong and P. Molian, "Femtosecond pulsed laser ablation of 3CSiC thin film on silicon," *Applied Physics A: Materials Science & Processing*, vol. 77, no. 6, pp. 839-846, 2003.
  - [81] X. Wang, G. Lim, H. Zheng, F. Ng, W. Liu, and S. Chua, "Femtosecond pulse laser ablation of sapphire in ambient air," *Applied Surface Science*, vol. 228, no. 1-4, pp. 221-226, 2004.
  - [82] S. Baudach, J. Bonse, and W. Kautek, "Ablation experiments on polyimide with femtosecond laser pulses," *Applied Physics A: Materials Science & Processing*, vol. 69, pp. 395-398, 1999.
  - [83] A. Ben-Yakar and R. Byer, "Femtosecond laser ablation properties of borosilicate glass," *Journal of Applied Physics*, vol. 96, p. 5316, 2004.
  - [84] D. Gómez and I. Goenaga, "On the incubation effect on two thermoplastics when irradiated with ultrashort laser pulses: Broadening effects when machining microchannels," *Applied Surface Science*, vol. 253, no. 4, pp. 2230-2236, 2006.
  - [85] X. Ni, C. Wang, L. Yang, J. Li, L. Chai, W. Jia, R. Zhang, and Z. Zhang,

- "Parametric study on femtosecond laser pulse ablation of Au films," *Applied Surface Science*, vol. 253, no. 3, pp. 1616-1619, 2006.
- [86] U. Hohenleutner, S. Hohenleutner, W. B. Umler, and M. Landthaler, "Fast and effective skin ablation with an Er: YAG laser: determination of ablation rates and thermal damage zones," *Lasers in Surgery and Medicine*, vol. 20, no. 3, pp. 242-247, 1997.
  - [87] C. Rumpf, "New minimally-invasive laser treatment in orthopaedics on spinal deformations and bone tumours," Thesis, Universitätsbibliothek, 2001.
  - [88] F. Loesel, M. Niemz, J. Bille, and T. Juhasz, "Laser-induced optical breakdown on hard and soft tissues and its dependence on the pulse duration: experiment and model," *IEEE journal of quantum electronics*, vol. 32, no. 10, pp. 1717-1722, 1996.
  - [89] T. Juhasz, G. Kastis, C. Suárez, Z. Bor, and W. Bron, "Time-resolved observations of shock waves and cavitation bubbles generated by femtosecond laser pulses in corneal tissue and water," *Lasers in Surgery and Medicine*, vol. 19, no. 1, pp. 23-31, 1996.
  - [90] B. Girard, D. Yu, M. Armstrong, B. Wilson, C. Clokie, and R. Miller, "Effects of femtosecond laser irradiation on osseous tissues," *Lasers in Surgery and Medicine*, vol. 39, no. 3, pp. 273-285, 2007.
  - [91] P. Tsai, B. Friedman, A. Ifarraguerri, B. Thompson, V. Lev-Ram, C. Schaffer, Q. Xiong, R. Tsien, J. Squier, and D. Kleinfeld, "All-optical histology using ultrashort laser pulses," *Neuron*, vol. 39, no. 1, pp. 27-41, 2003.
  - [92] J. C. McDonald and G. M. Whitesides, "Poly(dimethylsiloxane) as a Material for Fabricating Microfluidic Devices," *Accounts of Chemical Research*, vol. 35, no. 7, pp. 491-499, 2002.
  - [93] J. C. McDonald, D. C. Duffy, J. R. Anderson, D. T. Chiu, H. Wu, O. J. A. Schueller, and G. M. Whitesides, "Fabrication of microfluidic systems in poly(dimethylsiloxane)," *Electrophoresis*, vol. 21, pp. 27-40, 2000.
  - [94] Y. Doi and K. Fukuda, *Biodegradable plastics and polymers*, Elsevier Amsterdam, 1994.
  - [95] T. Kondo, K. Yamasaki, S. Juodkazis, S. Matsuo, V. Mizeikis, and H. Misawa, "Three-dimensional microfabrication by femtosecond pulses in dielectrics," *Thin Solid Films*, vol. 453, pp. 550-556, 2004.
  - [96] D. B. Wolfe, J. B. Ashcom, J. C. Hwang, C. B. Schaffer, E. Mazur, and G. M. Whitesides, "Customization of Poly(dimethylsiloxane) Stamps by Micromachining Using a Femtosecond-Pulsed Laser," *Advanced Materials*, vol. 15, no. 1, pp. 62-65, 2003.
  - [97] D. Chang-Yen, R. Eich, and B. Gale, "A monolithic PDMS waveguide system fabricated using soft-lithography techniques," *Journal of Lightwave Technology*, vol. 23, no. 6, p. 2088, 2005.
  - [98] K. Rubahn, J. Ihlemann, G. Jakopic, A. Simonsen, and H. Rubahn, "UV laser-induced grating formation in PDMS thin films," *Applied Physics A: Materials Science & Processing*, vol. 79, no. 7, pp. 1715-1719, 2004.
  - [99] A. Rosenfeld, M. Lorenz, R. Stoian, and D. Ashkenasi, "Ultrashort laser pulse damage threshold of transparent materials and the role of incubation," *Applied Physics A: Materials Science & Processing*, vol. 69, pp. 373-376, 1999.

- [100] Gaussian Beam Optics. URL: [www.mellesgriot.com](http://www.mellesgriot.com)
- [101] A. Yariv, "Quantum Electronics. 3<sup>rd</sup> ed," *New York: John Wiley & Sons*, 1989.
- [102] Z. Guo, S. Kan Wan, D. August, J. Ying, S. Dunn, and J. Semmlow, "Optical imaging of breast tumor through temporal log-slope difference mappings," *Computers in Biology and Medicine*, vol. 36, no. 2, pp. 209-223, 2006.
- [103] J. Bonse, J. Wrobel, J. Krüger, and W. Kautek, "Ultrashort-pulse laser ablation of indium phosphide in air," *Applied Physics A: Materials Science & Processing*, vol. 72, no. 1, pp. 89-94, 2001.
- [104] N. Suhm, M. Götz, J. Fischer, F. Loesel, W. Schlegel, V. Sturm, J. Bille, and R. Schröder, "Ablation of neural tissue by short-pulsed lasers: a technical report," *Acta neurochirurgica*, vol. 138, no. 3, pp. 346-349, 1996.
- [105] W. Kautek, S. Mitterer, J. Krüger, W. Husinsky, and G. Grabner, "Femtosecond-pulse laser ablation of human corneas," *Applied Physics A: Materials Science & Processing*, vol. 58, no. 5, pp. 513-518, 1994.
- [106] M. Mahirogullari, C. Ferguson, P. Whitlock, K. Stabile, and G. Poehling, "Freeze-dried allografts for anterior cruciate ligament reconstruction," *Clinics in Sports Medicine*, vol. 26, no. 4, pp. 625-637, 2007.
- [107] G. Friedlaender, "Bone-banking," *The Journal of bone and joint surgery. American volume*, vol. 64, no. 2, p. 307, 1982.
- [108] H. Huang and Z. Guo, "Human dermis separation via ultra-short pulsed laser plasma-mediated ablation," *Journal of Physics D: Applied Physics*, vol. 42, p. 165204, 2009.
- [109] T. Crawford, A. Borowiec, and H. Haugen, "Femtosecond laser micromachining of grooves in silicon with 800 nm pulses," *Applied Physics A: Materials Science & Processing*, vol. 80, no. 8, pp. 1717-1724, 2005.
- [110] D. Shin, J. Lee, Y. Chung, and H. Sohn, "Laser Cutting Process for FPCB," in *International Conference on Smart Manufacturing Application ICSMA 2008*, Gyeonggi-do, Korea, pp. 357-362, 2008.
- [111] G. Daminelli, J. Krüger, and W. Kautek, "Femtosecond laser interaction with silicon under water confinement," *Thin Solid Films*, vol. 467, no. 1-2, pp. 334-341, 2004.
- [112] M. van Gemert and A. Welch, "Time constants in thermal laser medicine," *Lasers in Surgery and Medicine*, vol. 9, no. 4, pp. 405-421, 2005.
- [113] J. Roider, F. Hillenkamp, T. Flotte, and R. Birngruber, "Microphotocoagulation: selective effects of repetitive short laser pulses," *Proceedings of the National Academy of Sciences*, vol. 90, no. 18, p. 8643, 1993.
- [114] B. Choi, J. Barton, E. Chan, and A. Welch, "Imaging of the Irradiation of Skin With a Clinical CO<sub>2</sub> Laser System: Implications," *Lasers in Surgery and Medicine*, vol. 23, pp. 185-193, 1998.
- [115] B. Choi and A. Welch, "Analysis of thermal relaxation during laser irradiation of tissue," *Lasers in Surgery and Medicine*, vol. 29, no. 4, pp. 351-359, 2001.
- [116] J. Neev, L. Da Silva, M. Feit, M. Perry, A. Rubenchik, and B. Stuart, "Ultrashort pulse lasers for hard tissue ablation," *IEEE Journal of Selected Topics in Quantum Electronics*, vol. 2, no. 4, pp. 790-800, 1996.
- [117] M. Feit, A. Rubenchik, B. Kim, L. Da Silva, and M. Perry, "Physical characterization of ultrashort laser pulse drilling of biological tissue," *Applied*

- Surface Science*, vol. 127, pp. 869-874, 1998.
- [118] B. Kim, M. Feit, A. Rubenchik, E. Joslin, J. Eichler, P. Stoller, and L. Da Silva, "Effects of high repetition rate and beam size on hard tissue damage due to subpicosecond laser pulses," *Applied Physics Letters*, vol. 76, p. 4001, 2000.
  - [119] B. Anvari, B. Tanenbaum, T. Milner, S. Kimel, L. Svaasand, and J. Nelson, "A theoretical study of the thermal response of skin to cryogen spray cooling and pulsed laser irradiation: implications for treatment of port wine stain birthmarks," *Physics in Medicine and Biology*, vol. 40, pp. 1451-1465, 1995.
  - [120] M. Cohen, "Measurement of the thermal properties of human skin. A review," *Journal of Investigative Dermatology*, vol. 69, no. 3, pp. 333-338, 1977.
  - [121] A. Tsai, "Investigation of variability in skin tissue intrinsic thermal conductivity measurements," Thesis, Massachusetts Institute of Technology, 1995.
  - [122] M. Ozisik and M. Oezisik, *Heat conduction*, John Wiley New York, 1993.
  - [123] D. Fried, J. Ragadio, and A. Champion, "Residual heat deposition in dental enamel during IR laser ablation at 2.79, 2.94, 9.6, and 10.6  $\mu\text{m}$ ," *Lasers in Surgery and Medicine*, vol. 29, no. 3, pp. 221-229, 2001.
  - [124] C. Grigoropoulos, D. Hwang, and A. Chimmalgi, "Nanometer-scale laser direct-write using near-field optics," *MRS bulletin*, vol. 32, no. 1, pp. 16-22, 2007.
  - [125] K. Yi, Z. Yang, and Y. Lu, "Fabrication of nanostructures with high electrical conductivity on silicon surfaces using a laser-assisted scanning tunneling microscope," *Journal of Applied Physics*, vol. 103, p. 054307, 2008.
  - [126] M. Hong, C. Lim, Y. Zhou, L. Tan, L. Shi, and T. Chong, "Surface Nanofabrication by Laser Precision Engineering," *The Review of Laser Engineering*, vol. 36, no. APLS, pp. 1184-1187, 2008.
  - [127] N. Murphy-DuBay, L. Wang, E. Kinzel, S. Uppuluri, and X. Xu, "Nanopatterning using NSOM probes integrated with high transmission nanoscale bowtie aperture," *Optics Express*, vol. 16, no. 4, pp. 2584-2589, 2008.
  - [128] W. Srituravanich, N. Fang, C. Sun, Q. Luo, and X. Zhang, "Plasmonic nanolithography," *Nano letters*, vol. 4, no. 6, pp. 1085-1088, 2004.
  - [129] A. Heltzel, A. Battula, J. Howell, and S. Chen, "Nanostructuring borosilicate glass with near-field enhanced energy using a femtosecond laser pulse," *Journal of Heat Transfer*, vol. 129, p. 53, 2007.
  - [130] S. Huang, M. Hong, B. Luk'yanchuk, Y. Zheng, W. Song, Y. Lu, and T. Chong, "Pulsed laser-assisted surface structuring with optical near-field enhanced effects," *Journal of Applied Physics*, vol. 92, p. 2495, 2002.
  - [131] T. Sakai, N. Nedyalkov, and M. Obara, "Positive and negative nanohole-fabrication on glass surface by femtosecond laser with template of polystyrene particle array," *Journal of Physics D: Applied Physics*, vol. 40, no. 7, pp. 2102-2107, 2007.
  - [132] H. Munzer, M. Mosbacher, M. Bertsch, J. Zimmermann, P. Leiderer, and J. Boneberg, "Local field enhancement effects for nanostructuring of surfaces," *Journal of Microscopy*, vol. 202, no. Pt 1, pp. 129-135, 2001.
  - [133] W. Guo, Z. Wang, L. Li, D. Whitehead, B. Luk'yanchuk, and Z. Liu, "Near-field laser parallel nanofabrication of arbitrary-shaped patterns," *Applied Physics Letters*, vol. 90, p. 243101, 2007.
  - [134] L. Li, Y. Lu, D. Doerr, D. Alexander, and X. Chen, "Parametric investigation of



- laser nanoimprinting of hemispherical cavity arrays," *Journal of Applied Physics*, vol. 96, p. 5144, 2004.
- [135] R. Micheletto, H. Fukuda, and M. Ohtsu, "A simple method for the production of a two-dimensional, ordered array of small latex particles," *Langmuir*, vol. 11, no. 9, pp. 3333-3336, 1995.
  - [136] Y. Lu and S. Chen, "Nanopatterning of a silicon surface by near-field enhanced laser irradiation," *Nanotechnology*, vol. 14, pp. 505-508, 2003.
  - [137] C. Park, J. Wilkinson, S. Banda, Z. Ounaies, K. Wise, G. Sauti, P. Lillehei, and J. Harrison, "Aligned single-wall carbon nanotube polymer composites using an electric field," *Journal of Polymer Science: Part A Polymer Chemistry*, vol. 44, no. 12, p. 1751, 2006.
  - [138] M. Bangar, D. Shirale, W. Chen, N. Myung, and A. Mulchandani, "Single Conducting Polymer Nanowire Chemiresistive Label-Free Immunosensor for Cancer Biomarker," *Analytical Chemistry*, vol. 81, no. 6, pp. 2168-2175, 2009.
  - [139] A. Nocke, M. Wolf, H. Budzier, K. Arndt, and G. Gerlach, "Dielectrophoretic alignment of polymer compounds for thermal sensing," *Sensors & Actuators: A. Physical*, 2009.
  - [140] C. Yan, T. Zhang, and P. Lee, "Flow assisted synthesis of highly ordered silica nanowire arrays," *Applied Physics A: Materials Science & Processing*, vol. 94, no. 4, pp. 763-766, 2009.
  - [141] W. Cai and R. Piestun, "Patterning of silica microsphere monolayers with focused femtosecond laser pulses," *Applied Physics Letters*, vol. 88, p. 111112, 2006.
  - [142] Y. Zhou, M. Hong, J. Fuh, L. Lu, B. Luk'yanchuk, C. Lim, and Z. Wang, "Nanopatterning mask fabrication by femtosecond laser irradiation," *Journal of Materials Processing Tech.*, vol. 192, pp. 212-217, 2007.
  - [143] A. Chimmalgi, C. Grigoropoulos, and K. Komvopoulos, "Surface nanostructuring by nano-/femtosecond laser-assisted scanning force microscopy," *Journal of Applied Physics*, vol. 97, p. 104319, 2005.
  - [144] J. Bohn, D. Nesbitt, and A. Gallagher, "Field enhancement in apertureless near-field scanning optical microscopy," *Journal of the Optical Society of America A*, vol. 18, no. 12, pp. 2998-3006, 2001.
  - [145] M. Micic, N. Klymyshyn, Y. Suh, and H. Lu, "Finite element method simulation of the field distribution for AFM tip-enhanced surface-enhanced Raman scanning microscopy," *J. Phys. Chem. B*, vol. 107, no. 7, pp. 1574-1584, 2003.
  - [146] A. Maradudin, *Light scattering and nanoscale surface roughness*, Springer Verlag, 2007.
  - [147] K. Nahm and W. Wolfe, "Light-scattering models for spheres on a conducting plane: comparison with experiment," *Applied Optics*, vol. 26, no. 15, pp. 2995-2999, 1987.
  - [148] G. Videen, "Light scattering from a sphere on or near a surface," *Journal of the Optical Society of America A*, vol. 8, no. 3, pp. 483-489, 1991.
  - [149] G. Videen, D. Ngo, P. Chylek, and R. Pinnick, "Light scattering from a sphere with an irregular inclusion," *J. Opt. Soc. Am. A*, vol. 12, pp. 922-928, 1995.
  - [150] R. Borghi, F. Gori, M. Santarsiero, F. Frezza, and G. Schettini, "Plane-wave scattering by a set of perfectly conducting circular cylinders in the presence of a plane surface," *Journal of the Optical Society of America A*, vol. 13, no. 12, pp.

- 2441-2452, 1996.
- [151] P. Valle, F. Moreno, J. Saiz, and F. González "Near-field scattering from subwavelength metallic protuberances on conducting flat substrates," *Physical Review B*, vol. 51, no. 19, pp. 13681-13690, 1995.
  - [152] P. Valle, F. Gonzalez, and F. Moreno, "Electromagnetic wave scattering from conducting cylindrical structures on flat substrates: study by means of the extinction theorem," *Appl. Opt.*, vol. 33, pp. 512-523, 1994.
  - [153] Refractive index as a function of wavelength. URL: <http://www.philiplaven.com/p20.html>

## Curriculum Vitae

Huan Huang

- 1999 – 2003 Bachelor of Science, Department of Precision Instrument and Mechanology, Tsinghua University, Beijing, China
- 2003 – 2005 Master of Science, Department of Precision Instrument and Mechanology, Tsinghua University, Beijing, China
- 2006 – 2010 Doctor of Philosophy, Department of Mechanical and Aerospace Engineering, Rutgers University-New Brunswick, New Jersey, U.S.A.

### Publications

1. Zhixiong Guo, Xiaoliang Wang and Huan Huang, "Plasma-mediated ablation of biofilm contamination," *Appl. Surface Sci.* 2010, Vol. 257(4), pp. 1247-1253, 2010.
2. Huan Huang and Zhixiong Guo, "Ultra-short pulsed laser ablation and stripping of freeze-dry dermis," *Lasers in Medical Science*, Vol. 25(4), pp. 517-524, 2010.
3. Huan Huang and Zhixiong Guo, "Human dermis separation via ultra-short pulsed laser plasma-mediated ablation," *Journal of Physics D: Applied Physics*, Vol. 42, pp. 165204 (9pp), 2009.
4. Huan Huang and Zhixiong Guo, "Ultra-short pulsed laser PDMS thin-layer separation and micro-fabrication," *Journal of Micromechanics and Microengineering*, Vol. 19(5), pp. 055007 (9pp), 2009.
5. Huan Huang and Zhixiong Guo, "Ablation and separation of dermis via ultra-short pulsed laser", *ASME 2009 International Mechanical Engineering Congress & Exposition (IMECE2009-10403)* (9pp), Lake Buena Vista, FL, USA, Nov. 13-19, 2009.
6. Huan Huang and Zhixiong Guo, "3-D micro-fabrication and separation of PDMS by ultra-short pulsed laser," *Proc. of 2008 ASME International Mechanical Engineering Congress & Exposition, IMECE2008-66371* (6pp) Oct. 31-Nov. 6, 2008 Boston, MA, USA.
7. Yen-Wen Lu, Huan Huang, Neha Arora, Abdul Hanifi and Adaleena Mookerjee, "Nanostructure Replication of Biodegradable Polymer Assisted by Low-Surface-Energy Coatings," *Late News, The 2007 IEEE International Conference on Nano/Molecular medicine and Engineering (IEEE-NANOMED)*, 2007.